Dynamic Nuclear Polarization: Theory, Instrumentation, and Applications

Kong Ooi Tan

Dynamic Nuclear Polarization: Theory, Instrumentation, and Applications

(The order is random) Chen, Cody, Qing, Kong, Christy, Michael, Sudheer, Dan , Richard J. Temkin,

Robert G. Griffin[a,*]

[a] Francis Bitter Magnet Laboratory and Department of Chemistry, Massachusetts Institute of Technology, Cambridge, Massachusetts 02139, USA

[1]Present address: xxx

Corresponding Author:

Robert G. Griffin

Francis Bitter Magnet Laboratory and Department of Chemistry, Massachusetts Institute of Technology, Cambridge, Massachusetts 02139, USA

E-Mail: rgg@mit.edu

Keywords: Dynamic Nuclear Polarization

Abstract

Dynamic Nuclear Polarization (DNP) is a hyperpolarization technique used to improve the sensitivity of NMR experiments. There has been a remarkable growth ranging from method development, advancement in instrumentation, and applications in the field of MAS-DNP NMR. In this review, we provide a comprehensive overview on the recent methodological, instrumental developments, and the applications of the DNP techniques. In contrast to other review articles in literature, our article provides an extensive and elaborated coverage on the topic of the pulsed DNP techniques, and hardware such as MAS-DNP probes, microwave sources, and cryogenics. In the end, a perspective on the future development and prospect on the development and application of the DNP techniques will be discussed.

Biographies

Dr. Kong Ooi Tan

Dr. Kong Ooi Tan received his undergraduate degree in Physics from Imperial College London. He worked on laboratory astrophysics in the field of plasma physics for his master thesis. During his PhD from 2011 to 2016, he worked on the topic of pulse-sequence design using Floquet theory in solid-state NMR, under the supervision of Prof. Matthias Ernst and Prof. Beat H. Meier at ETH Zurich. He had improvised and designed several homonuclear dipolar recoupling sequences, and presented a theoretical framework that unifies all decoupling sequences using a single set of master equations. He is currently a postdoctoral research associate in the group of Prof. Robert G. Griffin at MIT, working on method development in the pulsed DNP techniques.

XXXX

He/She was a graduate student in Prof. Robert G. Griffin group. (Default description if the biography is not received)

Dr. Chen Yang

Dr. Chen Yang received his undergraduate degree in Materials Physics from Nanjing University in 2010. From September 2010 to March 2015 he did PhD research with Prof. Leonard Mueller on biological solid-state NMR methodologies. He then joined the group of Prof. Robert G. Griffin at MIT during April 2015 as a postdoctoral associate, and has been working on DNP instrumentation and DNP simulation. He left academia in March 2018 to pursue industry opportunities.

Daniel Banks

Daniel received his undergraduate degree in Chemistry from the Pennsylvania State university in 2014. He did his undergraduate research in the group of Prof. Karl T. Mueller. He is currently a Ph.D. candidate in the group of Prof. Robert G. Griffin at MIT. His research interests include instrumentation development and implementation of fast MAS DNP and ^{17}O DNP at high magnetic fields.

Dr. Sudheer Jawla

Dr. Sudheer Jawla received the M.Sc. degree in Physics from Indian Institute of Technology, Delhi, India, and, Ph.D. degree in physics from Swiss Plasma Center, École Polytechnique Fédérale de Lausanne (EPFL), Lausanne, Switzerland. He is currently a Research Scientist at Plasma Science and Fusion Center, Massachusetts Institute of Technology (MIT), Cambridge, MA, USA. His current research interests include high frequency vacuum electron devices, high-power gyrotrons, microwave and THz systems for dynamic nuclear polarization/nuclear magnetic resonance applications, and, quasi-optical components at millimeter and THz wavelengths.

Dr. Richard Temkin

Dr. Richard Temkin received the B.A. degree in physics from Harvard College, Cambridge, MA, USA, and the Ph.D. degree in physics from the Massachusetts Institute of Technology (MIT), Cambridge, USA. He is a Senior Scientist in the MIT Department of Physics and serves as Associate Director of MIT's Plasma Science and Fusion Center. Dr. Temkin is a life fellow of the IEEE, fellow of the American Physical Society and the Institute of Physics, London, U.K.

Michael Mardini

Michael Mardini received his A. B. in Chemistry from Washington University in St. Louis, where he worked with Prof. Alexander Barnes on the development of DNP methodology. In 2016, he started as a Ph.D. student in Griffin at MIT, where he is currently working on extending pulsed DNP to higher magnetic fields.

Thach V. Can

Thach V. Can studied physics at Vietnam National University, Hanoi, received his M.S. from the Florida State University, and obtained his Ph.D. in Physical Chemistry from MIT.

Qing Zhe Ni

Dr. Qing Zhe Ni received a B.S. degree in Chemistry from Florida State University in 2010. She received her Ph.D. from MIT in Physical Chemistry under the guidance of Prof. Robert Griffin. Her graduate

work focused on various aspects of DNP applications, in particular, mechanistic studies of the membrane ion pump, Bacteriorhodopsin. She is currently a postdoctoral research associate at UCSD.

1 Introduction

Dynamic Nuclear Polarization (DNP) is a sensitivity enhancement technique used to enhance Nuclear Magnetic Resonance (NMR) signals by transferring polarization from unpaired electrons to nuclei of interest via microwave irradiation.[1,2] Over the past few decades, the applications of NMR in the field of structural biology, particularly in determining the structures of proteins, has thrived. As of April 2019, 12590 structures deposited in the Protein Data Bank (PDB) were determined by NMR.[3] The advantage of NMR over other spectroscopic methods is that it provides atomic-resolution for determining structures and is non-invasive; however, NMR spectroscopy is generally hampered by poor sensitivity or low polarization, $P = \tanh(\gamma\hbar B_0/2k_{\mathrm{B}}T)$, where γ is the gyromagnetic ratio, $\hbar$ is the reduced Planck constant, B_0 is the static magnetic field, k_{B} is the Boltzmann constant, and T is the temperature. For example, in an NMR experiment conducted with a 1 GHz (23.5 T) magnet at room temperature, the population difference of protons, ^{1}H, in the "spin-up" and "spin-down" states is less than 0.01 %. By contrast, for the same temperature and magnetic field strength, electrons have a polarization approximately $\gamma_{\mathrm{e}}/\gamma_{1\mathrm{H}} \sim 658$ times that of protons. Thus, it is the main objective of DNP to redistribute the populations of the spin states in an electron-nuclei spin system, such that the population difference

between the nuclei spin-up and the spin-down states is higher than that at thermal equilibrium, i.e. signal enhancement.

Due to the recognition of the vast potential for DNP to revolutionize the field of magnetic resonance, more than 34 (from 2009 till 2017) commercial gyrotons, high-power microwave sources at high frequencies, have been installed by Bruker Biospin around the world.[4] Consequently, this initiated the escalating growth in research and scientific publications in the field of DNP over the last decade. Hence, the objective of this article is to provide a concise but comprehensive review of the developments in the field of DNP; particularly the theory, instrumentation, and applications.

We will provide a general overview of the events in the DNP process (Figure 1) that lead to polarization transfer from an unpaired electron to the targeted nuclei of interest. First, the polarizing agent, or radical (Section 3), mixed with sample of interest and a cryoprotectant such as glycerol, is prepared. Then, the resulting glassy mixture is irradiated using a microwave source (Section 5.1) to saturate or nutate the transition between the energy eigenstates. This process is performed most efficiently at cryogenic temperatures (Section 5.3). Depending on the type of DNP mechanism(s) (Section 2) employed, the microwave irradiation scheme is strategically tailored to maximize polarization transfer. After that, the enhanced nuclei that are in close proximity to the radical will distribute the polarization throughout the bulk nuclei and target system-of-interest via the spin diffusion process (Section 4). Finally, conventional NMR spectroscopy can then be applied to the target molecule for various applications such as studying biological macromolecules or inorganic materials (Section 6). In the final section, we will summarize the discussed topics and provide an outlook for the future of DNP.

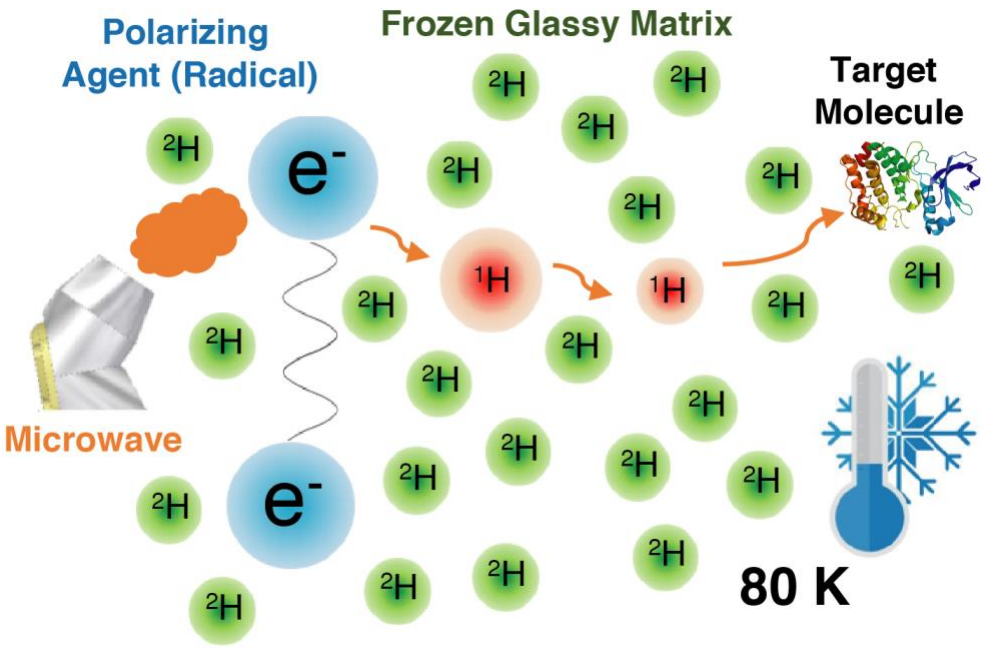

Figure 1: Schematic diagram of the DNP polarization-transfer pathway starting from the radical to the target sample. for instance a protein or a small molecule. The radicals are first irradiated with microwaves to transfer polarization from unpaired electrons to nearby nuclei. Then, the polarization is distributed throughout the bulk nuclei and eventually the target sample in the solvent via the spin diffusion process. Most DNP experiments are performed at cryogenic temperatures for efficient performance. (Fig source : fig0_2.ai)

2 Theory

2.1 CW DNP

Most high-field DNP-NMR techniques employ continuous-wave (CW) microwave irradiation due to the availability of high-frequency microwave oscillators or CW sources.[5] There are in general four different CW-DNP mechanisms responsible for transferring polarization from unpaired electrons to nuclei, namely the solid effect (SE), cross effect (CE), Overhauser effect (OE), and thermal mixing (TM).[6-9] The underlying principles of the mentioned mechanisms driving the polarization transfer are fundamentally different from one another. In the quest for obtaining the maximum enhancement, one has to make strategic choices of radical(s), solvent, temperature, and microwave irradiation scheme in order

to exploit the corresponding DNP mechanism efficiently. The combination of these parameters that give rise to the most efficient transfer are sometimes complicated and not well understood. Nevertheless, we will provide concise but self-contained theoretical descriptions of the four CW-DNP mechanisms, and discuss the conditions where their effects are optimum.

2.1.1 Solid Effect

Following the discovery of the OE in 1953, Jeffries proposed another DNP sequence in non-conducting solids known as the SE,[10] which was then demonstrated experimentally by Abragam and Proctor.[6] Comprehensive reviews and rigorous theoretical approaches for the SE sequence have been discussed for both static[11-13] and MAS[14,15] cases in literature. There are two theoretical approaches to determine the matching conditions and the corresponding transition probabilities, which characterizes the build-up rate of the polarization transfer. The first approach applies perturbation theory to determine the degree of state mixing between the Zeeman eigenstates and is best suited for the case where the electron nutation frequency, ω_{1S}, is small relative to the electron relaxation rate, T_{1e}^{-1}. The second approach uses average Hamiltonian theory (AHT) to determine the time-independent effective Hamiltonian,[16] with the assumption that ω_{1S} is large relative to the hyperfine interaction and the relaxation effect is insignificant. We will adopt the AHT approach here as the derivation takes fewer steps, and it will be shown that the final result converges to the results derived using perturbation theory in the limit of small ω_{1s} relative to the microwave offset frequency, Ω.

Let's first consider a two-spin electron-nuclei system (Figure 2) with a Hamiltonian in the electron rotating frame given by

$$\widehat{\mathcal{H}} = \Omega\hat{S}_z - \omega_{0I}\hat{I}_z + A_{zz}\hat{S}_z\hat{I}_z + B_{zx}\hat{S}_z\hat{I}_x + \omega_{1s}\hat{S}_x, \quad (1)$$

where A_{zz} and B_{zx} are the secular and non-secular components of the hyperfine interaction, ω_{0I} is the Larmor frequency of the nuclear spin, Ω is the microwave offset frequency, and ω_{1S} is the electron

nutation frequency. By inspecting the matrix representation (Equation 2) of the given Hamiltonian (Equation 1), one can see that the Zeeman states will mix due to the presence of the off-diagonal term B_{zx}.

$$\widehat{\mathcal{H}} = \frac{1}{4}\begin{bmatrix} A_{\mathrm{zz}} - 2\omega_{0\mathrm{I}} + 2\Omega & B_{\mathrm{zx}} & 2\omega_{1\mathrm{s}} & 0 \\ B_{\mathrm{zx}} & -A_{\mathrm{zz}} + 2\omega_{0\mathrm{I}} + 2\Omega & 0 & 2\omega_{1\mathrm{s}} \\ 2\omega_{1\mathrm{s}} & 0 & -A_{\mathrm{zz}} - 2\omega_{0\mathrm{I}} - 2\Omega & -B_{\mathrm{zx}} \\ 0 & 2\omega_{1\mathrm{s}} & -B_{\mathrm{zx}} & A_{\mathrm{zz}} + 2\omega_{0\mathrm{I}} - 2\Omega \end{bmatrix} \tag{2}$$

The theoretical analysis can be simplified by aligning the effective microwave field, $\omega_{\mathrm{eff}} = \sqrt{\omega_{1\mathrm{s}}^2 + \Omega^2}$, along the *z*-axis of spin *S* by applying a frame transformation using the propagator $\widehat{U}_{\mathrm{t}} = \exp(-i\theta\hat{S}_{\mathrm{y}})$, where $\theta = \tan^{-1}(\omega_{1\mathrm{s}}/\Omega)$:

$$\begin{aligned} \widehat{\mathcal{H}} &= \omega_{\mathrm{eff}}\cos\theta\,\hat{S}_{\mathrm{z}} - \omega_{0\mathrm{I}}\hat{I}_{\mathrm{z}} + A_{\mathrm{zz}}\hat{S}_{\mathrm{z}}\hat{I}_{\mathrm{z}} + B_{\mathrm{zx}}\hat{S}_{\mathrm{z}}\hat{I}_{\mathrm{x}} + \omega_{\mathrm{eff}}\sin\theta\,\hat{S}_{\mathrm{x}} \\ \widehat{U}_{\mathrm{t}}^{-1}\widehat{\mathcal{H}}\widehat{U}_{\mathrm{t}} &= \omega_{\mathrm{eff}}\hat{S}_{\mathrm{z}} - \omega_{0\mathrm{I}}\hat{I}_{\mathrm{z}} + \left(A_{\mathrm{zz}}\hat{I}_{\mathrm{z}} + B_{\mathrm{zx}}\hat{I}_{\mathrm{x}}\right)\left(\hat{S}_{\mathrm{z}}\cos\theta - \hat{S}_{\mathrm{x}}\sin\theta\right). \end{aligned} \tag{3}$$

Then, we perform an interaction-frame transformation with respect to the term $\widehat{U}_1 = \exp\left(-i\left(\omega_{\mathrm{eff}}\hat{S}_{\mathrm{z}} - \omega_{0\mathrm{I}}\hat{I}_{\mathrm{z}}\right)t\right)$:

$$\begin{aligned} \widehat{\widetilde{\mathcal{H}}}(t) &= \widehat{U}_1^{-1}(t)\widehat{\mathcal{H}}\widehat{U}_1(t) - \left(\omega_{\mathrm{eff}}\hat{S}_{\mathrm{z}} - \omega_{0\mathrm{I}}\hat{I}_{\mathrm{z}}\right) \\ &= \left(A_{\mathrm{zz}}\hat{I}_{\mathrm{z}} + B_{\mathrm{zx}}\left(\hat{I}_{\mathrm{x}}\cos\omega_{0\mathrm{I}}t + \hat{I}_{\mathrm{y}}\sin\omega_{0\mathrm{I}}t\right)\right)\left(\hat{S}_{\mathrm{z}}\cos\theta - \left(\hat{S}_{\mathrm{x}}\cos\omega_{\mathrm{eff}}t - \hat{S}_{\mathrm{y}}\sin\omega_{\mathrm{eff}}t\right)\sin\theta\right). \end{aligned} \tag{4}$$

Next, by inspecting the sinusoidal terms in Equation 4, it is obvious that the matching conditions, $\omega_{\mathrm{eff}} = \pm\omega_{0\mathrm{I}}$, remove the time dependence of the Hamiltonian upon integration:

$$\widehat{\widetilde{\mathcal{H}}} = \frac{\omega_{0\mathrm{I}}}{2\pi}\int_0^{(2\pi)/\omega_{0\mathrm{I}}} \widehat{\widetilde{\mathcal{H}}}(t)\,dt = \begin{cases} -\dfrac{B_{\mathrm{zx}}\sin\theta}{2}\left(\hat{S}_{\mathrm{x}}\hat{I}_{\mathrm{x}} - \hat{S}_{\mathrm{y}}\hat{I}_{\mathrm{y}}\right) + A_{\mathrm{zz}}\hat{S}_{\mathrm{z}}\hat{I}_{\mathrm{z}}\cos\theta \text{ if } \omega_{\mathrm{eff}} = +\omega_{0\mathrm{I}} \\ -\dfrac{B_{\mathrm{zx}}\sin\theta}{2}\left(\hat{S}_{\mathrm{x}}\hat{I}_{\mathrm{x}} + \hat{S}_{\mathrm{y}}\hat{I}_{\mathrm{y}}\right) + A_{\mathrm{zz}}\hat{S}_{\mathrm{z}}\hat{I}_{\mathrm{z}}\cos\theta \text{ if } \omega_{\mathrm{eff}} = -\omega_{0\mathrm{I}} \end{cases} \tag{5}$$

Note that the first terms in the effective Hamiltonian (Equation 5) are the zero-quantum (ZQ, flip-flop) or double-quantum (DQ, flop-flop) terms that are responsible for DNP transfer. The second term, $\hat{S}_z\hat{I}_z$, is a bilinear operator that does not affect the DNP transfer in the first order as it constitutes the identity operator in either the ZQ or DQ subspace. This is evident by inspecting the matrix representation of Equation 5 for the case of $\omega_{\text{eff}} = -\omega_{0I}$ (ZQ condition) as an example:

$$\hat{\bar{\mathcal{H}}} = \frac{1}{4}\begin{bmatrix} A_{zz}\cos\theta & 0 & 0 & 0 \\ 0 & -A_{zz}\cos\theta & -B_{zx}\sin\theta & 0 \\ 0 & -B_{zx}\sin\theta & -A_{zz}\cos\theta & 0 \\ 0 & 0 & 0 & A_{zz}\cos\theta \end{bmatrix}. \tag{6}$$

Note that the middle 2x2 block correlates the states $|\alpha\beta\rangle$ and $|\beta\alpha\rangle$, which form the ZQ subspace. It is trivial to see that the ZQ subspace is not connected to the outer block (DQ subspace) by any off-diagonal elements. Next, we can determine $\rho(t)$ using the Liouville von Neumann (LvN) equation with an initial density operator $\rho(0) = \hat{S}_z$:

$$\begin{gathered} \hat{U}_{\text{eff}} = \exp\left(-i\hat{\bar{\mathcal{H}}}t\right) \\ \rho(t) = \hat{U}_{\text{eff}}\rho(0)\hat{U}_{\text{eff}}^{-1} = \hat{S}_z\cos^2(\omega_{SE}t) + \hat{I}_z\sin^2(\omega_{SE}t) - \left(\hat{S}_x\hat{I}_y - \hat{S}_y\hat{I}_x\right)\sin(2\omega_{SE}t), \end{gathered} \tag{7}$$

where $\omega_{SE} = (B_{zx}\sin\theta)/4$ denotes the SE build-up rate. Despite the $+\hat{I}_z$ sign in Equation 7, either positive or negative enhancement can be obtained depending on the sense of nuclear precession, i.e. sign of the nuclear g-factor, g_n. For instance, ^{1}H and ^{15}N nuclei will receive negative and positive transfer, respectively, for a ZQ matching condition. Note that similar results but an opposite sign of polarization transfer is expected for the DQ case with the matching condition $\omega_{\text{eff}} = \omega_{0I}$. As the magnitude of ω_{1s} employed is usually smaller than the ^{1}H Larmor frequency in most DNP experiments, we approximate the matching conditions at the limit of small θ or $|\omega_{1s}/\Omega| \ll 1$:

$$\omega_{\text{eff}} = \sqrt{\omega_{1s}^2 + \Omega^2} = \pm\omega_{0I} \tag{8}$$

$$\Rightarrow \Omega \sim \pm \omega_{0\mathrm{I}},$$

and the nuclei polarization at initial build-up is given by

$$\sin^2(\omega_{\mathrm{SE}} t) \sim {\omega_{\mathrm{SE}}}^2 t^2$$

$$ {\omega_{\mathrm{SE}}}^2 = \left(\frac{B_{\mathrm{zx}} \omega_{1\mathrm{s}}}{4\omega_{0\mathrm{I}}}\right)^2. \tag{9}$$

Here, we have derived the famous SE matching conditions $\Omega \sim \pm \omega_{0\mathrm{I}}$ (Figure 2b) and the build-up rate implies that the enhancement factor scales by a factor of $\sim {\omega_{0\mathrm{I}}}^{-2}$ relative to the field, assuming all other factors remain constant. These theoretical findings agree with the results derived using the perturbation theory. In principle, we can recover the loss of enhancement factor at higher field be increasing the nutation frequency, $\omega_{1\mathrm{s}}$, by the same factor.

Although the SE mechanism is usually described as a two-spin process, the polarization transfer can also be mediated via a second-order effect on a three-spin system. *Boer* had recorded the first three-spin solid effect on a BDPA-doped sample below 1 K and a weak enhancement factor of ~ 3 was observed.[17] There have been recent attempts to investigate the second-order effect but the enhancements were not directly observable.[18] Nevertheless, our lab has discovered recently that a surprisingly high enhancement factor of ~ 100 (Figure 2b) was recorded using a trityl radical at low field (0.35 T) and a temperature of 80 K. Theoretical analysis and numerical simulations were performed to confirm that a three-spin system involving one electron and two nuclei is responsible for the second-order effect with matching conditions at $\Omega = \pm 2\omega_{0\mathrm{I}}$. Further details of the three-spin solid effect will be presented in a future publication.

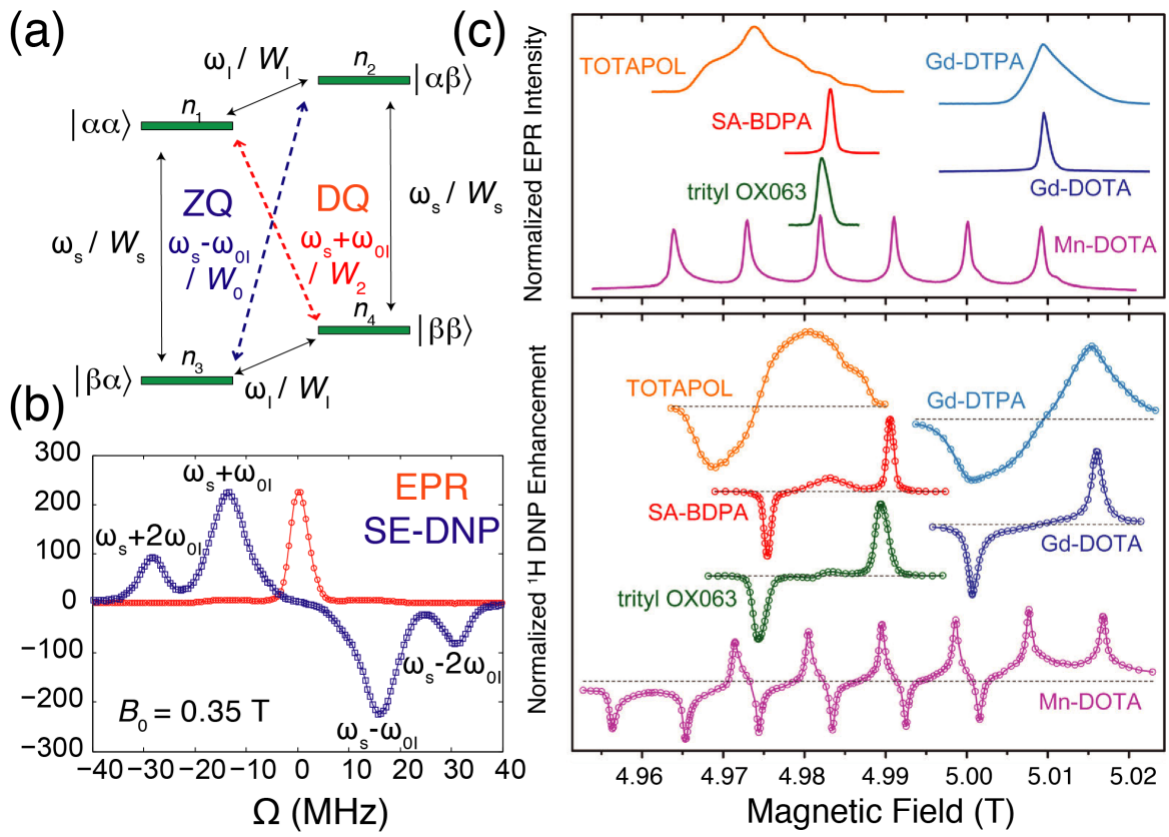

Figure 2: (a) Energy level diagram of a two-spin e^--^{1}H system that shows all possible transitions and relaxation pathways between the energy eigenstates. (b) Experimental DNP field profile of trityl OX063 exhibiting three-spin SE at 0.35 T, obtained by sweeping the microwave frequency. (c) EPR spectra (top) and DNP field profiles (bottom) of radicals at 5 T. The narrow-line radicals have a characteristic separation of $2\boldsymbol{\omega_{0I}} \cong \mathbf{0.015\ T}$ between the ZQ and DQ enhancements for SE. The EPR spectrum of TOTAPOL has an inhomogeneous linewidth that spans larger than the nuclear Larmor frequency $\Delta \geq |\boldsymbol{\omega_{0I}}|$, which is an important criterion for the CE to take place. Figure adapted with permission from [19]. (Fig source : SE_combined.ai)

2.1.2 Cross Effect

The CE was first discovered by Hwang and Hill in 1967 when they observed that the distance between the maxima in DNP field profiles decreases when higher concentrations of radical are used.[8,20] The CE mechanism essentially is a three-spin effect involving two coupled electrons and one nuclei, and it occurs when the difference in electron resonance frequencies of the two electrons matches the nuclear Larmor frequency, $\omega_{0S1} - \omega_{0S2} = \pm\omega_{0I}$ (Figure 3). The CE matching condition was optimally exploited by Hu et al.,[21] who mixed two different radicals whose resonance frequencies are separated by $\sim\omega_{0I}$. The

resulting DNP enhancement factor was significantly higher than if only a single kind of radical was used. Nevertheless, the advantages of exploiting the CE mechanism were not realized until the introduction of biradicals,[22,23] e.g. TOTAPOL (Figure 7), which is formed by tethering two monomeric TEMPO radicals together with a linker. The resulting enhancement factor showed a significant improvement over the SE mechanism under MAS conditions. Additionally, the concentration of radical required is usually lower, i.e. typically around 10 mM, compared to ~40 mM for the SE. This is beneficial for biological applications if the interaction between the biological sample and the radicals is a concern.[24]

The underlying mechanism of the CE has been explained theoretically with a quantum-mechanical description for both the static[12,25] and the MAS cases.[14,26] In the theoretical analysis presented in the literature, the perturbation treatment was applied twice because there is no off-diagonal term that connects the two degenerate energy eigenstates directly. We will present an alternate and novel approach in this article using fictitious operators treated with AHT.[27] We prefer such a derivation because it is a generic non-perturbative approach with minimal approximations, i.e. we obtain the lowest order solution or effective Hamiltonian only once instead of twice as is the case in previous literature. We will begin with a generic Hamiltonian for a three-spin system:

$$\begin{aligned}\hat{\mathcal{H}}(t) = d\left(3\hat{S}_{1z}\hat{S}_{2z} - \hat{S}_1 \cdot \hat{S}_2\right) - 2J\hat{S}_1 \cdot \hat{S}_2 + A_{zz}\hat{S}_{1z}\hat{I}_z + B_{zx}\hat{S}_{1z}\hat{I}_x \cdots \\ + A_{zz2}\hat{S}_{2z}\hat{I}_z + B_{zx2}\hat{S}_{2z}\hat{I}_x + \omega_{0S1}\hat{S}_{1z} + \omega_{0S2}\hat{S}_{2z} - \omega_{0I}\hat{I}_z,\end{aligned} \tag{10}$$

where d and J represent the dipolar coupling and the exchange interaction between the two electrons, respectively. The variable $\omega_{0I/S}$ denotes the Larmor frequency of the respective I/S spin. Although there are eight energy levels described by $\psi = |een\rangle$ (Figure 3a), we are mainly interested in the middle four energy levels described by the electron-electron ZQ subspace $\hat{\mathcal{H}}^{CE}$, i.e. $|\alpha\beta\alpha\rangle$, $|\alpha\beta\beta\rangle$, $|\beta\alpha\alpha\rangle$ and $|\beta\alpha\beta\rangle$. We can isolate this subspace because these four energy levels are not connected to any of the other four

energy levels by any off-diagonal elements in the absence of microwave irradiation. We can write down the matrix representation of the $\widehat{\mathcal{H}}^{\mathrm{CE}}$ subspace as

$$\widehat{\widehat{\mathcal{H}}} = \frac{1}{4} \times \cdots$$

$$\begin{bmatrix} \Delta A_{\mathrm{zz}} + 2(J - d + \Delta\omega - \omega_{0\mathrm{I}}) & \Delta B_{\mathrm{zx}} & -2(2J + d) & 0 \\ \Delta B_{\mathrm{zx}} & -\Delta A_{\mathrm{zz}} + 2(J - d + \Delta\omega + \omega_{0\mathrm{I}}) & 0 & -2(2J + d) \\ -2(2J + d) & 0 & -\Delta A_{\mathrm{zz}} + 2(J - d - \Delta\omega - \omega_{0\mathrm{I}}) & -\Delta B_{\mathrm{zx}} \\ 0 & -2(2J + d) & -\Delta B_{\mathrm{zx}} & \Delta A_{\mathrm{zz}} + 2(J - d - \Delta\omega + \omega_{0\mathrm{I}}) \end{bmatrix} \tag{11}$$

where $\Delta\omega = \omega_{0\mathrm{S1}} - \omega_{0\mathrm{S2}}$, $\Delta A_{\mathrm{zz}} = A_{zz} - A_{zz2}$, and $\Delta B_{\mathrm{zx}} = B_{\mathrm{zx}} - B_{\mathrm{zx2}}$. By comparing the matrix representation of the subspace here to that used to describe the two-spin solid effect (Equation 2), we observe that many terms have similar symmetrical properties and that prompts us to recognize that it is possible to express $\widehat{\mathcal{H}}^{\mathrm{CE}}$ as a product of two fictitious spin-$1/2$ operators, i.e. $\widehat{\mathcal{H}}^{\mathrm{CE}} = \hat{S}_1^{\mathrm{CE}} \otimes \hat{I}_2^{\mathrm{CE}}$. Thus,

$$\widehat{\mathcal{H}}^{\mathrm{CE}} = \frac{J - d}{2} \widehat{\mathbb{E}} + \Delta\omega \hat{S}_{\mathrm{z}}^{\mathrm{CE}} - \omega_{0\mathrm{I}} \hat{I}_{\mathrm{z}}^{\mathrm{CE}} - (2J + d) \hat{S}_{\mathrm{x}}^{\mathrm{CE}} + \Delta B_{\mathrm{zx}} \hat{S}_{\mathrm{z}}^{\mathrm{CE}} \hat{I}_{\mathrm{x}}^{\mathrm{CE}} + \Delta A_{zz} \hat{S}_{\mathrm{z}}^{\mathrm{CE}} \hat{I}_{\mathrm{z}}^{\mathrm{CE}}, \tag{12}$$

where $\widehat{\mathbb{E}}$ is the identity operator and it can be ignored as it commutes with all other terms. Note that by comparing the expression with Equation 1 for the SE case, the offset Ω and the nutation frequency, $\omega_{1\mathrm{s}}$,are now analogous to $\Delta\omega$ and $-(2J + d)$, respectively in the CE. Since the Hamiltonians and the matrix representation are similar in both cases, this ensures that the commutator relations are also satisfied in this space spanned by the fictitious spin- $1/2$ operators. Following that, the μw interaction-frame transformation performed in Equation 4 can also be applied here as the electron-electron couplings, $-(2J + d)$, are usually larger than the hyperfine ΔB_{zx} except in some extreme cases where the crystallite orientation yields $|2J + d| \leq |\Delta B_{\mathrm{zx}}|$. We are interested only in the transitions $|\alpha\beta\alpha\rangle \leftrightarrow |\beta\alpha\beta\rangle$ and $|\alpha\beta\beta\rangle \leftrightarrow |\beta\alpha\alpha\rangle$, which correspond exactly to DQ and ZQ transfers in the fictitious $\widehat{\mathcal{H}}^{\mathrm{CE}}$ space. Thus, with the justifications described, we can adapt the results from the SE case directly and write down the matching conditions

$$\omega_{0\mathrm{I}} = \pm\sqrt{(2J+d)^2 + \Delta\omega^2}$$
$$\sim \pm\,\Delta\omega \text{ if } |2J+d| \ll |\Delta\omega|, \tag{13}$$

and the build-up rate

$$\omega_{\mathrm{CE}} = \frac{\Delta B_{\mathrm{zx}}(2J+d)}{4\omega_{0\mathrm{I}}} \tag{14}$$

for the CE case directly. Our approach yields similar results as the ones derived by Thurber et al. using perturbation theory.[14] The build-up rate, ω_{CE}, characterizes the transfer rate from the initial density operator $\rho(0) = \hat{S}_{\mathrm{z}}^{\mathrm{CE}} \pm \hat{I}_{\mathrm{z}}^{\mathrm{CE}}$ to the optimum inversion $\rho(t) = -\left(\hat{S}_{\mathrm{z}}^{\mathrm{CE}} \pm \hat{I}_{\mathrm{z}}^{\mathrm{CE}}\right)$ when $t = (2\pi)/\omega_{\mathrm{CE}}$ in an ideal situation. In the following discussions, we focus on the initial state $\hat{S}_{\mathrm{z}}^{\mathrm{CE}} + \hat{I}_{\mathrm{z}}^{\mathrm{CE}}$, which dictates the population difference between $|\alpha\beta\alpha\rangle$ and $|\beta\alpha\beta\rangle$ in the lab-frame representation. Although the population difference of the stated pair is negligible during thermal equilibrium, it can be magnified via saturating either electron (Figure 3a), i.e. $\omega_{\mu\mathrm{w}} = \omega_{0\mathrm{S}1}$ or $\omega_{\mu\mathrm{w}} = \omega_{0\mathrm{S}2}$ for negative and positive transfer, respectively. Thus, the EPR saturation factor or CE transfer efficiency depends indirectly on the microwave nutation frequency $\omega_{1\mathrm{S}}$. Additionally, Ravera et al. have shown that the population difference can be generated by saturating either an electron involved in the CE directly (dCE), or other electrons that depolarize the CE electron pairs indirectly (iCE) via the electron spectral diffusion.[28]

In summary, the CE mechanism is a two-step process that involves first preparing a difference in population in the $\hat{\mathcal{H}}^{\mathrm{CE}}$ subspace by saturating either electron. Then, the polarization will be transferred to the opposite nuclear manifold (α or β) via the transition within the degenerate energy eigenstate pair $|\alpha\beta\alpha\rangle \leftrightarrow |\beta\alpha\beta\rangle$ (Equation 13). Note that the first step requires the microwave irradiation to saturate an EPR transition whereas the second step does not require instantaneous microwave irradiation to take place. Hence, it is not required that the two processes occur simultaneously and this unique feature was exemplified in the MAS case where the saturation and polarization steps happen at different rotor angles

(Figure 3b). The similar radiationless process also accounts for the depolarization effect in the absence of microwave irradiation (*vide infra*).[29,30]

In the description provided by Thurber et al. for the MAS case,[14] the population between the eigenstates changes when the energy levels become close but do not cross each other; these events are known as anti-level crossings. There are three important categories of events (Figure 3b) where anti-level crossings took place, namely: (1) the saturation of EPR transitions; (2) the difference in EPR frequencies matches the nuclear Larmor frequency, i.e. $\omega_{0S1} - \omega_{0S2} = \pm\omega_{0I}$, and (3) the exchange of state populations between two electrons. In the MAS experiment, the energy levels are modulated and become time-dependent. Thus, if the time at which the anti-level crossing occurs is sufficiently long, i.e. a slow process, the transition becomes adiabatic with the probability quantifiable by the Landau-Zener equation. The adiabatic frequency sweep facilitated by MAS without instantaneous microwave irradiation has a similar counterpart in the MAS-NMR experiment,[31] where Verel et al. demonstrated a homonuclear polarization transfer by sweeping the MAS frequency through the rotational resonance condition.[32]

We have demonstrated a theoretical analysis on the CE mechanism by focusing on the $\widehat{\mathcal{H}}^{\mathrm{CE}}$ subspace, which is a valid approach in the case of absent or weak ω_{1S} microwave irradiation. Secondly, we have neglected the relaxation effects by assuming that the relaxation rates are slow relative to coherent effects, which is valid in the low-temperature regime. If ω_{1S}, or the relaxation rates are large, the $\widehat{\mathcal{H}}^{\mathrm{CE}}$ subspace is no longer independent from the other eigenstates and it requires a different theoretical approach.

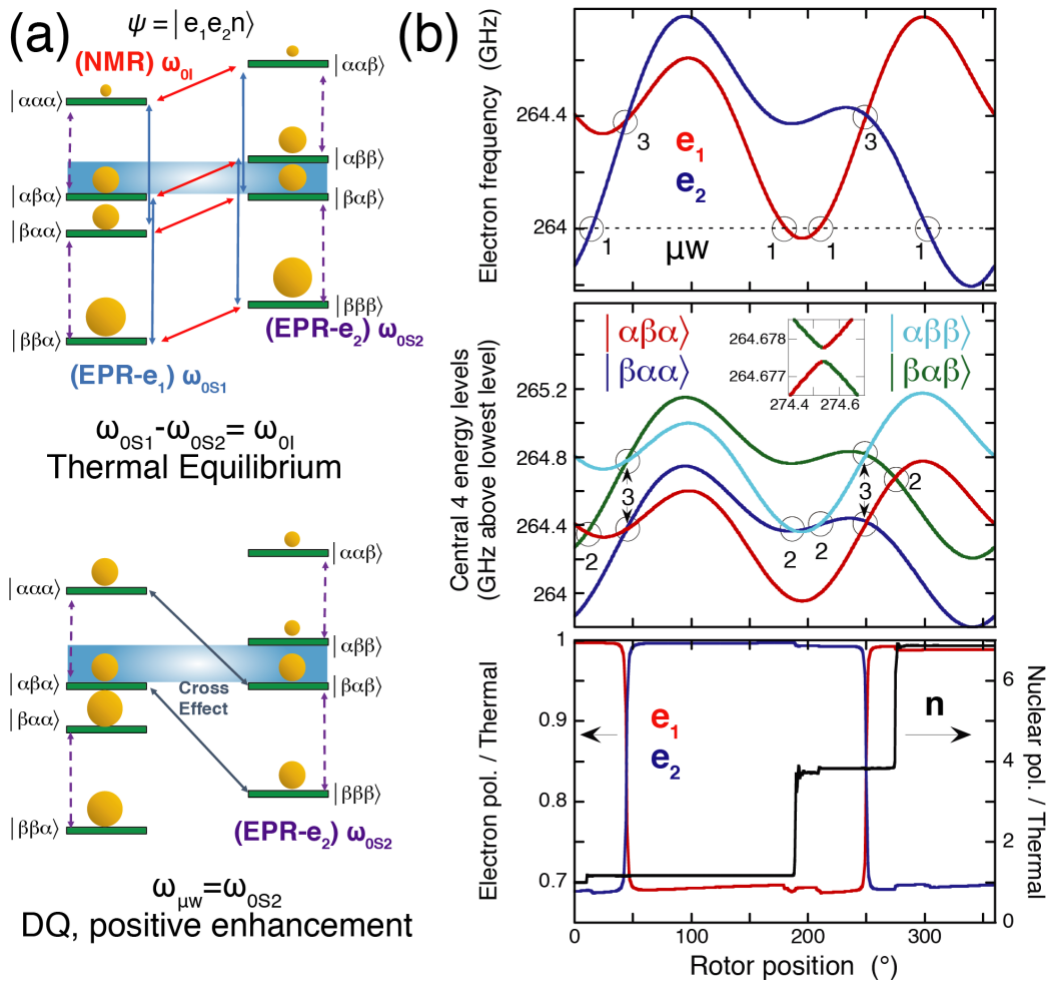

Figure 3: (a) Schematic diagram of the energy level diagram of a three-spin (two electrons and one nucleus) system exhibiting the CE-DNP mechanism. The event occurs when the energy levels of the states are close to each other, for e.g. $|\boldsymbol{\alpha\beta\alpha}\rangle$ and $|\boldsymbol{\beta\alpha\beta}\rangle$. Negative/positive enhancement can be obtained if the EPR transition of the first or second electron is saturated. (b) Energy-level diagram as a function of rotor angle in MAS. There are three important categories of events where anti-level crossings took place namely: (1) the saturation of EPR transition, (2) the CE matching condition $\boldsymbol{\omega_{0S1} - \omega_{0S2} = \pm\omega_{0I}}$, and (3) the exchange of populations between two electrons. Figure adapted with permission.[14] (Fig source : CE_level.ai)

2.1.3 Overhauser Effect

The OE was first predicted theoretically by Overhauser and later confirmed by Carver and Slichter experimentally on a sample of lithium metal.[7] Subsequently, the nuclear counterpart of the OE, also known as the Nuclear Overhauser Effect (NOE), has been used extensively to obtain distance

measurements in biological samples. In DNP, the OE mechanism originates from either the dipolar or scalar relaxation mechanism. When anisotropic interactions such as dipolar couplings are modulated by stochastic motions such as rotational and translational diffusion, the fluctuation in the local dipolar fields induces the dipolar relaxation mechanism. On the other hand, scalar relaxation originates from the modulation of the exchange interaction, *J*, due to either chemical exchange processes (scalar relaxation of the first kind), or by a scalar coupling to a spin that relaxes quickly (scalar relaxation of the second kind). In principle, both the scalar-mediated ZQ (W_0) and dipolar-mediated DQ (W_2) relaxation pathways (Figure 2a) coexist and they affect both the electron and nuclei populations at thermal equilibrium. If the EPR single-quantum transitions are saturated by microwave irradiation, the populations of the four eigenstates will be redistributed and the system reaches a new steady state, which can result in an enhanced NMR signal. The enhancement will either be positive if the ZQ's contribution is larger, or negative if it is dominated by DQ relaxation. The Overhauser effect can be described by the Solomon equations at the phenomenological level[33] and only a simplified theoretical derivation will be shown here. Let us consider a two-spin system with the rate of change of the population of the respective states (Figure 2a) given by

$$\begin{aligned} dN_1/dt &= -(W_\mathrm{I} + W_\mathrm{S} + W_2)N_1 + W_\mathrm{S}N_3 + W_\mathrm{I}N_2 + W_2N_4 \\ dN_2/dt &= -(W_\mathrm{I} + W_\mathrm{S} + W_0)N_2 + W_\mathrm{S}N_4 + W_\mathrm{I}N_1 + W_0N_3 \\ dN_3/dt &= -(W_\mathrm{I} + W_\mathrm{S} + W_0)N_3 + W_\mathrm{S}N_1 + W_\mathrm{I}N_4 + W_0N_2 \\ dN_4/dt &= -(W_\mathrm{I} + W_\mathrm{S} + W_2)N_4 + W_\mathrm{S}N_2 + W_\mathrm{I}N_3 + W_2N_1, \end{aligned} \tag{15}$$

where $N_\mathrm{i} = n_\mathrm{i} - n_\mathrm{i,eq}$ denotes the difference between the instantaneous population n_i and that during the equilibrium $n_\mathrm{i,eq}$, $W_\mathrm{I/S}$ symbolizes the longitudinal relaxation rate $1/T_1$ of the *I* or *S* spin, while W_0 and W_2 represent the ZQ and DQ relaxation rates, respectively. Following that, by recognizing that $I_z = n_1 - n_2 + n_3 - n_4$ and $S_z = n_1 - n_3 + n_2 - n_4$, one can obtain

$$dI_z/dt = -\rho_I(I_z - I_{z,eq}) - \sigma(S_z - S_{z,eq})$$
$$dS_z/dt = -\rho_S(S_z - S_{z,eq}) - \sigma(I_z - I_{z,eq}), \quad (16)$$

where $\rho_{I/S} = W_0 + 2W_{I/S} + W_2$ is the auto-relaxation rate constant and $\sigma = W_2 - W_0$ is the cross-relaxation rate constant. Hence, by considering the system to be in equilibrium, $dI_z/dt = 0$ and $\langle S_{z,eq}\rangle/\langle I_{z,eq}\rangle = \gamma_S/\gamma_I$, one can obtain

$$\varepsilon = \frac{\langle I_z\rangle - \langle I_{z,eq}\rangle}{\langle I_{z,eq}\rangle} = \frac{s\sigma\gamma_S}{\rho_I\gamma_I}, \quad (17)$$

in which the saturation factor, $s = 1 - \langle S_z\rangle/\langle S_{z,eq}\rangle$ describes the degree of saturation of the EPR transitions. In principle the enhancement, ε, can be either positive or negative depending on $\sigma = W_2 - W_0$. Likewise, the system may lose polarization in the case that $|\varepsilon| < 1$. A more generic definition of enhancement factor, $\varepsilon = -\xi f s\gamma_S/\gamma_I$, has been defined in the literature where the coupling factor, $\xi = \sigma/\rho_I$ describes the efficiency of the OE, and has value ranging from -1 to 0.5. Furthermore, the leakage factor, f, accounts for the relaxation effect due to the addition of radicals. Further in-depth discussion and analysis of the parameters are well documented in the literature.[34-36]

As the OE relies on the stochastic motion of mobile electrons, it was believed that the mechanism is present only in solutions or conducting solids.[34,37] Nevertheless, a recent publication by Can et al.[38] has reported an observation of the Overhauser effect in an insulating solid using BDPA or water-soluble SA-BDPA as the radical. Furthermore, the author reported an unexpected finding that the enhancement factor increases with increasing static magnetic field (Figure 4a). The discovery of this effect in insulating solids and the unexpected dependence of enhancement on the magnetic field has sparked an interest in the community to pursue further investigation and theoretical explanation. Pylaeva et al. have proposed that the Overhauser effect exhibited by BDPA could be due to the modulation of the hyperfine coupling by the flipping in the bond orders in the radical.[39] Their molecular dynamics (MD) simulations have predicted

that the hyperfine modulation has a broad frequency spectrum ranging from 200 to 750 GHz, with a maximum at ~ 650 GHz. Nevertheless, the recent observation of the OE on the same radical at 1.2 K[40] implies that some other mechanism, not involving bond motion, may be responsible.

The effect of the sample preparation and MAS frequency (Figure 4b) on the enhancement factor were also studied extensively.[41] For instance, an enhancement factor of ~ 80 was obtained when BDPA is dissolved in ortho-terphenyl (OTP) compared to ~ 20 in PS.[42] Furthermore, an improvement in the enhancement factor could be obtained if the paramagnetic oxygen is removed via degassing.[40]

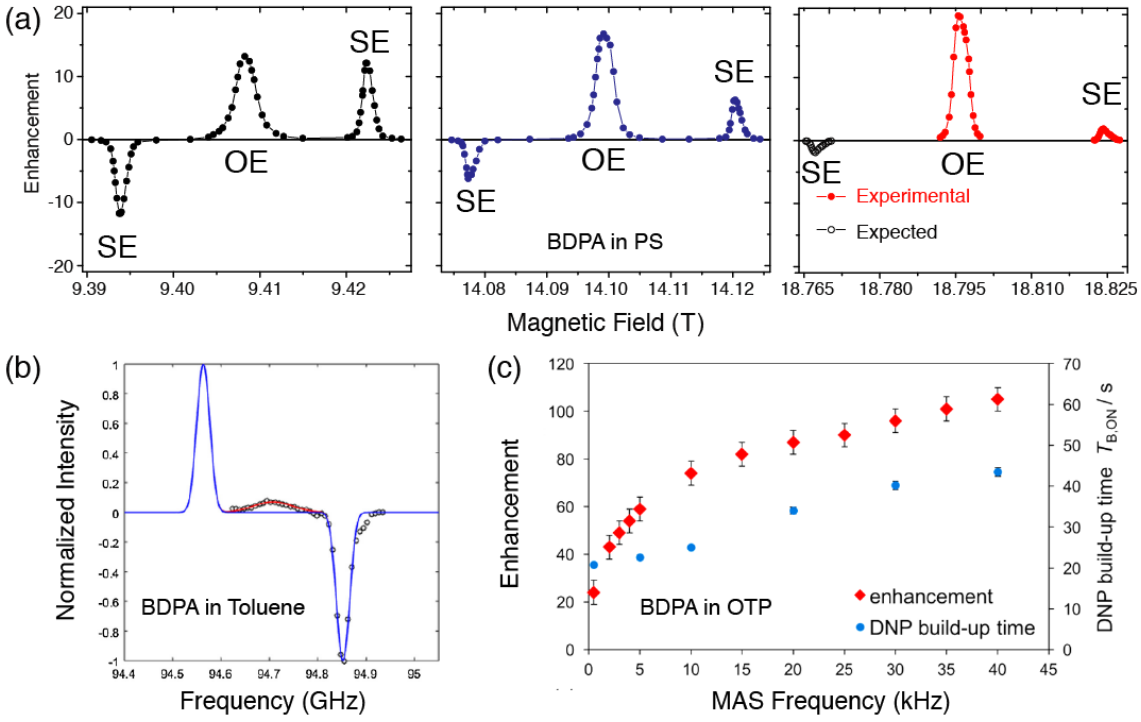

Figure 4: Overhauser-DNP enhancement of BDPA dispersed in (a) polystyrene, (b) toluene, or (c) OTP. Figure (c) shows the dependence of the OE enhancement at 18.8 T as a function of MAS frequency (red) and build-up time (blue). The OE exhibits the highest enhancement at 18.8 T. Figures are adapted with permission from [38,43,44]. (*OE_Thach_FieldProfile_2.png *)

2.1.4 Thermal Mixing

The TM process is one of the four CW-DNP mechanisms that is particularly important in the case of dissolution DNP at low temperatures ($T \leq 20$ K).[45] During the polarization step in most DNP

experiments at low temperatures, multiple DNP mechanisms can take place simultaneously, namely the SE, CE and TM. However, the TM process becomes dominant relative to other DNP mechanisms if the EPR spectrum is broad enough to cover the nuclear Larmor frequency, i.e. $\Delta\omega_e \geq \omega_{0I}$. Although the EPR linewidth can be broadened homogeneously due to increased electron-electron dipolar coupling when high concentration of radical is used, or inhomogeneously due to large *g*-anisotropy, it was reported that the former process is the dominant contribution to the TM effect.[46] Unlike other DNP processes, the TM mechanism was described by Provotorov and Borghini using a classical thermodynamic model.[1,9,47] In this model, the polarization transfer from electron to nuclei is described analogously to the flow of heat (polarization) between different reservoirs (spin types) due to the difference in temperature (populations). Thus, the concepts of a Zeeman/dipolar bath and spin/lattice temperatures were introduced and applied in the mathematical description of the thermodynamic model. We refer readers to the recent review by Wenckebach for a comprehensive summary of the thermodynamic model.[48] Alternate approaches using quantum-mechanical descriptions have also been presented recently and it was shown that TM occurs in a multiple-spin system involving a nucleus and more than two electrons, which makes TM a distinguishable process from the CE.[46,49] The quantum mechanical approaches yield good agreement with experimental data and show convergence with the concept of spin temperature in the thermodynamic approach. We will not discuss further the topic of TM as the effect is insignificant in MAS-DNP experiment at temperatures above 80 K.

2.2 Pulsed DNP

We have provided a brief theoretical description of the CW-DNP mechanisms, which aimed at transferring polarization via saturating the transition between energy levels rather than manipulating spin coherences. Nevertheless, the saturation-based CW techniques usually have enhancement factors that exhibit dependence on the static magnetic field. On the contrary, pulsed DNP techniques mediate polarization transfer via a coherent pathway, which can have an enhancement factor that is field-independent in principle. An important criterion for pulsed DNP to work is that the microwave power

must be sufficiently strong to overcome the relaxation rates and invert the spin polarization. This feature allows DNP to be performed at higher temperatures with less compromise to the enhancement factor, in comparison to the CW technique. Several instances of pulsed DNP experiments have been demonstrated to yield decent enhancement factors at room temperature and at a magnetic field of 0.35 T.[50-52] Both the field-independent enhancement and viability at higher temperatures pose a promising prospect that pulsed DNP can outperform CW techniques for biological applications. We will discuss two main categories of pulsed DNP techniques, namely those with and without simultaneous rf irradiation on the nuclei involved. We shall see that the implementation, terms of hyperfine interactions used, and the effects of them are rather different in these two categories.

2.2.1 Pulsed DNP with rf Irradiation

Two pulse sequences will be discussed here, namely DNP in the Nuclear Rotating Frame (NRF-DNP)[53-55] and the Dressed-State Solid Effect (DSSE).[56] Apart from the presence of rf irradiation during the polarization period (Figure 5) that makes these two sequences distinct from other DNP techniques, both NRF-DNP and DSSE exploit the secular hyperfine coupling A_{zz} rather than the non-secular contributions B_{zx} to mediate polarization transfer. The main consequence of using the secular contribution is that the technique can possibly be applied to liquid state samples. Secondly, the theory doesn't indicate any unfavorable scaling of the enhancement with the static magnetic field, assuming ideal conditions. Although there is limited experimental evidence for the theoretical claim, the validity is worthy of a comprehensive investigation. We will begin with a general Hamiltonian for a two-spin system before considering individual sequences:

$$\widehat{\mathcal{H}} = \Omega\hat{S}_{\mathrm{z}} + \omega_{1\mathrm{S}}\hat{S}_{\mathrm{x}} - \omega_{0\mathrm{I}}\hat{I}_{\mathrm{z}} + 2\omega_{1\mathrm{I}}\cos(\omega_{\mathrm{rf}}t)\,\hat{I}_{\mathrm{x}} + A_{\mathrm{zz}}\hat{S}_{\mathrm{z}}\hat{I}_{\mathrm{z}} + B_{\mathrm{zx}}\hat{S}_{\mathrm{z}}\hat{I}_{\mathrm{x}}$$

$$\widehat{U}_{\mathrm{t}}^{-1}\widehat{\mathcal{H}}\widehat{U}_{\mathrm{t}} = \omega_{\mathrm{eff}}^{(\mathrm{S})}\hat{S}_{\mathrm{z}} - \omega_{0\mathrm{I}}\hat{I}_{\mathrm{z}} + 2\omega_{1\mathrm{I}}\cos(\omega_{\mathrm{rf}}t)\,\hat{I}_{\mathrm{x}} + \left(A_{\mathrm{zz}}\hat{I}_{\mathrm{z}} + B_{\mathrm{zx}}\hat{I}_{\mathrm{x}}\right)\left(\hat{S}_{\mathrm{z}}\cos\theta - \hat{S}_{\mathrm{x}}\sin\theta\right), \quad (18)$$

where in the second line we performed a rotation with $\hat{U}_{\mathrm{t}} = \exp\left(-i\theta\hat{S}_{\mathrm{y}}\right)$ with the angle θ given by $\theta = \tan^{-1}(\omega_{1\mathrm{s}}/\Omega_{\mathrm{s}})$, so that the *z*-axis is along the effective field $\omega_{\mathrm{eff}}^{(\mathrm{S})} = \sqrt{\omega_{1\mathrm{s}}^2 + \Omega_{\mathrm{s}}^2}$. Then, we go into the rf interaction-frame with $\hat{U}_{\mathrm{rf}} = \exp\left(-i\left(-\omega_{\mathrm{rf}}\hat{I}_{\mathrm{z}}\right)t\right)$:

$$\hat{U}_{\mathrm{rf}}^{-1}\hat{U}_{\mathrm{t}}^{-1}\hat{\mathcal{H}}\hat{U}_{\mathrm{t}}\hat{U}_{\mathrm{rf}} = \omega_{\mathrm{eff}}^{(\mathrm{S})}\hat{S}_{\mathrm{z}} + \Omega_{\mathrm{I}}\hat{I}_{\mathrm{z}} + \omega_{1\mathrm{I}}\hat{I}_{\mathrm{x}} + A_{\mathrm{zz}}\cos\theta\,\hat{S}_{\mathrm{z}}\hat{I}_{\mathrm{z}} - A_{\mathrm{zz}}\sin\theta\,\hat{S}_{\mathrm{x}}\hat{I}_{\mathrm{z}}, \tag{19}$$

where $\Omega_{\mathrm{I}} = \omega_{0\mathrm{I}} - \omega_{\mathrm{rf}}$ is the rf offset frequency. Note that the non-secular term B_{zx} vanishes when using a high-field approximation. Similarly, if we now tilt the Hamiltonian such that the *z*-axis of the nuclear frame is directed along the effective field $\omega_{\mathrm{eff}}^{(\mathrm{I})}$:

$$\begin{aligned}\hat{\bar{\mathcal{H}}} = A_{\mathrm{zz}}\big(&\cos\theta\cos\varphi\,\hat{S}_{\mathrm{z}}\hat{I}_{\mathrm{z}} - \cos\theta\sin\varphi\,\hat{S}_{\mathrm{z}}\hat{I}_{\mathrm{x}} - \sin\theta\cos\varphi\,\hat{S}_{\mathrm{x}}\hat{I}_{\mathrm{z}} + \sin\theta\sin\varphi\,\hat{S}_{\mathrm{x}}\hat{I}_{\mathrm{x}}\big)\cdots \\ &+\omega_{\mathrm{eff}}^{(\mathrm{S})}\hat{S}_{\mathrm{z}} + \omega_{\mathrm{eff}}^{(\mathrm{I})}\hat{I}_{\mathrm{z}},\end{aligned} \tag{20}$$

where $\varphi = \tan^{-1}(\omega_{1\mathrm{I}}/\Omega_{\mathrm{I}})$. We have now obtained a simplified Hamiltonian in the double-rotating frame, which will be used subsequently for the NRF-DNP and DSSE cases. In NRF-DNP, off-resonance microwave irradiation with on-resonance spin-locking rf pulses are implemented, whereas DSSE has an opposite scenario, i.e. on-resonance spin-locking microwave pulses with off-resonance rf irradiation. The consequences of the two different implementations will be discussed in the following subsections.

2.2.1.1 NRF-DNP

The NRF-DNP experiment exploits an on-resonance rf irradiation ($\varphi = \pi/2$) (Figure 5a) and for a far off-resonance microwave irradiation (small θ for $|\omega_{1\mathrm{s}}/\Omega_{\mathrm{s}}| \ll 1$). Hence, we can simplify Equation 20 to become

$$\hat{\bar{\mathcal{H}}} \approx \omega_{\mathrm{eff}}^{(\mathrm{S})}\hat{S}_{\mathrm{z}} + \omega_{1\mathrm{I}}\hat{I}_{\mathrm{z}} - A_{\mathrm{zz}}\hat{S}_{\mathrm{z}}\hat{I}_{\mathrm{x}}\,. \tag{21}$$

By inspecting the resulting Hamiltonian (Equation 21), one can see that it has a similar form as the Hamiltonian for the SE (Equation 1) except that the off-diagonal term here is contributed by the secular

A_{zz} term. Hence, a similar state mixing is also expected for driving the DQ and ZQ transitions in the rotating frame, with the degree of mixing $\eta = \tan^{-1}(A_{zz}/2\omega_{1I})$.[15] Following that, it is trivial to diagonalize the Hamiltonian (Equation 21) with $\hat{U} = \exp\left(-i\left(-\eta 2\hat{S}_z\hat{I}_y\right)t\right)$ and obtain the eigenvalues needed to determine the matching condition:

$$\omega_{eff}^{(S)} = \pm\sqrt{(A_{zz}/2)^2 + \omega_{1I}^2}$$
$$\Omega_S \sim \pm\sqrt{(A_{zz}/2)^2 + \omega_{1I}^2} \quad (22)$$

where we have considered the case for $|\omega_{1S}/\Omega_S| \ll 1$ in the second line. The matching conditions imply that the separation between the DQ and ZQ conditions is much smaller than the case expected for the solid effect, i.e. $2\omega_{0I}$ (Figure 5a). An enhancement factor of ~ 0.89 was measured.[55] Although this enhancement factor may be considered to be small, the real experimental advantage comes indirectly from the short T_1 of electrons relative to nuclei. The low enhancement factor could be rationalized by the fact that the polarization is built up along the spin-lock axis, which has a relaxation time $T_{1\rho}$ (~ 27 ms) several orders of magnitude smaller than T_1 (~ 1056 s). This could hamper the enhancement factor when $T_{1\rho}$ becomes comparable or smaller than the spin diffusion timescale.

2.2.1.2 DSSE

We have mentioned that the DSSE sequence has an opposite pulsing regime compared to NRF-DNP, i.e. $\theta = \pi/2$ (Figure 5b) and small φ for the case $|\omega_{1I}/\Omega_I| \ll 1$. Hence, we can simplify Equation 20 to become

$$\hat{\tilde{\mathcal{H}}} \approx \omega_{eff}^{(I)}\hat{I}_z + \omega_{1S}\hat{S}_z - A_{zz}\hat{S}_x\hat{I}_z \,. \quad (23)$$

This is similar to the Hamiltonian for NRF-DNP (Equation 21), except that the spin part of the off-diagonal term here is $\hat{S}_x\hat{I}_z$ instead of $\hat{S}_z\hat{I}_x$. Likewise, the Hamiltonian (Equation 23) can be diagonalized with $\hat{U} = \exp\left(-i\left(-\eta 2\hat{S}_y\hat{I}_z\right)t\right)$ with $\eta = \tan^{-1}(A_{zz}/2\omega_{1S})$, and the matching conditions are given as

$$\omega_{\text{eff}}^{(\text{I})} = \pm\sqrt{(A_{zz}/2)^2 + \omega_{1S}^2}$$

$$\Omega_I \sim \pm\,\omega_{1S}, \tag{24}$$

where we have considered the case for $|\omega_{1I}/\Omega_I| \ll 1$ and $A_{zz} \ll \omega_{1S}$ in the second line. Although the enhanced nuclear signal was not observed directly, there are indications of polarization transfer via monitoring the loss of electron polarization and also via numerical simulations[56] (Figure 5b). Nonetheless, The fact that the microwave irradiation is applied directly on-resonance on the EPR line has allowed the possibility of employing electron decoupling during NMR detection.[57]

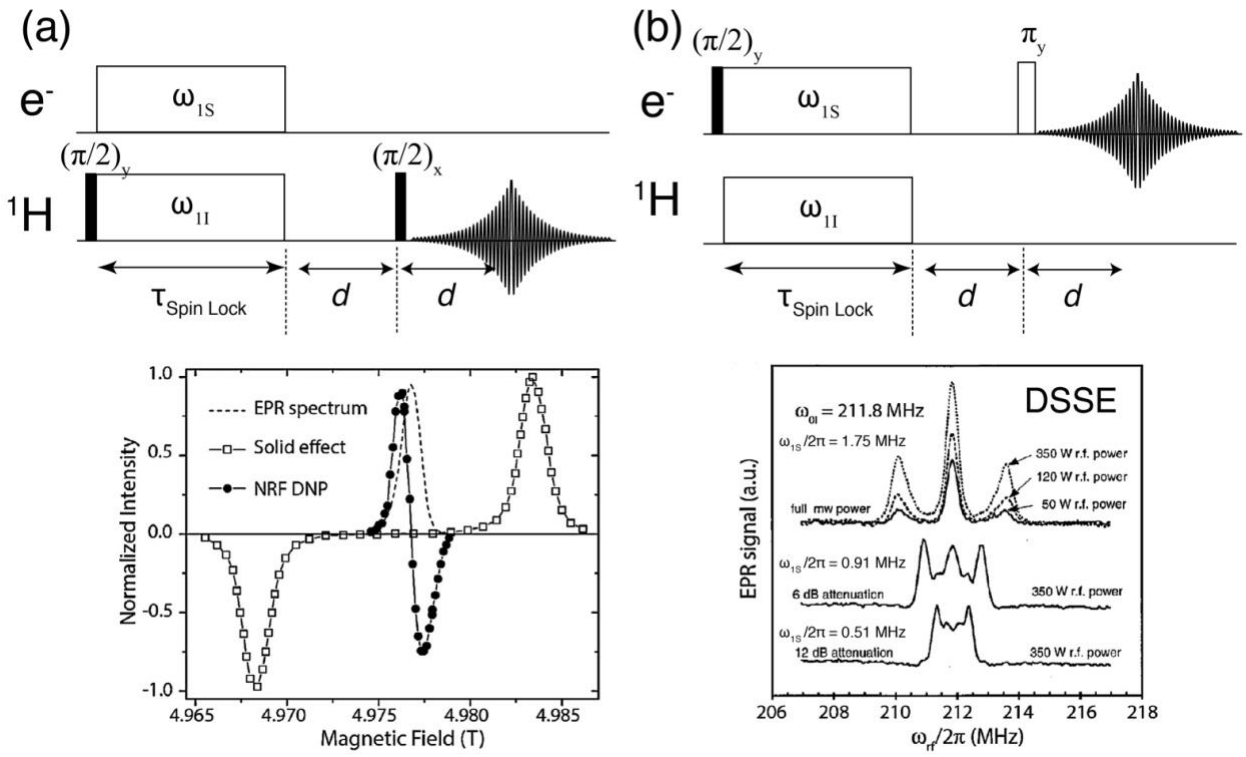

Figure 5: Schematic diagram of the pulse sequences (a) NRF-DNP with NMR detected using solid echo and (b) DSSE with EPR signal detected using spin echo, at ~5 T. An enhancement factor of less than 1 is obtained for NRF-DNP while the nuclear enhancement was not directly observable in the DSSE case. Figures adapted with permission from [55,56,58]. (source: NRF_DNP_DSSE.ai)

2.2.2 Pulsed DNP without rf Irradiation

There are in general three different types of pulsed DNP sequences that employ only microwave irradiation, namely Nuclear Orientation Via Electron Spin Locking (NOVEL), frequency-swept Integrated Solid Effect (ISE), and Time-Optimized Pulsed DNP (TOP-DNP). These pulsed DNP sequences are in general more favorable and have promising prospects for several reasons. Firstly, any rotation of the NMR polarization away from the z-axis induced by the RF pulses will inevitably result in faster decay in NMR signal due to transverse relaxation. Secondly, the precession frequencies of the nuclei might be shifted away from the Larmor frequency due to distance-dependent hyperfine interactions. This causes an additional complication when choosing the frequency for the RF pulses. Therefore, we will emphasize this category of pulsed DNP techniques as they have been demonstrated experimentally to be more robust.

2.2.2.1 Nuclear Orientation via Electron Spin-Locking (NOVEL)

The NOVEL technique matches the Rabi frequency that spin locks the electron spins to the nuclear Larmor frequency.[59,60] When the matching condition ($\omega_{1S} = \omega_{0I}$) is fulfilled (Figure 6a and b), the presence of dipolar interactions allow a resonant transfer of polarization from the electrons to the nuclei, an idea similar to the Hartmann-Hahn cross-polarization technique.[61] The derivation of the Hamiltonian can be shown starting with a Hamiltonian that is similar to the case for the SE (Equation 1) except that the microwave irradiation is applied on resonance $\Omega = 0$:

$$\hat{\mathcal{H}} = -\omega_{0I}\hat{I}_z + A_{zz}\hat{S}_z\hat{I}_z + B_{zx}\hat{S}_z\hat{I}_x + \omega_{1s}\hat{S}_x \,. \tag{25}$$

Then, an interaction-frame transformation with respect to the term $\hat{U}_1 = \exp\left(-i\left(\omega_{1S}\hat{S}_x - \omega_{0I}\hat{I}_z\right)t\right)$ is performed to yield

$$\begin{aligned}\hat{\tilde{\mathcal{H}}}(t) &= \hat{U}_1^{-1}(t)\hat{\mathcal{H}}\hat{U}_1(t) - \left(\omega_{1S}\hat{S}_x - \omega_{0I}\hat{I}_z\right) \\ &= \left(A_{zz}\hat{I}_z + B_{zx}\left(\hat{I}_x\cos\omega_{0I}t + \hat{I}_y\sin\omega_{0I}t\right)\right)\left(\hat{S}_z\cos\omega_{1S}t + \hat{S}_y\sin\omega_{1S}t\right).\end{aligned} \tag{26}$$

Similarly, the Hamiltonian becomes time-independent at the conditions $\omega_{1S} = \pm\omega_{0I}$ upon integration:

$$\hat{\bar{\mathcal{H}}} = \frac{\omega_{0I}}{2\pi}\int_0^{(2\pi)/\omega_{0I}} \hat{\tilde{\mathcal{H}}}(t)\,dt = \frac{B_{zx}}{2}\left(\hat{S}_z\hat{I}_x \pm \hat{S}_y\hat{I}_y\right) \text{ if } \omega_{1S} = \pm\omega_{0I}, \tag{27}$$

where the Hamiltonian (Equation 27) dictates a DQ condition if the electron polarization is spin locked along the microwave field ($\omega_{1S} = \omega_{0I}$), or ZQ condition if they are antiparallel ($\omega_{1S} = -\omega_{0I}$). The sequence has been shown to be robust and yields enhancement factors >300 in perdeuterated system at 0.35 T.[52,62] Additionally, it was demonstrated recently that the enhancement factor can be increased further by a factor of 1.6 by making the sequence adiabatic, i.e. sweeping the microwave Rabi frequency across the matching condition using an arbitrary waveform generator (AWG).[63] In such sequences, longer spin lock pulses are required to fulfil the adiabatic condition, and a microwave source capable of a higher duty cycle is required. A known challenge of implementing NOVEL at higher fields is the requirement of high microwave Rabi frequencies. It was shown that this issue can be mitigated by exploiting the off-resonance NOVEL condition $\left(\sqrt{\omega_{1s}^2 + \Omega^2} = \omega_{0I}\right)$,[64] similar to the SPECIFIC-CP sequence in solid-state NMR.[65]

2.2.2.2 Integrated Solid Effect (ISE)

Due to the NOVEL matching condition being technically demanding at higher fields, the ISE is an alternative sequence that can be implemented at lower Rabi frequencies.[66-68] The ISE sequence was first demonstrated by sweeping the magnetic field through both SE matching conditions (Figure 6c and

d), e.g., from $\Omega \ll -\omega_{0I}$ to $\Omega \gg \omega_{0I}$ within a short time period (~T_{1e}). This approach might appear to be counterintuitive because the ZQ and DQ matching conditions yield nuclear polarizations of opposite sign. However, the electron polarization is also inverted during the adiabatic process and hence the polarization transfer adds constructively. In order to perform the ISE at higher fields, the magnetic field has to be swept by ~ 28 mT within 1 ms in a 9.4 T/ 400 MHz magnet. This is technologically challenging and the field drift after the sweep makes the sequence inappropriate for NMR applications at higher fields. Alternatively, the offset frequencies Ω can be manipulated by changing the microwave frequency while keeping the magnetic field constant. Such frequency modulation schemes were demonstrated to improve the enhancement by a factor of ~2-3 at both 3.34 T (95 GHz) and 6.7 T (188 GHz) on TEMPOL at temperatures (10-50 K) favoring TM.[69,70] The frequency modulation schemes were performed by changing the microwave carrier frequencies directly via a voltage-controlled oscillator (VCO). Alternatively, the frequency modulation can also be implemented by generating a microwave pulse train of varying phases using an arbitrary waveform generator (AWG), while having the same carrier frequency. It was demonstrated recently that such frequency-swept ISE experiments performed at $\omega_{1S} =$ 1.5 MHz ($\sim 0.1\ \omega_{0I}$) can yield similar enhancements compared to the ISE at the NOVEL condition ($\omega_{1S} =$ 15 MHz) 0.35 T.[71] Such a low-power pulsed DNP sequence could be potentially implemented experimentally at higher fields upon the availability of gyro-amplifiers (*vide infra*) or other high-power controllable microwave sources. Nonetheless, so far most ISE experiments have been performed at static conditions and its effect under MAS condition is still uncertain. This is further complicated by the additional modulation of the *g* tensor or offset frequencies.

2.2.2.3 Time-Optimized Pulsed DNP (TOP-DNP)

We have discussed pulsed DNP sequences that achieve DNP matching conditions by either setting the Rabi (NOVEL) or offset (SE/ISE) frequencies. We have recently introduced a new class of pulsed DNP sequence, which mediates the polarization transfer via a train of microwave pulses, τ_p, and delays, d, of optimal timings (Figure 6e), i.e. TOP-DNP (Time-Optimized Pulsed DNP). The design of

the sequence was inspired by the dipolar recoupling sequences in MAS-NMR experiments.[72] In the recoupling experiments, averaged anisotropic interactions like dipolar couplings can be reintroduced via rotor-synchronized pulses like radio frequency-driven recoupling (RFDR)[73] during the mixing time to transfer polarization. Similarly, the averaging of the pseudo-secular term B_{zx} by the Larmor interaction $\omega_{0\mathrm{I}}\hat{I}_{\mathrm{z}}$ is inhibited and restored to transfer polarization in TOP-DNP, i.e. hyperfine recoupling. A brief theoretical analysis of the pulse sequence using Floquet theory[74,75] is discussed here. There are three characteristic frequencies[76,77] involved in the TOP-DNP sequence, namely the nuclear Larmor frequency, $\omega_{0\mathrm{I}}$, modulation frequency, $\omega_{\mathrm{m}} = 2\pi/(\tau_{\mathrm{p}} + d)$, and the effective field, ω_{eff}. ω_{eff} is defined as the net rotation angle, β_{eff}, over the cycle time, τ_{m}, of a periodic sequence. An effective Hamiltonian can be obtained if there exists a linear combination of the characteristic frequencies that satisfies the resonance conditions:

$$\omega_{0\mathrm{I}} + k\omega_{\mathrm{m}} \pm \omega_{\mathrm{eff}} = 0, \tag{28}$$

where k is an integer number. There are in principle many different resonance conditions exploiting different values of k. We show that the effective Hamiltonian for the simplest condition, $\omega_{\mathrm{m}} + \omega_{\mathrm{eff}} = \omega_{0\mathrm{I}}$, is given by

$$\hat{\bar{\mathcal{H}}}^{(1,-1,-1)} + \hat{\bar{\mathcal{H}}}^{(-1,1,1)} = \frac{B}{4}\left(a_{-}^{(-1,-1)}\hat{S}^{-}\hat{I}^{-} + a_{+}^{(-1,-1)}\hat{S}^{+}\hat{I}^{-} + 2a_{\mathrm{z}}^{(-1,-1)}\hat{S}_{\mathrm{z}}\hat{I}^{-}\right) + c.c, \tag{29}$$

where *c.c.* stands for complex conjugate, $\hat{S}^{\pm} = \hat{S}_{\mathrm{x}} \pm i\hat{S}_{\mathrm{y}}$ are the ladder operators, and $a_{\pm}^{(k,l)}$ are the Fourier coefficients. The first two terms in the effective Hamiltonian (Equation 29) are responsible for driving the DQ and ZQ transfers, respectively. It can be shown that the strengths of the Fourier coefficients $a_{+,-}^{(-1,-1)}$as a function of the offset frequencies give rise to oscillatory enhancements in the field profile (Figure 6f). This sequence yields a broadband DNP field profile spanning a bandwidth of $4\omega_{0\mathrm{I}}$ with a maximum enhancement of ~200 at 0.35 T. Furthermore, the effective Hamiltonian (Equation

29) suggests that the enhancement factor is field-independent as long as the Rabi frequency is scaled proportionally.

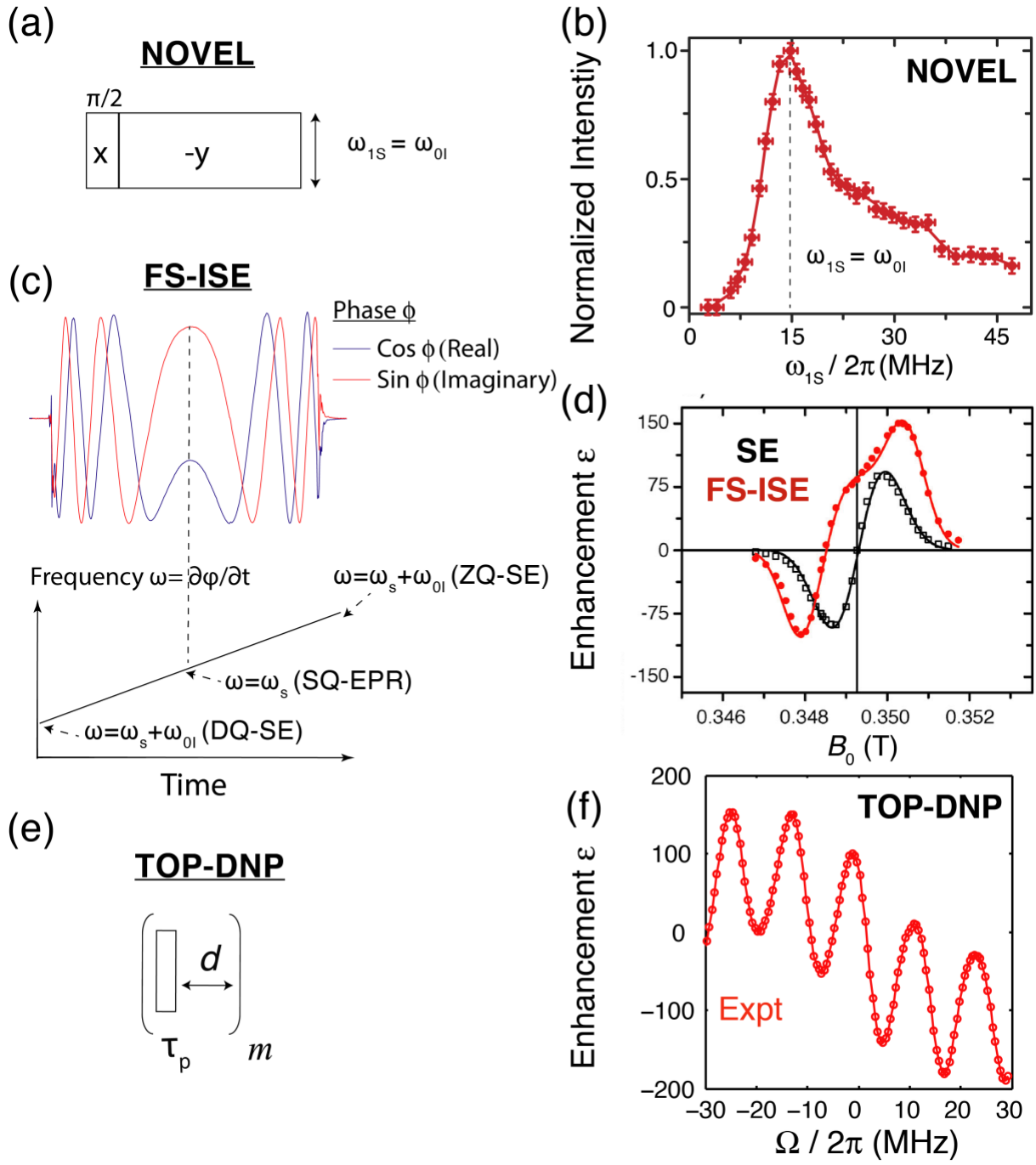

Figure 6: Schematic diagrams (a, c, and e) and the respective results (b, d, and f) of NOVEL (a and b), FS-ISE (c and d), and TOP-DNP (e and f). Figure b shows clearly that optimum enhancement is obtained when the NOVEL condition ($\boldsymbol{\omega_{1S} = \omega_{0I}}$) is

matched. For the FS-ISE sequence, the microwave frequency is swept across both the DQ- and ZQ-SE conditions via phase-modulated microwave pulses using an AWG. Figures adapted with permission from [52,71]. (source: Pulsed_DNP_2.ai)

3 Solvents, Radicals and Effects of Radical Additions

3.1 Solvents and Radicals

We have discussed the theoretical aspects of CW-DNP (Section 2.1) and pulsed DNP (Section 2.2). Despite theoretical predictions, the experimentally measured enhancement factors can vary significantly depending on the choice of radicals and the nature of solvent. The reasons that account for more efficient performance of some radicals than others are not completely understood. Nevertheless, there exists a *prima facie* relation between the EPR linewidth of the chosen radical and the most appropriate DNP mechanism. For instance, both the homogeneous, δ, and inhomogeneous, Δ, linewidth of the radical must be smaller than the nuclear Larmor frequency, i.e. $\delta, \Delta < |\omega_{0I}|$, for OE, SE, and pulsed DNP to work. On the other hand, both CE and TM conditions favor radicals that satisfy the relation $\delta < |\omega_{0I}| \leq \Delta$ for best performance.

We provide a summary of the standard type of radicals (Figure 7) used for different techniques here, assuming standard solvents such as DNP juice[78] (d_8-glycerol / D_2O / H_2O, 6:3:1 by volume) for water-soluble radicals and organic solvents such as d_6-DMSO / D_2O / H_2O mixture, tetrachloroethane (TCE) / methanol mixture,[79] and ortho-terphenyl (OTP) for other radicals with poor solubility in water. It is advantageous to perform DNP on samples comprised of an amorphous, glassy matrix to cryoprotect biological samples and to ensure even distribution of the polarizing agent throughout the matrix. Other factors such as solubility of radicals, solvent conditions, and interaction between radicals and target molecules also have to be considered when optimizing performance with minimal interference to the state of experiment. For instance, it was reported that the radical TOTAPOL has a tendency to bind to the surface of amyloids. While this may allow for more efficient polarization transfer at lower radical concentration, it also can perturb the structure of interest.[24]

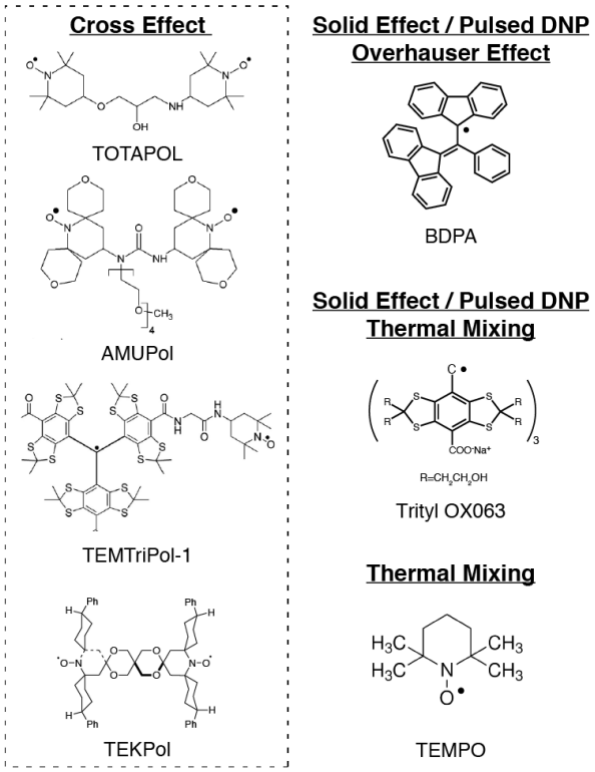

Figure 7: Structures of the commonly used standard radicals used for different DNP techniques. The EPR spectrum and the field profiles for TOTAPOL, trityl and SA-BDPA measured at 5 T can be found in Figure 2. (source: radicals.ai)

It is important to note that most of the solvents employed for DNP are perdeuterated so that higher polarization can be shared among the smaller number of nuclear spins. However, the average dipolar coupling, $d \propto \gamma^2/r^3$, becomes too small if the ^{1}H concentration is too dilute. Consequently, this will quench the dipolar-mediated spin diffusion that distributes the polarization among the bulk protons. Since the dipolar coupling also depends on the gyromagnetic ratios, most DNP techniques are usually directed at polarizing the ^{1}H nuclei directly rather than low-gamma nuclei such as ^{13}C.

To date, only BDPA and its water-soluble derivative, SA-BDPA, are shown to exhibit the OE in insulating solids. For thermal mixing, TEMPO, trityl, and their derivatives are found to be the most efficient. For MAS-DNP applications, radicals suited for the CE mechanism are usually employed in general cases. The standard radicals in this case are AMUPOL[80] and TOTAPOL[22] at low fields (9 – 14.1

T) and TEMTriPol-1 at high fields (18.8 T and above).[81] These three radicals fulfill the basic criteria of $\delta \leq |\omega_{0I}| \leq \Delta$ (refer to Figure 2c for the EPR spectrum of TOTAPOL), however, the reasons why these radicals perform well compared to other biradicals are not completely understood. There have been approaches to characterize spin parameters such as the electron-electron dipolar coupling, *D*, exchange interaction, *J*, *g* values and relative orientations of the two electrons by acquiring EPR spectra at different fields.[82,83] Furthermore, variants of the standard radicals have also been chemically modified. These modifications include substitution of subgroups, partial deuteration,[84] manipulating the length of linker,[23] and synthesis of triradicals/tetraradicals[85] to search for better CE polarizing agents. Most findings have reported that long T_{1e} relaxation times, strong dipolar couplings, and relative Euler angles between the *g*-tensors are crucial for efficient CE enhancement in general cases. Some of these features were exploited in designing rigid and bulky biradicals like the bTbK, PyPol, and TEKPOL series that are sufficiently rigid and large enough in size to limit molecular conformations, which led to longer relaxation times and hence higher enhancements.[84,86-88]

Both SE and pulsed DNP techniques are best implemented when the homogeneous linewidth of the radical(s) is smaller than the nuclear Larmor frequency $\delta \leq |\omega_{0I}|$. Some commonly used standard narrow-line radicals are trityl OX063, BDPA, Gd^{3+}-DOTA, and their derivatives. The trityl radical has a negligible hyperfine interaction and it is broadened mainly by *g*-anisotropy; whereas BDPA has larger hyperfine couplings (~ 5 MHz) but insignificant *g*-anisotropy. Gd^{3+}-DOTA is a high-spin (S = 7/2) metal ion complex[89] in which the central transition (CT) is primarily broadened by the zero-field splitting (ZFS), which scales inversely with the magnetic field. Hence, the CT linewidth is expected to get narrower as the static field increases. Another example of a high-spin metal ion complex utilized for DNP is Mn^{2+}-DOTA (S = 5/2), which has 6 EPR resonances (Figure 2c) in total for the CT. As a reference, the linewidths of trityl, BDPA, Gd^{3+}-DOTA (CT), and Mn^{2+}-DOTA (CT) are 42, 20, 29, and 25 MHz respectively at 5 T.[19,89,90] It is challenging to obtain high enhancement factors with high-spin metals because the Boltzmann

population spreads across all the m_S and m_I (if $I \neq 0$) energy states. Hence, we conclude that it is optimum to use trityl at low-fields (below 2.5 T) and BDPA/SA-BDPA for higher-field experiments.

Although most polarizing agents are synthesized to maximize DNP efficiency when added directly into a glass forming matrix, some polarizing agents are customized for specific applications, i.e. the polarizing agents can be incorporated either by direct or indirect binding to the sample of interest.[91-95] Another instance of this is the recent development of the trimodal polarizing agent, TotaFAM, which contains a nitroxide biradical for DNP, a peptide for cell targeting, and a fluorophore for fluorescent imaging.[96]

3.2 Quenching, Depolarization, and Electron Decoupling

Despite the important roles played by the radicals as the sources of polarization in DNP experiments, it is known that the presence of radicals can cause quenching and depolarization of NMR signals when microwave irradiation is turned off. We would like to clarify the differences between quenching and depolarization. Signal quenching is defined as a generic effect that occurs when radicals are added to the solvent, they cause large dipolar-induced shifts or line-broadening beyond detection in the nearby nuclei. This feature, known as paramagnetic relaxation enhancement (PRE), has been exploited in paramagnetic NMR spectroscopy to probe local environments surrounding the spin label.[97] Depolarization is attributed specifically to the situation where the signal decreases upon MAS spinning of the sample (Figure 8a) and occurs even when microwave irradiation is turned off. The depolarization effect is usually observed when cross effect radicals are utilized. The signal loss due to quenching is typically less than 20% for most common DNP radicals while depolarization can cause signal loss as much as ~50% in the case of TOTAPOL (Figure 8b).[30,98,99] We will focus our remaining discussion on the effect of depolarization as it is a more severe of the two.

It was realized that depolarization occurs upon MAS due to same rotor event, or anti-crossing of energy levels, that leads to the CE mechanism.[29] Although at first thought it might seem counterintuitive

that the same rotor event is responsible for both hyperpolarization or depolarization in a DNP experiment, the key factor that determines whether the anti-crossing is beneficial or detrimental is the polarization difference between the electrons in the quasi-periodic steady state. If the population difference of electrons is smaller than the nuclei polarization, it leads to depolarization during the CE rotor event. It was reported recently that the biradical TEMTriPol-1 does not exhibit depolarization effect because the population difference between the two electrons is not smaller than the nuclei polarization (Figure 8c).[100] There are multiple factors that govern the electronic population difference in the quasi steady state such as T_{1e}, T_{1n}, MAS frequency, dipolar couplings between the electrons, and the g-factors.[29] Another important consequence of the depolarization effect is the rationalization of the actual enhancement factor, i.e. the definition of enhancement factor ($\epsilon = I_{\mathrm{on}}/I_{\mathrm{off}}$) by comparing the signal intensities with the presence/absence of microwave irradiation has to be used with care. For instance, De Paëpe et al. have recorded $I_{\mathrm{on}}/I_{\mathrm{off}} \sim 677$ using AMUPOL at 55 K. The measured enhancement factor exceeded the theoretical maximum of $\gamma_e/\gamma_{1H} \sim 658$ because the effect of depolarization was not taken into account.[101]

Apart from the loss of polarization due to the quenching or depolarization, the presence of radical also shortens the lifetime of the spin coherences, i.e. it produces a line-broadening effect or shorter T_2. Nevertheless, recently Saliba et. al. have demonstrated experimentally that by sweeping the microwave frequency across the EPR spectrum during NMR detection, a reduction in linewidth by ~ 11 % can be achieved at MAS frequency of 4 kHz and static field of ~ 7 T.[57] The frequency sweep was performed using a home-built frequency-agile gyroton, which is capable of sweeping up to 250 MHz within a period of a few µs.

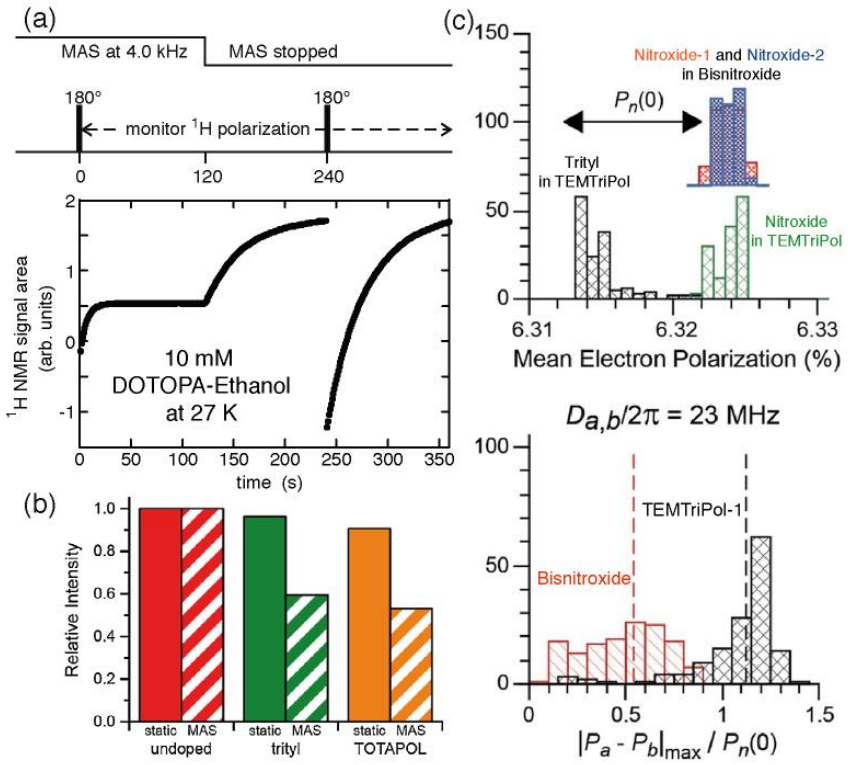

Figure 8: Experimental evidence of the effect of depolarization upon MAS in a sample doped with cross-effect radical (a) DOTOPA-Ethanol at 27 K and (b) trityl and TOTAPOL at 80 K. Signal loss of ~ 70 % is found in (a) DOTOPA-Ethanol and about 40-50 % for (b) 20 mM trityl and 10 mM TOTAPOL. Besides depolarization, signal quenching of about 5-10 % was recorded for the samples in (b) in the static case. Figure (c) shows the histograms of 144 powder orientations showing the mean electron polarization for the two electrons in a biradical for TEMTriPol-1 and a bis-nitroxide (top), and the electronic polarization difference scaled with the nuclei polarization (bottom). The vertical dashed lines indicate the value of the depolarization factor, which implies depolarization if it is less than 1. Figures adapted with permission from[30,38,100]. (source: Depol_eDec.ai)

4 Numerical Simulations and Spin Diffusion

4.1 Introduction

Despite the fact that DNP has been studied and developed extensively since its first demonstration in the 1950s, the underlying factors and optimum conditions required to yield efficient DNP transfer are not fully understood yet. For instance, the choice of solvent, type of radical, degree of deuteration, temperature, and even the protocol to freeze the sample could all affect the measurement of the

enhancement factor.[102] Additionally, we have discussed in the CE section that the moieties and the details of spin interactions are crucial but lack full theoretical analysis. It is clear that maximizing DNP enhancements is a multifaceted issue. Numerical simulation and theoretical modeling can provide useful insight and enable DNP mechanisms to be studied at reduced complexity to achieve enhancements closer to the theoretical maximum of ~658.

As mentioned in the introduction (Section 1), the DNP process involves multistage processes to transfer polarization from an unpaired electron to the target molecule: (1) from an unpaired electron to the nearby nuclei coupled directly via hyperfine interaction,[103] (2) from the nearby nuclei to the bulk nuclei, and (3) among the bulk nuclei via spin diffusion. Alternatively, radicals can polarize the bulk nuclei directly without a relayed transfer via nearby nuclei (Figure 9a). The first stage is essentially the main process where basic DNP mechanisms like CE and SE take place between an electron and a few nuclei, while the second and third stages are governed by the spin-diffusion mechanism in a large spin system. We will first discuss the architecture and theoretical framework in a typical numerical simulation package for the first stage of DNP. Then, we will describe different aspects and spin-diffusion models for the last two stages. Besides DNP simulations, EPR simulation programs are also an important tool to characterize polarizing agents and can provide essential spin parameters for DNP simulation. There are currently two EPR simulation programs: *EasySpin*[104] and *Spinach*[105], both of which are available as simulation packages in MATLAB.

4.2 Radical-Nuclei Polarization Transfer

The first stage of the DNP process, in the case of a small and isolated spin system, can usually be simulated reliably using a full quantum-mechanical description in numerical simulation packages like Spinach[105] and SPINEVOLUTION[106]. The former is free and an open source package in MATLAB while the latter is a standalone commercial software. The general features of the simulated field profiles are usually comparable to the experimental results, and qualitative arguments can be made on the performance of the DNP process. However, the simulated enhancement factors do not necessarily

resemble the observed value because factors like spin diffusion and the number of protons surrounding each radical are beyond the capability of the full quantum-mechanical calculations. Nevertheless, we will discuss briefly the main aspects and differences of the DNP simulations from the conventional NMR or EPR simulations.

One of the major considerations in the DNP simulation is the long time scale of the DNP sequence (seconds to minutes) compared to the inverse time scale of the electron-nuclear coupling (several MHz). This results in several issues that have to be considered. Firstly, the relaxation time scales of both the electron and nuclei are sufficiently short to be significant during DNP and have to be incorporated into the simulation. Secondly, the time step of each propagator for a time-dependent Hamiltonian has to be small enough to ensure the convergence of results.

Although there are many ways of treating the relaxation effects in the simulation, not all are applicable because relaxation is a non-coherent effect and incompatible with the mathematical description in a normal Hilbert space. Hence, an extended Hilbert space such as Liouville space is required to solve the master equation given as

$$\frac{d\hat{\sigma}(t)}{dt} = -i\hat{\hat{\mathcal{L}}}\hat{\sigma}(t) = -i\left[\hat{\mathcal{H}}, \hat{\sigma}(t)\right] - \hat{\hat{\Gamma}}\left\{\hat{\sigma}(t) - \hat{\sigma}_{\mathrm{eq}}\right\}, \tag{30}$$

where $\hat{\hat{\mathcal{L}}}$ is the Liouvillian, $\hat{\mathcal{H}}$ is the Hamiltonian that describes the coherent evolution, $\hat{\hat{\Gamma}}$ is the relaxation superoperator, while $\hat{\sigma}(t)$ and $\hat{\sigma}_{\mathrm{eq}}$ are the instantaneous and equilibrium density operators, respectively. The Liouville space is the cartesian product of two Hilbert spaces and it is spanned by a complete set of 2^{2N} basis operators, for an N spin-½ system. For instance, the Liouvillian, $\hat{\hat{\mathcal{L}}}$, defined for a two spin-system is described by a 16x16 matrix, compared to only 4x4 in Hilbert space. Thus, this makes DNP simulations more computationally expensive and also restricted to small spin systems ($\leq$ 6 spins) due to limited memory. In general DNP simulations, most relaxation models rely on the empirical T_1 and T_2 values measured experimentally. One of the simplest relaxation models is the random fluctuating fields or

local fields,[107] which has been adopted by Thurber et al.[14] and Hovav et al.[26,46] in their respective DNP simulations. The latter approach has been incorporated as the 'Weizmann' theory in *Spinach*, while other approaches include the Linbladian[108,109] and 'Nottingham'[110] DNP relaxation theory. The other complication in DNP simulations is that the master equation (Equation 30) is an inhomogeneous linear differential equation, i.e. the density operator $\hat{\sigma}(t)$ relaxes to a non-zero value of $\hat{\sigma}_{\mathrm{eq}}$ after a long time t. Two approaches were suggested by Levante et al.[111] and Levitt et al.[112] to transform the inhomogeneous master equation to become homogenous. The two approaches are equivalent in the case of a high-temperature approximation, i.e. $\hbar\omega_0/k_{\mathrm{B}}T \ll 1$.

The development of numerical packages for DNP simulations has been significant in the past few years and it is still an ongoing progress. Currently available simulation programs are able to simulate pulsed-DNP sequences as well as the CE and SE. The OE can be simulated, but only with preset values of cross-relaxation rates.[38] Additionally, it is still challenging to simulate the TM effect using full quantum-mechanical simulation due to limited computational power or effective algorithms to treat a large spin system accurately, where spin diffusion and cross relaxation are important. Nevertheless, Figure 9 shows some of the simulated DNP field profiles using the custom-built simulation programs developed in our lab.

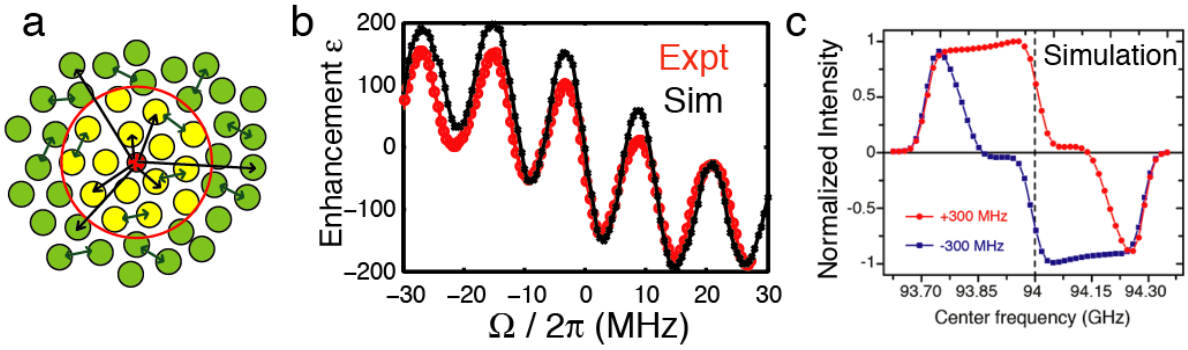

Figure 9: (a) The illustration of the model for spin diffusion barrier. The polarization can be transferred from the radical (red) to the bulk nuclei (green) directly, or via the nearby nuclei (yellow). Simulated field profiles of (b)TOP-DNP and (c) FS-ISE using custom-built simulation packages in Griffin's lab. Figures adapted with permission from [103,113].

4.3 Nuclei-Nuclei Polarization Transfer (Spin Diffusion)

After the nearby nuclei become polarized by an adjacent radical, the polarization might not contribute directly to the observable signal because its precession frequency might be shifted away from the Larmor frequency due to the hyperfine interaction. The large difference in precession frequencies between nearby and bulk nuclei can hinder the polarization distribution among the nuclei spin bath via spin diffusion.[114,115] In addition, these nuclei might experience shorter relaxation times, $T_{1n,}$ due to the paramagnetic effect and result in lower polarization for the bulk nuclei. Thus, the nearby nuclei whose polarization can't be transferred out to the bulk nuclei are considered to be within the "spin diffusion barrier" (Figure 9).[116-118] The size of the spin diffusion barrier was experimentally suggested to be ~5 Å for ytterbium-doped yttrium-ethyl-sulfate crystal $Y(C_2H_5SO_4)_3 \bullet 9H_2O:Yb$.[116]

The second step in the DNP polarization transfer pathway refers to the polarization transfer from the distant nearby nuclei, i.e. those at the edge of the barrier, to the bulk nuclei. Following that, the last step involves the polarization distribution among the bulk nuclei via the normal spin diffusion process. We would like to stress that the normal spin diffusion process here refers to the coherent mechanism that depends only on the dipolar interaction, as opposed to the stochastic processes like cross-relaxation or NOE (Nuclear Overhauser Effect). As mentioned earlier, simulating spin diffusion on a large spin system using full quantum mechanical calculation is computationally infeasible, since the dimension of matrices grow exponentially with respect to the number of spins involved. This issue can be circumvented by making sensible approximations in the numerical calculations, for instance, higher order spin coherences were shown to have limited influences and can be neglected in a restricted state space.[119,120] Alternatively, classical approaches like rate equations,[103] kinetic Monte Carlo algorithms,[121] or modified Bloch equations[122] can be used to model spin diffusion.

5 Instrumentation

Since the introduction of high-frequency microwave sources or gyroton for DNP at 140 GHz / 5 T at MIT by Griffin et al., along with the discovery of other DNP mechanisms, high-field DNP has now become a routinely applicable and preferred technique in solid-state NMR experiments.[123,124] Hence, we will present a comprehensive review on the features, operating principles, and limitations of the various microwave sources (Section 5.1). Following that, low-loss waveguide transmission lines (Section **Error! Reference source not found.**) and quasi-optical components that direct the microwave wave from the source to the DNP-MAS probe (Section 5.2) are crucial for high DNP enhancement as the waveguide transmission lines are typically ~ 60 – 70 % efficient and typical microwave absorption in the sample is less than 10 % due to the complex housing of the sample inside the MAS rotor (Section 5.3.4). Besides that, the incorporation of the cryogenic setup (Section 5.3) to achieve efficient DNP enhancements with low-temperature MAS will be discussed.

5.1 Microwave Sources

The frequency of a microwave source for DNP is about $\gamma_e/\gamma_{1H} \sim 658$ times higher than the ^{1}H Larmor frequency assuming a free electron g_e-factor of 2.002, i.e. 263 / 395 / 527 GHz for magnetic fields at 9 / 14 / 18.8 T, respectively. The important criteria involved in choosing a suitable microwave source for DNP-NMR experiment is the output power, capability to pulse or manipulate the phases, cost of operation, and the stability in maintaining the frequency and power over a long period of time.

An overview of the current state of average output power of various types of microwave sources as a function of frequency can be seen in Figure 10.[125-131] In particular, current research interests are in the microwave range of 140 – 700 GHz for corresponding NMR magnets ranging from 5 – 25 T. Two different technologies are available for microwave generation in this frequency range, solid-state transistor-based devices and vacuum electronic devices (VEDs). Although solid state devices are available up to frequencies of 1 THz (Figure 10), the average powers are below 100 mW; The VEDs can generate average power of over 100 W up to 700 GHz. However, solid-state devices are less expensive and their ease of integration into electronic systems e.g. enabling pulse gating, phase modulation,

quadrature detection, etc., make them useful for pulsed DNP / EPR experiments. In contrast, while VEDs, including Backward Wave Oscillators (BWOs), Extended Interaction Klystrons (EIK) and gyrotrons, offer more power at higher frequency, they are more expensive, less compact and not as flexible.

Apart from the maximum output power, the stability of the power and frequency of the microwave sources for DNP-NMR applications should be stable, i.e. less than variation of ±0.5% in power and ±2 MHz in frequency over week of operation. Moreover, it is also preferable to have 1-2 GHz of frequency bandwidth to optimize the DNP matching conditions for different radicals. Another practical considerations in choosing a suitable microwave source for DNP applications is the cost of the device and the operating lifetime with minimum maintenance. We will further elaborate further on the solid state devices (Section 5.1.1) and VEDs (Section 5.1.2), which fulfill these criteria for DNP applications, in the next sections.

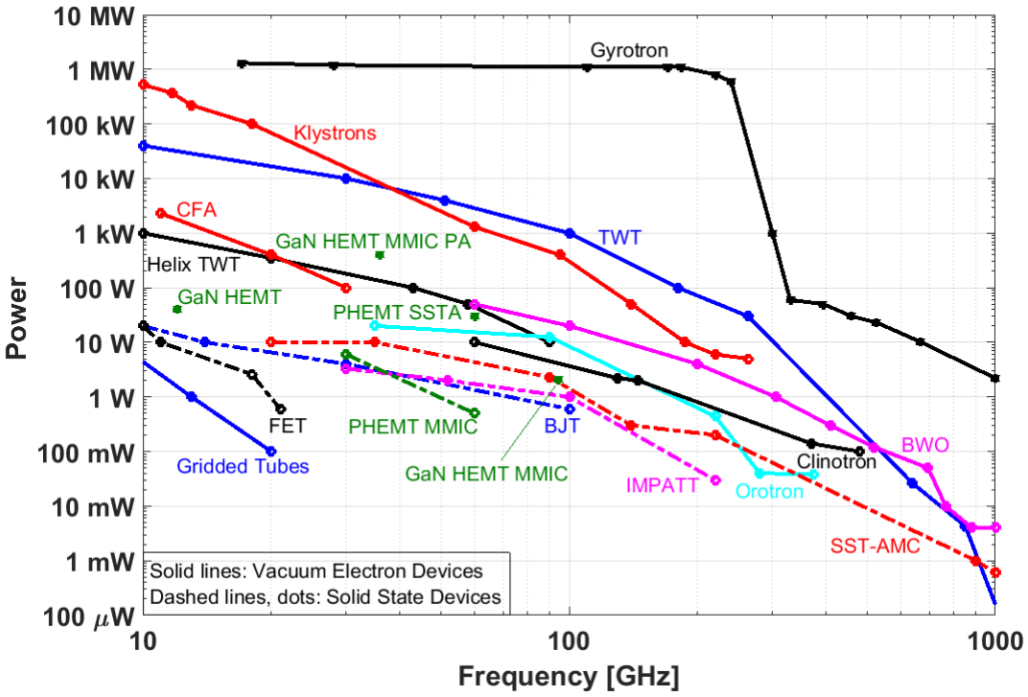

Figure 10: Plot of the average power output against frequency for various microwave sources, divided in two main categories: solid-state transistor based and vacuum electron devices (VEDs). TWT: travelling wave tube, CFA: cross field amplifier, BWO:

backward wave oscillator, GaN HEMPT MMIC PA: gallium nitride high electron mobility transistor monolithic microwave integrated circuit power amplifier, PHEMT SSTA: pseudomorphic high electron mobility transistor solid state transistor amplifier, SST-AMC: solid state transistor amplifier multiplier chain, IMPATT: impact ionization avalanche transit-time diode, BJT: bipolar junction transistor, and, FET: field effect transistor. Data are collected from [125-131].

5.1.1 Solid-State Devices

Solid-state microwave sources using diode-based frequency multipliers and amplifiers are advancing towards into the sub-millimeter and THz region. Significant progress has been made up to Ka-band (26 – 40 GHz) in terms of output power due to demand driven by commercial applications.[129] The TriQuint Semiconductor (now Qorvo, Inc.) company have microwave sources capable of generating power up to 400 W in Ka-band by efficiently combining GaN based solid-state power amplifiers (SSPAs). Despite this, generating higher power into sub-millimeter and THz region is still technologically challenging. Power amplifiers-multipliers are typically used in cascade to reach higher power at higher frequencies. Due to the reduced circuit dimensions at higher frequencies, the output power is generally limited because of enormous thermal load and heat dissipation in small areas. Also, very high junction temperature in transistor assemblies is another critical issue. For high field DNP-NMR applications at frequencies above 140 GHz the available power is very limited. Recently, VDI Inc. has produced peak power of 600 mW at 188 GHz using a varactor doubler[130] and 120 mW at 250 GHz using Schottky diode based amplifier-multiplier chain assembly.[128] It has also reported 6 microwatts at 2.6 THz. Many DNP NMR and EPR experiments up to 9.4 T have been done using solid-state sources[132-135] at these power levels. Their ease of integration with NMR, compactness, low cost, and simplicity to use over VEDs still make them a preferred option for DNP experiments at low fields. For instance, one of the key advantages of solid-state sources is that they can be integrated with an AWG to generate arbitrary shaped pulses to perform pulsed DNP experiments. Additionally, they can be used in conjunction with improved microwave resonator (Section 5.2.1) and/or at low temperature (Section 5.3) to maximize the DNP enhancements. Although the solid-state based microwave sources have limited power at high frequencies, the output microwave pulses

can be fed and amplified to kW pulses via the gyro-amplifier (Section 5.1.2.2.2), a VED, to perform pulsed DNP experiments.

5.1.2 Vacuum Electronic Devices

Vacuum electronic devices (VEDs) generate coherent microwave radiation via a resonant interaction between an electron beam and an electromagnetic wave. Since these are currently the most effective devices for solid-state DNP-NMR, we will discuss them in some detail; for a more complete treatment we refer the reader to relevant textbooks[136-138] and review articles.[125,139] The general features of VEDs are discussed here. The electron beam is generated by applying a high DC voltage between the cathode and anode of an electron gun. This electron beam is further accelerated through an electron tube till it reaches the resonant interaction circuit/cavity. Inside the cavity, the electron beam exchange energy with the electromagnetic wave by one of several possible interaction mechanisms (depending on the type of device). All of these interactions depend on some level of velocity synchronism between the beam and the wave; we will discuss the particular conditions for a few devices that have been used for DNP. Under the right conditions, the energy exchange results in a net transfer of energy from the beam to the wave, acting either as a microwave amplifier or source (oscillator). After the interaction cavity, the microwaves exit the VED through an output window whereas the electron beam proceeds to a collector. VEDs are primarily classified in two ways, slow-wave devices or fast-wave devices, based on the nature of the electron beam, the cavity mode, or the mechanism for their interaction. Before we discuss specific devices, we will establish (in the context of DNP) a general distinction between the slow- and fast-wave devices. Depending on the magnitude of the phase velocity ($v_{ph} = \omega/k_z$) of the electromagnetic waves compared to the speed of light c, a slow-wave device phase velocity $v_{ph} < c$ while a fast-wave device fulfills $v_{ph} > c$.

5.1.2.1 Slow-Wave Devices

Slow-wave devices include traveling-wave tubes (TWTs), backward wave oscillators (BWOs), klystrons, magnetrons, clinotrons, orotrons, and crossed-field amplifiers. All slow wave devices rely on a common concept of synchronism between the axial velocity of an electron beam with the longitudinal component of the electric field supported by a periodic radio-frequency structure specifically designed to slow down the wave. The slowed down wave's electric field induces longitudinal modulation in the electron phase velocities due to the periodicity of the structure resulting in current modulation. This leads to synchronism between the modulated beam and the periodic electric field resulting in generation or amplification of electric field. Due to their higher output powers at higher frequencies slow wave devices are preferred sources for DNP-NMR. In particular, a 10 W klystron developed by Varian Inc. operating at 40 GHz was the microwave source for the early solid-state DNP-NMR experiments of Wind and colleagues[140] . Schaefer and colleagues[141] also used a klystron as microwave source.

In recent years, klystrons have gained significant attention as microwave sources for DNP-NMR, particularly in the form of extended-interaction oscillator (EIO) or its amplifier version known as extended interaction klystron (EIK).[85,142,143]An EIK is a linear electron beam device that combines the high power capability of traditional klystrons with the large bandwidth of a TWT at higher frequencies. This is achieved by the introduction of cavities with multiple coupled gaps. The working principle of an EIK is shown in Figure 11a along with a photograph of a commercially available 220 GHz EIO in Figure 11b.

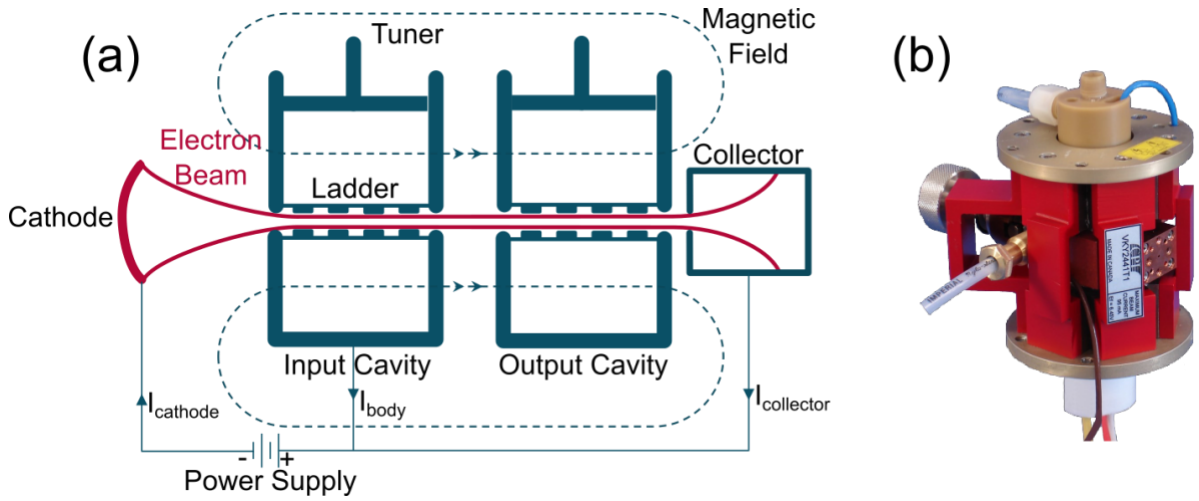

Figure 11: (a) Schematic of a typical EIK showing different components. (b) Photograph of a 170-220 GHz 10 Watt CW EIO from the company Communication and Power Industries Inc.[144] (Source: eik.svg)

The electron beam emitted by the cathode accelerates through a beam tunnel in the center of a series of cavities. For an EIK these cavities are divided in three sections, input and output cavities and an intermediate gain section. The RF structure is excited through the input cavities by an external driver source. The input section induces the current modulation in the beam. Additional cavities in between the input and output cavities, called the intermediate gain cavities contributes to high impedance which support resonant energy exchange between the beam and the electric field. An EIK can have multiple cavities whereas an EIO is a single cavity device. Since the interaction circuits in EIKs and EIOs do not have to be as long as those of other devices, one can supply the external magnetic field with a small and relatively inexpensive permanent magnet. Communications & Power Industries (CPI) Canada is a leading manufacturer of EIK's and EIO's for DNP applications.[144,145] Currently their EIO can produce 5 W CW microwave power at 263 GHz with 2 GHz bandwidth using mechanical cavity tuning. The photograph shown in Figure 11b is a 220 GHz, 10W CW EIO with 4 GHz mechanical tunability. EIK's and EIO's are successfully used for solid state DNP applications,[85,142,143] up to 263 GHz. DNP enhancement factor of over 100 was achieved using a 264 GHz 1.5 W EIO at cryogenic temperature of 25 K.[85] Another experiment achieved similar enhancement of over 100 using a 187 GHz 3 W EIK.[142] A 1.03 THz TWT

power amplifier was recently demonstrated[127] by Northrop Grumman Corporation achieving 29 mW peak power and 2 GHz with 3dB bandwidth in short pulses of 30 μs.

Slow wave devices offer several advantages for DNP-NMR applications with respect to the solid-state sources. In addition to significantly higher power and tunability they are relatively compact and can be employed with minimum lab space. The lifetime of such state of the art EIKs is however limited to 20,000 hours, which raises issues about their cost effectiveness. They also suffer from fabrication challenges at higher frequencies. Due to the interaction structure geometry to slow down the RF wave the electromagnetic fields can be quite high near the metallic wall of the structure. The electron beam must propagate in close proximity of the wall for efficient interaction. Due to the small dimensions of the interaction structure and beam transmission space, smaller than the wavelength, the high heat load generated by the transmitting beam degrades the structure relatively quickly. This limits their operating lifetimes. Furthermore, extending frequencies into sub-millimeter and THz region is difficult because miniaturization of structures makes the fabrication extremely challenging. Several efforts have been made, currently limited to research purpose only, to increase the beam transmission space by employing overmoded and oversized structures such as overmoded TWTs and photonic-bandgap-based structures.[146,147]

5.1.2.2 Fast-Wave Devices

The other broad category of device, fast-wave devices, includes gyrotrons and free-electron lasers (FELs). In such devices the phase velocity of the electromagnetic wave is higher than the speed of light $(v_{ph} > c)$. Coherent electromagnetic radiation is generated or amplified by the stimulated emission of bremsstrahlung from a relativistic electron beam. In these devices, the electrons in the beam oscillate transverse to the direction of beam propagation in an externally applied magnetic field. The oscillation frequency of the beam Ω is related to the generated microwave frequency $\omega_{\mu w}$ by

$$\omega_{\mu w} - k_z v_z \approx s\Omega, \tag{31}$$

where k_z is the axial wavenumber of the electromagnetic (EM) wave at resonance, v_z is the axial drift velocity of the electron beam, and s is an integer representing the harmonic of the interaction. The beam oscillation allows the EM wave's phase velocity $\omega_{\mu w}/k_z$ to be greater than the speed of light (whereas if $s = 0$ the condition becomes that for Cerenkov radiation $\omega_{\mu w}/k_z = v_z$, and v_z is strictly less than c).

Since fast waves can propagate in an open waveguide, they do not require the same fragile slow-wave structures and reduced device dimensions to generate high power microwaves at higher frequencies. This allows the fast wave device to operate at more beam current situated at regions of higher electric field in the cavity for efficient beam-wave coupling, generating higher power. It was for these reasons that a fast-wave device, particularly the gyrotron, was first considered for use in DNP-NMR at high fields.[124] Gyrotron technology had matured significantly over the past two decades due to their use for heating the plasma in nuclear fusion tokamak experiments,[148] at megawatt power levels operating at frequencies up to 300 GHz. For DNP-NMR applications where the power requirements are up to 50 watts they have undergone many refinements including their capability to operate for continuously longer durations, weeks at a time, with stable power and frequency.

Since their first demonstration to be a reliable microwave source for DNP-NMR[124], gyrotrons have become the most widespread and considered the best microwave source for DNP because they have been the only source to provide sufficient power for DNP at high fields. One major advantage of a gyrotron in comparison to a slow wave device is its operating lifetime > 100,000 hours. The 140 GHz gyrotron built and designed at MIT[124] is still in operation, demonstrating the operating lifetime in excess of 100,000 hours. Today, dozens of gyrotrons operating between 140 and 593 GHz are used for DNP-NMR, including commercially available gyrotrons at 263,[149] 395, 527, and 593 GHz. Despite their many advantages e.g. higher power at higher frequencies and continuous stable operation for longer periods, they suffer from a few disadvantages, namely the cost and larger space for installation. The cost is mainly

driven by the requirement of higher magnetic fields generated by large superconducting magnets and auxiliary components for operating the gyrotron, such as liquid cryogens, high voltage power supply, water cooling systems etc. This makes the entire gyrotron system large requiring more laboratory space for installing the device. For a complete introduction and a synopsis of the history of gyrotrons in plasma physics research, the reader is referred to relevant textbooks[148,150,151] and review articles.[152,153]

5.1.2.2.1 Principles of Operation and Design of Gyrotons

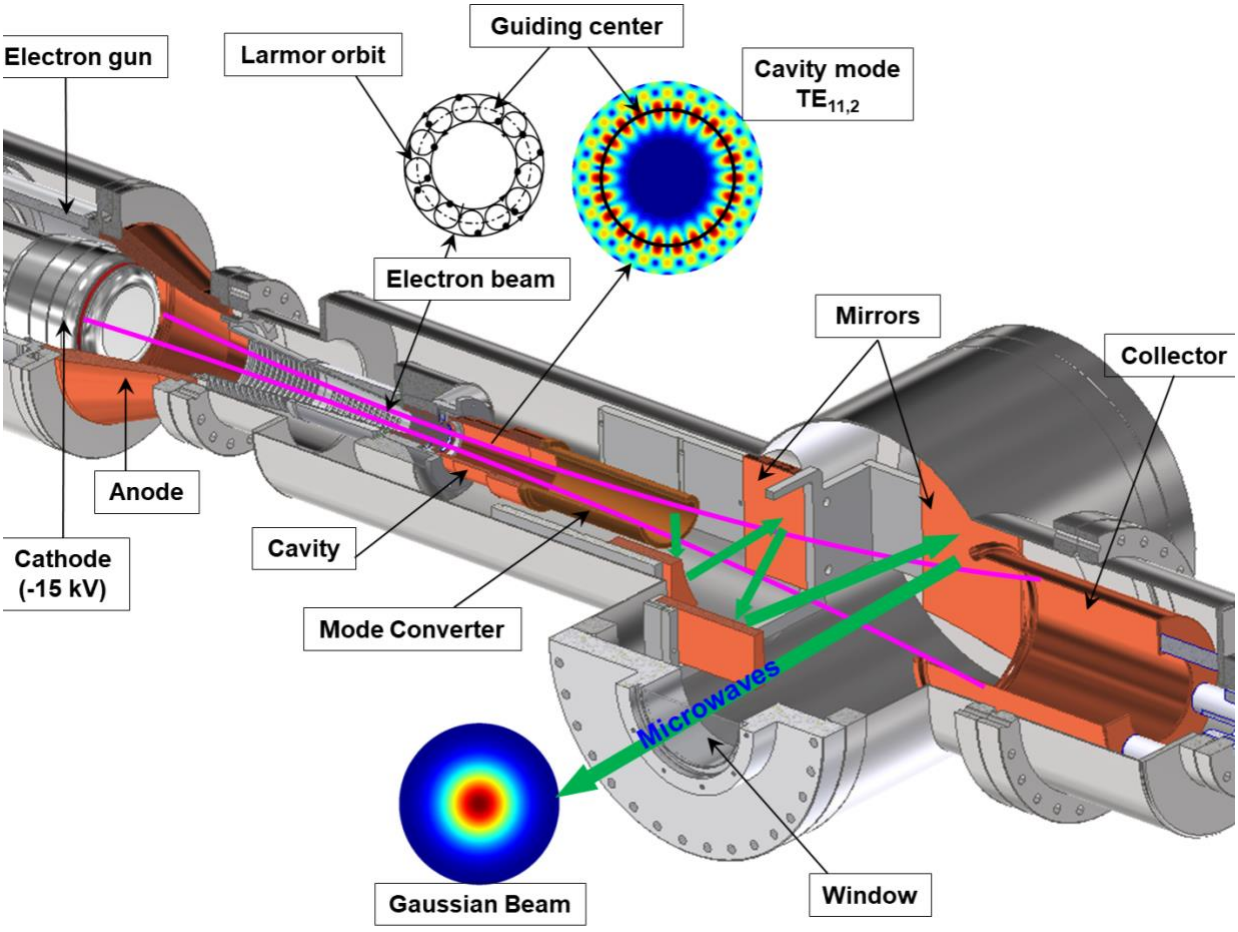

Figure 12: A CAD picture showing typical components/assembly of a gyrotron tube.The electron gun (annular ring shown in red on the left side) produces an electron beam (purple lines) which is accelerated and adiabatically compressed by the external magnetic field until arriving at the interaction cavity. The cyclotron mode of the beam interacts with the cavity mode $TE_{m,p}$ (a $TE_{11,2}$ mode is shown) of the electromagnetic wave, ultimately generating (shown in green) microwave radiation. The microwave radiation is initially in the cavity mode (in the form of $TE_{m,n}$ mode), but a helical cut waveguide (mode converter) and a series of

mirrors converts the microwaves to a Gaussian-like beam for propagation in free space or a corrugated waveguide. After exiting the cavity, the energy of the "spent" electron beam is dissipated by an actively-cooled collector.

The main components (Figure 12) of a gyrotrons are an electron gun, a superconducting magnet, an open cavity waveguide located at the peak of the magnetic field, a quasi-optical mode converter with reflective mirrors, a microwave window, and a collector. Unlike in many of the slow-wave devices previously mentioned, the electrons generated by an electron gun must have an initial non-zero transverse velocity in order to oscillate in the applied magnetic field. This is typically achieved using a single anode magnetron injection gun (MIG) operating at 10-20 kV and 100-200 mA electron beam current. Electrons are thermionically emitted in the form of a hollow beam from the heated annular cathode and acquire initial axial and transverse velocity in the crossed electric and magnetic field due to the potential between the cathode (negative potential) and anode (ground potential). The electron beam is initially generated in the fringe field of the main magnet, and as it accelerates towards the cavity the beam experiences an increasing magnetic field. The electrons follow the magnetic field lines in a cyclotron motion. Their transverse velocity increases in exchange for their axial velocity as the electron beam is adiabatically compressed in the magnetic field due to conservation of electron orbital momentum. An optimal electron beam waist is achieved at the center of the interaction cavity for efficient interaction between the cavity mode and the electron beam.

In the cavity the electrons gyrate along the constant magnetic field lines in Larmor orbits (Figure 12) centered in a guiding center orbit. The transverse energy in the beam at the interaction region depends on the ratio of the transverse velocity, $v_\perp$, to the axial velocity, v_z of the beam, also known as pitch factor $\alpha = v_\perp / v_z$. The pitch factor can be fine-tuned with a secondary magnet called the gun coil magnet. The electron optic system is specifically designed to achieve the appropriate beam radius and thickness at the cavity and high pitch factor values, typically 1.6 – 2.0, while minimizing the spread of electron transverse velocity $\Delta v_\perp$. The cavity supports a transverse cylindrical electromagnetic mode TE_{mp} with frequency

$\omega_{\mu w}$ near cutoff. An example of the operating cavity mode $TE_{11,2}$ for a 527 GHz gyrotron cavity is presented in Figure 12 showing two radial and twenty-two azimuthal electric field variations. For net energy exchange from the electron beam to the TE_{mp} mode in the cavity two phenomenon must happen; 1) the beam-wave synchronism condition in Equation 31 must be satisfied, and, azimuthal electron bunching mechanism.

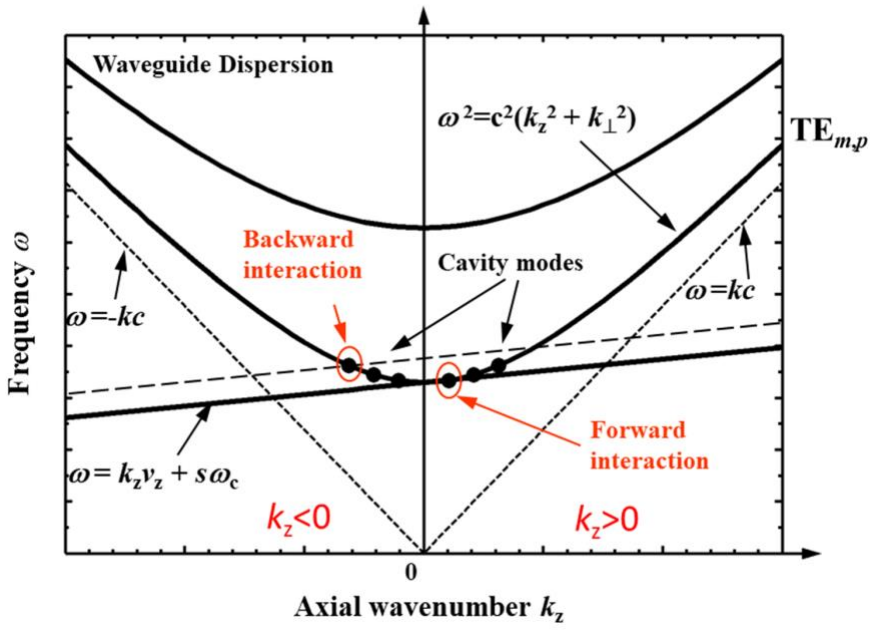

Figure 13: The beam-wave dispersion diagram showing the waveguide mode dispersion, a parabola, and the electron beam line, a straight line. The beam-wave synchronism can happen for two cases, forward and backward interaction.

Figure 13 shows the beam-wave synchronism plotted in in the form of cold waveguide dispersion relation, $\omega^2 - k_z^2c^2 - k_\perp^2c^2 = 0$, where $k_\perp$ and k_z are the transverse and axial wavenumbers of the TE_{mp} mode. The cyclotron frequency ω_c for the Doppler shifted resonance condition is,

$$\omega_c = \frac{eB_0}{m_0\gamma}, \tag{32}$$

where e is the electron charge, B_0 the main magnetic field, m_0 the electron rest mass, and $\gamma = (1 - v^2/c^2)^{-1/2} \approx 1 + eV_0/m_0c^2 = 1 + eV_0/511$ the relativistic correction factor. The solid line in the plot in Figure 13, represented as electron beam line, interacts with the cavity mode TE_{mp}, shown as a

parabola, in the forward interaction region. Typically, a gyrotron operates in the forward wave region. The dependence on B_0 determines the required magnetic field for a gyrotron to output a particular frequency. This gives the nonrelativistic electron cyclotron frequency to be $f = sf_c = s \times 27.9924\ \mathrm{GHz/T}$. A gyrotron operating in the fundamental mode ($s = 1$ in Equation 31) requires a magnetic field approximately equal to that of the NMR superconducting magnet. For frequencies above 300 GHz, the required magnetic field exceeds 10 T which require more expensive superconducting magnet systems. Therefore, it is preferable to operate the gyrotron in the higher harmonic interaction, $s = 2$. Operating at higher harmonics decreases the gyrotron efficiency, i.e. the power drops by a factor of s^2 in theory. Even with the reduced efficiency the achieved microwave power levels at higher cyclotron harmonic operation exceeds the requirements of any CW DNP experiment.

Within the cavity of a gyrotron, the electrons pass through the electromagnetic field of the cavity mode, and undergo acceleration or deceleration depending on the phase of the field. This is depicted in Figure 14 where the electron Larmor orbit is shown in different time frame $T = i\,2\pi/\omega$ as the electrons progress through the interaction cavity. When the electrons first enter the cavity, shown in frame 1, they are randomly distributed in the EM field around a Larmor orbit of radius $r_L = v_\perp/\omega_e$ following a common guiding center radius (beam radius r_e). As the electrons advances in the cavity, in the region where $v_\perp \cdot \mathbf{E} < 0 < 0$ or $\dot{\gamma} > 0$ (shown in green), electrons are accelerated and will gain energy. However, because the cyclotron frequency depends on the electron velocity (due to the γ term in Equation 32), accelerated electrons rotate slower with increased Larmor radius. The electrons in the deceleration region where $v_\perp \cdot \mathbf{E} > 0$ or $\dot{\gamma} < 0$ (shown in red), will lose their energy and rotate faster with decreased Larmor radius. After a few cycles, the electrons become azimuthally bunched in the phase of their cyclotron oscillation. This electron bunch will be located in the decelerating phase of the field and a net energy from the bunch will be transferred to the field.

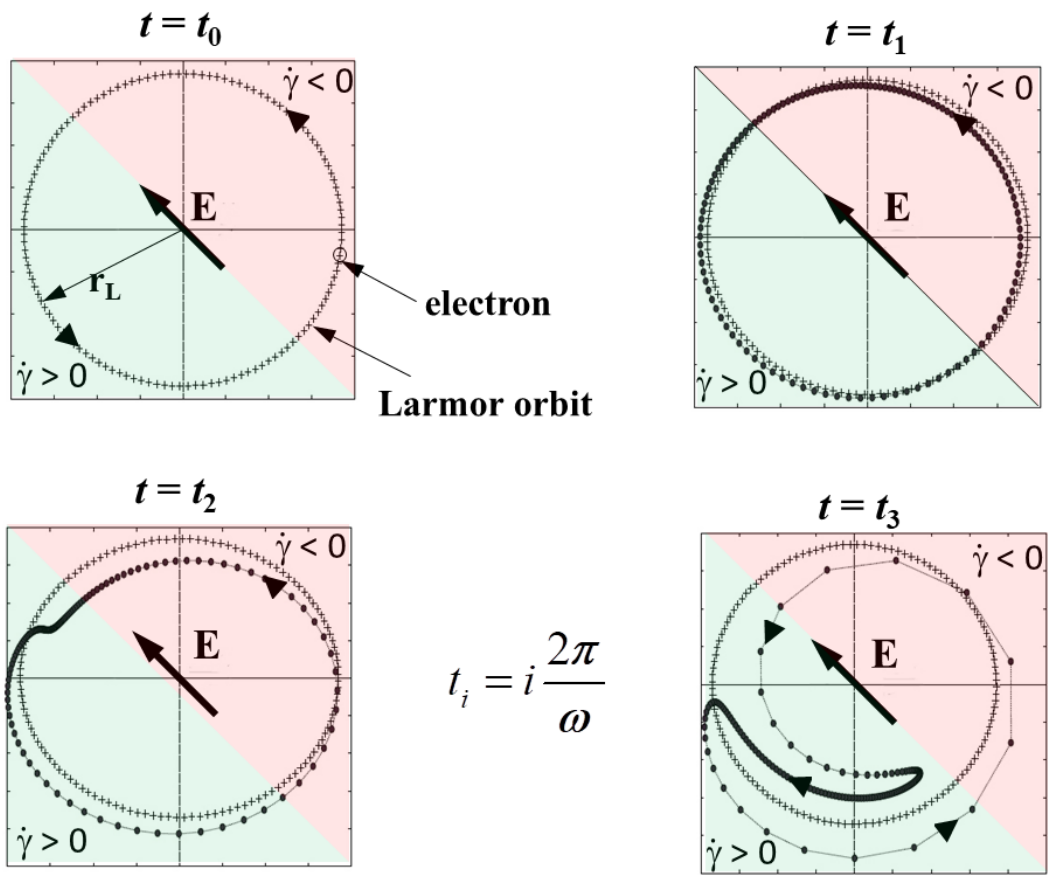

Figure 14: Azimuthal bunching of an electron beam interacting with a cavity electric field E in synchronism with the fundamental cyclotron harmonic (s = 1). Each frame corresponds to a multiple of microwave period at different axial locations in the interaction cavity. The red area $\dot{\gamma} < 0$ represents the decelerating region whereas green area $\dot{\gamma} > 0$ represents the accelerating region.

After the beam-wave (energy exchange) interaction, the generated microwave leaves the tube via a specially designed mode converter to convert a higher order circular waveguide TE mode into a field with more appropriate spatial distribution which is well suited for long distance propagation from the gyrotron exit into free space. The design of a mode converter is unique to individual gyrotron and depends on the operating TE mode of the cavity and the frequency of operation. Designing an efficient mode converter has been a topic of great interest for megawatt power level gyrotrons. A complete mode converter consists of a helically cut waveguide, called a Vlasov launcher,[154,155] followed by a series of quasi-parabolic or toroidal and plane mirrors. This mode converter unit transforms a TE mode into a Gaussian

beam, or a low loss waveguide mode, an HE_{11} mode of a corrugated waveguide, which is well suited for long distance propagation from the gyrotron exit to the DNP probe and ultimately to the NMR sample. On the other hand, the spent electron beam in the gyroton tube travels into low magnetic field of the superconducting magnet and deposits its remaining energy on to a collector (Figure 12).

Figure 15a shows a photograph of a 527 GHz gyrotron, whose electron gun operates at 10 – 15 kV and 200 mA beam current.[156] The electron beam passes through a beam tunnel of slotted rings of lossy ceramic to suppress unwanted microwave generation. The cavity (right in Figure 15a) is situated at the peak of the magnetic field at the center of the superconducting magnet. The magnet used in this experiment is a fully cryo-free magnet operating with a pulse tube cryo-cooler. The tube is operating in second cyclotron harmonic (s = 2) at 9.7 T magnetic field and $TE_{11,2}$ mode in the interaction cavity. The mode converter with a helical cut waveguide and mirrors are also shown in the CAD view. The microwaves are extracted using an internal 12 mm i.d. corrugated waveguide through a quartz window and coupling to an external 16 mm i.d. corrugated waveguide through a corrugated linear taper. The spent electron beam is collected on a water-cooled copper collector which is at ground potential. The water cooling lines for cavity and collector can be seen in the photograph. The entire tube is kept under ultra-high vacuum using two 20 L/s vac-ion pumps.

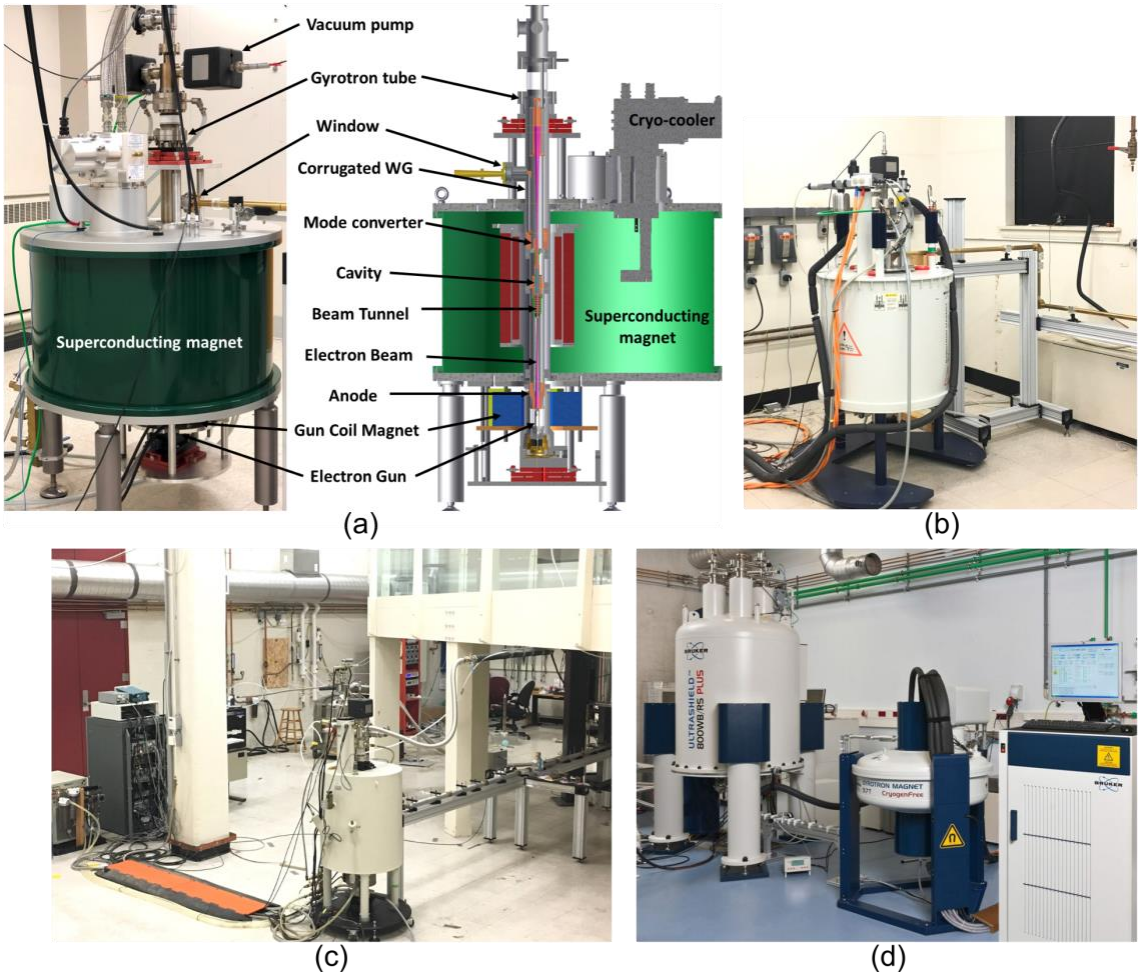

Figure 15: Photographs of a (a) 527 GHz gyrotron (left) and the CAD view of different components of a gyrotron in the superconducting magnet (b) 330 GHz gyrotron (second harmonic operation in $TE_{-4,3}$ operating cavity mode) in a 6 T magnet for a 500 MHz NMR spectrometer (c) 460 GHz / 700 MHz DNP-NMR system with the gyrotron control system (left) and auxiliary components and the 19 mm i.d. corrugated waveguide transmission line made of aluminum (d) a commercial 527 GHz/800 MHz DNP-NMR system. [157] (Fig_gyro)

5.1.2.2.2 State of the Art and Outlook

There have been significant research efforts worldwide in improving gyrotron technology for DNP. Here, we summarize several current DNP-related gyrotron research programs to provide an idea of the currently available technology and directions for the foreseeable future. MIT initiated the gyrotron development and have successfully built five gyrotrons at 140, 250, 330, 460 and 527 GHz.[156,158-162] Other than the conventional gyrotons, the MIT group's focus has been on developing frequency agile gyrotron capable

of frequency bandwidth of 1-2 GHz using high voltage or magnetic field tuning. This however produces another challenge of mode competition in the interaction cavity where electron beam can interact with nearby waveguide cavity modes. The gyrotron at 330 GHz and above are operating at second harmonic of electron cyclotron. The 250 GHz gyrotron developed for a 380 MHz NMR spectrometer produced 15 W operating CW at 10 kV and 85 mA of electron beam current.[159,160] The frequency bandwidth of 3 GHz was achieved using voltage and magnetic field tuning. Excellent power and frequency stability were also achieved while the tube was operating at CW mode for very long duration, months. This was accomplished by the PID feedback control voltage based with stable output power and frequency. The 330 GHz gyrotron (Figure 15b) was developed and integrated with the 500 MHz NMR spectrometer.[161,163] This gyrotron operated in the second cyclotron harmonic and TE_{-43} interaction cavity mode producing 18 W at 13 kV and 150 mA of beam current. The 460 GHz second harmonic gyrotron (Figure 15b) developed for a 700 MHz NMR spectrometer is capable of generating 16 W (Figure 16a) of microwave power in the $TE_{11,2}$ mode.[162,164] The output beam (Figure 16b) measured with a pyroelectric camera after the corrugated waveguide reveals a high Gaussian-like mode content of ~92%.

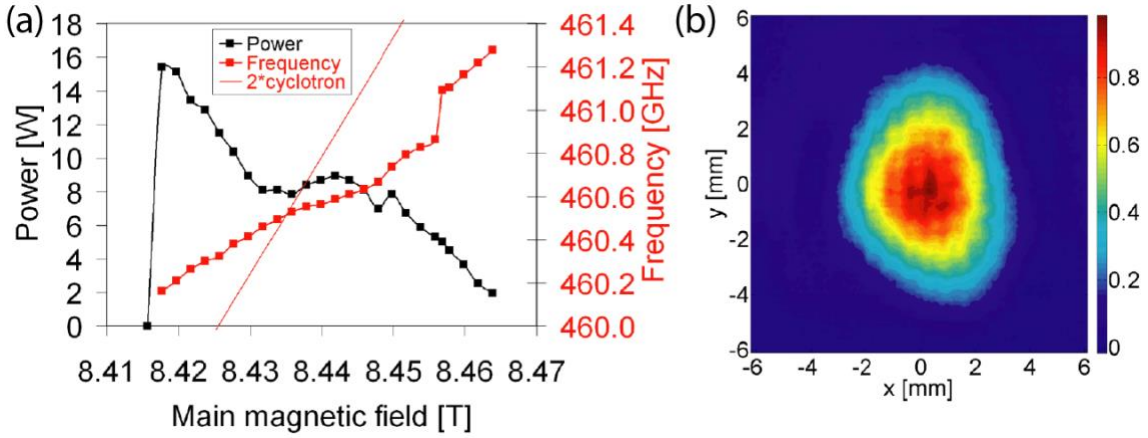

Figure 16: (a) Measured output power and frequency of the 460 GHz gyrotron with respect to the beam voltage showing a measured tuning range of ~ 1 GHz. (b) Output Gaussian beam profile generated by the 460 GHz gyrotron. The image is measured using a THz pyroelectric camera. (460gyro.ai)

Idehara and colleagues at Fukui University have developed various high frequency gyrotrons for DNP-NMR applications. They have built a 395 GHz gyrotron for a 600 MHz NMR spectrometer at Osaka University.[165] In the realm of ever higher frequencies, Idehara and colleagues have constructed a gyrotron to operate at 790 GHz in the second harmonic[166,167] and theoretically explored operation at 1.2 THz in the third harmonic.[168] They have experimentally demonstrated a 1.08 THz gyrotron operating in a pulsed mode using a 20 T SCM.[169] Frequency-tunable gyrotrons at many frequencies[159,161,162,170,171] have been developed as a way to satisfy DNP matching conditions for a variety of radicals and polarization mechanisms without a need to vary the field of an NMR magnet. Frequency-agile gyrotrons, in which the microwave frequency can be modulated over the course of an experiment by varying the accelerating voltage of the electron gun, represent one way to bring pulsed DNP to high fields. Idehara and coworkers have modulated the frequency output of a 460 GHz gyrotron by up to 50 MHz, observing an increase in overall DNP enhancement.[172] Barnes and coworkers have built and used a frequency-agile 198 GHz gyrotron with a >200 MHz bandwidth to switch from a DNP matching condition to an electron decoupling condition, demonstrating a corresponding reduction in homogeneous linewidths with decoupling.[57]

A 263.5 GHz gyrotron was developed at EPFL Lausanne for a 400 MHz NMR spectrometer[173] demonstrating over 100 W of output power. The MIT 527 GHz gyrotron magnet shown in Figure 15a is a copy of the magnet used for the successful EPFL 263.5 GHz gyrotron. Several research efforts are also ongoing at IAP in Russia, and in universities in China for developing 260 and 330 GHz gyrotrons respectively for DNP-NMR.[174-176] Commercially, CPII Inc. has built and installed gyrotrons at the frequencies 263, 395, 527 and 595 GHz in collaboration with the Bruker Corp. These gyrotrons are fully integrated with the NMR spectrometers and are in use by more than 35 research groups across the world. A photograph of their 527 GHz/800 MHz gyrotron-NMR spectrometer is shown in Figure 15d. A 260 GHz gyrotron has been built by the Gycom Co. of Russia and installed in Germany. [175]

While gyrotron oscillators (which we have referred to as gyrotrons) are the most common type of gyro-device for DNP, one can also develop fast-wave analogs of backward wave oscillators (BWOs), klystrons, and traveling wave tubes (TWTs). The existence of gyro-BWOs, gyro-TWTs, etc., is well known.[152]

As the ultra-high field magnet is expected to become available soon due to demand for applications in biological NMR and material science, there is also a call for more efficient DNP techniques at high fields. Although the pulsed DNP techniques are expected to have more robust performance over the CW-DNP techniques at high fields, the technique is not feasible unless high power (500 – 1000 W) microwave pulses are available. Gyro-amplifiers are the most promising sources for producing such high-power pulses. Recently, Temkin and coworkers have built gyro-TWTs for use in pulsed DNP-NMR. One device operates at 140 GHz and uses a confocal waveguide to suppress backward oscillations and undesired modes.[177] The gyrotron amplifier operates in a HE_{06} mode of a confocal waveguide circuit demonstrating a peak circuit gain of 35 dB, a bandwidth of 1.2 GHz while operating at 48 kV and 3 A of beam current producing 550 W peak power at 140 GHz. Another gyro-amplifier was developed at 250 GHz (Figure 17) using a novel electromagnetic circuit, a photonic-bandgap waveguide cavity. This amplifier produced pulses as short as 260 picoseconds with a device gain of 38 dB and an impressive instantaneous bandwidth of 8 GHz. The total operational bandwidth was observed to be 16 GHz by adjusting the magnetic field and voltage. The circuit gain of more than 55 dB was obtained at very moderate operating voltage of 23 kV and 700 mA of beam current.[178,179] These devices allow one to generate high-frequency microwave pulses of very short durations and waveforms at low power and amplify them to the power levels needed for pulsed EPR and DNP, as has been done at lower frequencies using solid-state and/or slow-wave amplifiers.

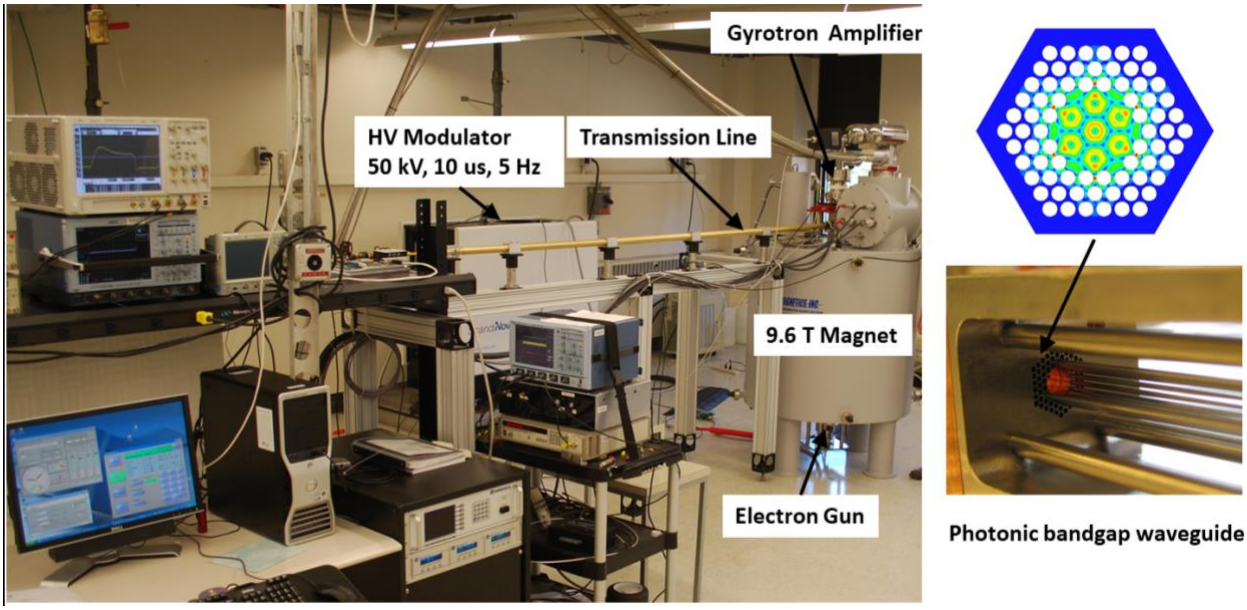

Figure 17: A 250 GHz gyro-amplifier system placed in a 9.2 T cryo-cooled magnet. Corrugated waveguides made of brass can be seen in the picture. Simulated electric field distribution of a TE_{03}-like mode in a photonic bandgap (PBG) waveguide made of metallic rods is shown in the upper right picture. White dots in the figure represent the metallic rods while the remaining space is vacuum. Electron beam passes through the hollow region in the waveguide. Bottom right picture shows the semi-assembled photo of the PBG waveguide showing the rods and empty space beam tunnel for electron beam.

5.1.3 Waveguide and Quasi-Optical Bridge

In order to avoid any field interference between the gyrotron and the NMR superconducting magnets, gyrotrons are kept at a safe distance from the NMR magnet. This means that efficient transmission of the microwaves from the gyrotron to the probe is vital to minimize power losses at the sample. Thus, the Gaussian beam created by the internal mode converter is transmitted through an overmoded corrugated waveguide whose radius is much larger than the wavelength of the incident microwave radiation. The high coupling efficiency of a Gaussian beam to the lowest order mode HE_{11} of a corrugated waveguide, over 98%, makes it convenient to couple into the corrugated waveguide. Extensive research has been published on high power overmoded corrugated waveguide in sub-millimeter wavelength region because of their use in megawatt level power transmission in fusion plasma experiment.[180-188]

A low-loss corrugated waveguide (Figure 18a) typically have a groove depth of $d \sim \lambda/4$, period $w_1 \sim \lambda/3$ and tooth width $w_2 \ll w_1/2$.[149,188,189] It becomes mechanically challenging to fabricate the waveguide due to shorter wavelengths at higher microwave frequencies. Thus, helically tapped grooves are preferred at higher frequencies. For instance, a photograph of a corrugated section of a 19 mm inner diameter waveguide machined with a tap of 0.318 mm groove is shown in Figure 18a.[190] Ohmic losses for a fundamental HE_{11} mode in such an overmoded corrugated waveguide are less than 0.1dB/m. The measured insertion loss in the 330 GHz waveguide was 0.0259 dB/m. An example of calculated ohmic loss in overmoded corrugated waveguide, of i.d. 19 mm with rectangular corrugations d = 0.227 mm and w_1 = 0.3175 mm, is shown in Figure 18b. At higher frequencies into the THz region, the attenuation is very small.

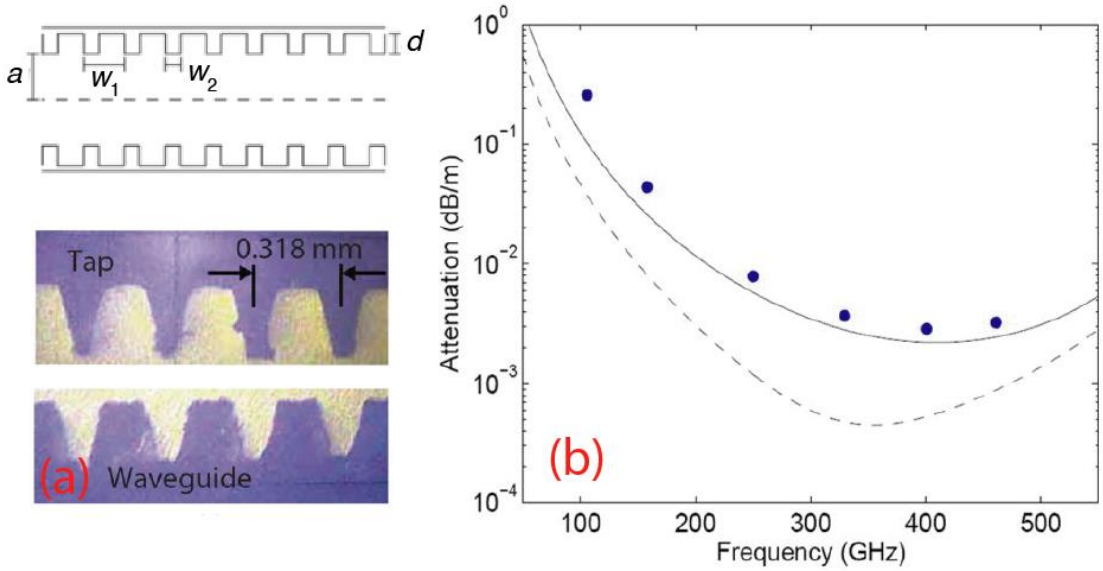

Figure 18: (Top) Schematic of a corrugated waveguide showing different parameters. (Bottom) Photograph of the cross-section of a 330 GHz waveguide and tap used to machine the corrugations. (b) Numerical simulations of ohmic loss in corrugated waveguide made of brass. Solid line: Analytical theory,[191] dashed line: Impedance approximation method, dot: HFSS numerical simulations. (waveguide.ai)

Changes in the direction of propagation of microwave are achieved by right angle bends known as miter bends. The overall transmission loss in the system is dominated by the power loss encountered at

these miter bends, as well as any misalignments in the waveguide components and imperfections in the Gaussian beam quality. With careful alignment overall microwave efficiency of over 70% can be achieved from the gyrotron window to the NMR sample inside the probe.[163]

Alternatively, quasi optical systems could be used for microwave transmission. They have the advantage that extremely low-loss transmission can be achieved over a broad range of frequencies. Furthermore, better control over the polarization of the microwave beam is possible by introducing a Martin-Puplett interferometer. This quasi optical system requires the use of a number of curved or flat mirrors over the microwave transmission length and the initial set up can be challenging. For general use the optics need to be in an enclosed system. Pike et al. have successfully employed a quasi-optical microwave transmission setup for DNP applications.[192] Han et al have fabricated a 200 GHz EPR-DNP spectrometer[134,193] with a combined system of quasi optical microwave bridge and corrugated waveguide for microwave transmission. Their measurements showed a 28% increase in DNP enhancement at 4 K by circularly polarizing the microwaves rather than utilizing linearly polarized microwaves. On the other hand, a single gyrotron can be configured to serve two different NMR spectrometers via a quasi-optical transmission system.[194]

5.2 DNP Probes

The first experimental setup solid-state DNP-NMR spectroscopy was demonstrated by Wind et al.[140]. The main challenge of designing a DNP-NMR probe is to incorporate both RF coil and microwave cavity around the sample of interest. In principle, the ENDOR (electron nuclear double resonance) probes used in EPR spectroscopy at low magnetic fields have the capability to perform DNP-NMR experiment by adding an extra rf isolation and detection capability. Such double-resonant structure (Section 5.2.1) has the advantage that high quality factors Q can be attained for both μw and rf channels. Nevertheless, the situation becomes more challenging at higher fields as the microwave wavelengths become shorter, i.e. it might obstruct the design of NMR coil and it can only accommodate smaller sample quantity. Another

level of complexity is present upon considering the integration of MAS stator with resonant cavity. In the current state-of-the-art DNP-MAS technology (Section 5.2.2), the microwave is only focused onto the sample via a lens without a resonant structure, i.e. possibly Q~ 1.

5.2.1 Resonators

In principle, the design of a high-Q microwave resonator can convert microwave power P to high Rabi frequency γB_1 efficiently since $\gamma B_1 \propto \sqrt{PQ}$. Unlike the radio waves generated by an NMR coil in free space, the travelling microwave waves form a standing wave inside a resonator as they are spatially confined by dimensions that are comparable to the wavelength λ. This allows the energy of the electromagnetic (EM) waves to be redistributed and concentrated at the maximum amplitude of the standing wave. Depending on the mode of standing wave employed in a resonator, the size of the *E* field can be curtailed at the position where *B* field is most intense. This is a desired feature, especially in the solution-state DNP because the interaction between a dipole and the *E* field causes unwanted heating in the sample.

For efficient NMR excitation and detection, an RF coil can be placed inside the cavity with the tuning/matching circuit placed outside the cavity. This 'coil in a cavity' structure operating at millimeter wave lengths becomes increasingly difficult at higher frequencies as the size of the cavity gets smaller with respect to increasing resonance frequency. For instances, $\lambda/2 \sim 1.5$ cm at 9.8 GHz (X-band) and ~1 mm for 140 GHz. Furthermore, the presence of the RF coil inside the cavity substantially perturbs the standing wave and hence reduces the Q-factor. An alternative approach is to wind the RF coil outside the cavity; however, slots/slits need to be cut into the cylinder walls to allow RF penetration.[113] A third approach is to employ the cavity wall itself as the RF coil, i.e. a 'ribbon-wound' design.[195] The design was adopted for DNP application at 140 GHz at MIT,[132] where a gold coated copper ribbon-wound acts simultaneously as a cylindrical TE_{011} mode cavity and an rf coil (Figure 19). The plungers with silver-

coated surfaces are used to tune the microwave cavity by moving the plungers into or further away from the center of the cavity. The simulated time averaged $\langle B_{1S} \rangle$ of this cavity is ~ 953 $\mu T/\sqrt{W}$ with a near constant field strengths and Q-factor over more than 1 GHz tuning range. Additionally, it can be either a $^{1}H/^{13}C$ or $^{1}H/^{15}N$ double resonant probe depending on the attached tuning/matching box. Since high rf power is needed in solid-state NMR to perform cross polarization or decoupling, the close proximity of the waveguide to the RF coil causes it to prone to arc. Nevertheless, this issue was circumvented by designing a balanced RF circuit.[196,197] An additional benefit of having a balanced rf circuit is that it ensures better rf homogeneity across the sample.

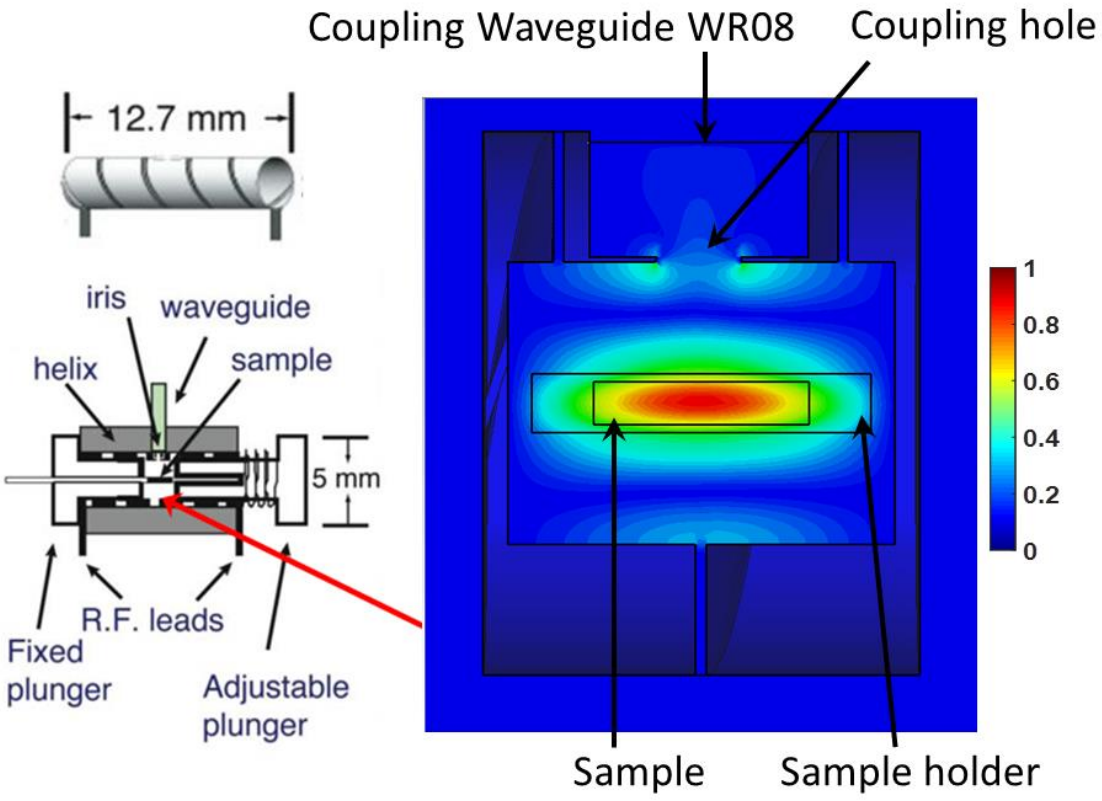

Figure 19: Flat wound coil resonator at 140 GHz acting as both cavity and RF coil. The simulated magnetic field of the TE_{011} mode inside the coil showing transverse *B*-field at the sample location transverse to the main NMR magnetic field.

Again, the reduction in cavity size at higher frequencies severely limits the sample volume. One approach to overcome this size limitation is to design an overmoded cavity. While a fundamental mode

resonant cavity restricts the sample size significantly below the wavelength in all three dimensions, an overmoded cavity restricts the sample size below the wavelength only in one dimension. Prisner et al. have successfully fabricated such an overmoded cavity for solution state DNP at 400MHz NMR/263GHz EPR. This probe works as a Fabry–Pérot resonator for the microwave and a stripline resonator for NMR.[198]

5.2.2 MAS-DNP NMR Probes

For DNP, conventional solid-state NMR probes need to be modified for cryogenic MAS and for efficient microwave irradiation at the sample. Hence, vacuum-jacketed transfer lines for the delivery of cryogenic gases as well as waveguides for propagation of microwave irradiation need to be incorporated into the probe design. Furthermore, to ensure that there is good thermal insulation between the magnet bore/shim stack and the DNP probe, the probe needs to be placed inside a vacuum jacketed cryostat. A diagram of this cryostat can be seen in Figure 20. All of these requirements must be achieved within the limited space available inside the magnet bore.

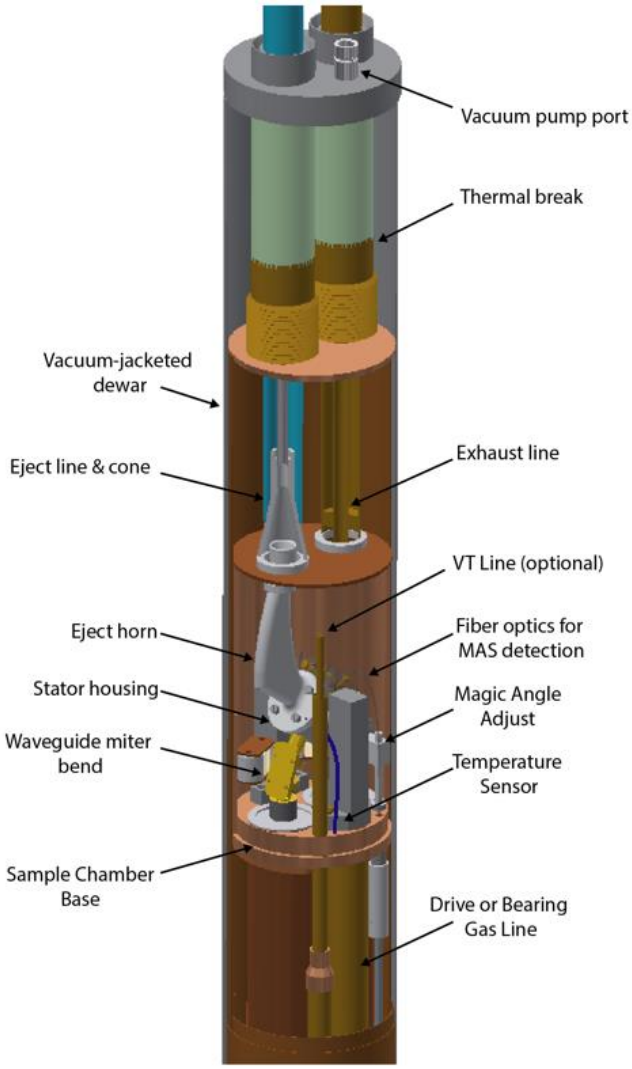

Figure 20: Design of a cryostat in a DNP probe. The sample chamber is housed in a low-temperature oven, thermally insulated from the bore of the magnet via a vacuum-jacketed dewar. The dewar contains two ports for a vacuum-jacketed exhaust line as well as a sample insert/eject tube.

In typical locally tuned probes, the tuning and matching elements are in close proximity to the RF coil and are situated near the cooling area within a DNP probe. This is the approach taken by Tycko et al.[199] as well as Bruker. Care must be taken to ensure that the tuning and matching elements remain thermally isolated. In many cases, remotely tuned transmission line (TL) probes, where the tuning and matching elements are placed outside the sample cooling area, are often preferred for DNP application.[164,200,201] In these TL probes the tuning and matching elements are kept outside the magnet bore, at room temperature

and separated from the RF coil(s) by the transmission line, mitigating space limitations near the sample chamber as well as temperature-induced changes in the properties of the RF circuit.

Though DNP-MAS probes have a resonant RF circuit with high Q for multiple channels, the stator housing that holds the RF coil does not act as a resonant microwave cavity, i.e. low Q for microwave irradiation. Due to the space constraints the corrugated waveguide inside the probe has a smaller diameter than the waveguide transmitting microwaves from the source to the probe. The outer, larger diameter waveguide is coupled with the probe waveguide either quasi optically or by employing down tapers. In most designs microwaves enter through the bottom of the probe and are reflected vertically upwards by a miter bend. At the sample chamber, another miter bend at the magic angle (Figure 21a) reflects the microwaves into the sample at an angle perpendicular to the rotor axis. The sample is surrounded by a holder (rotor) of a different material (sapphire or zirconia) and the rotor is itself surrounded by a metallic structure (the NMR coil) that reflects terahertz radiation. This irradiation technique causes scattering and diffraction of the microwave beam by the RF coil resulting in non-uniform microwave distribution (Figure 21b) across the sample.[202,203]

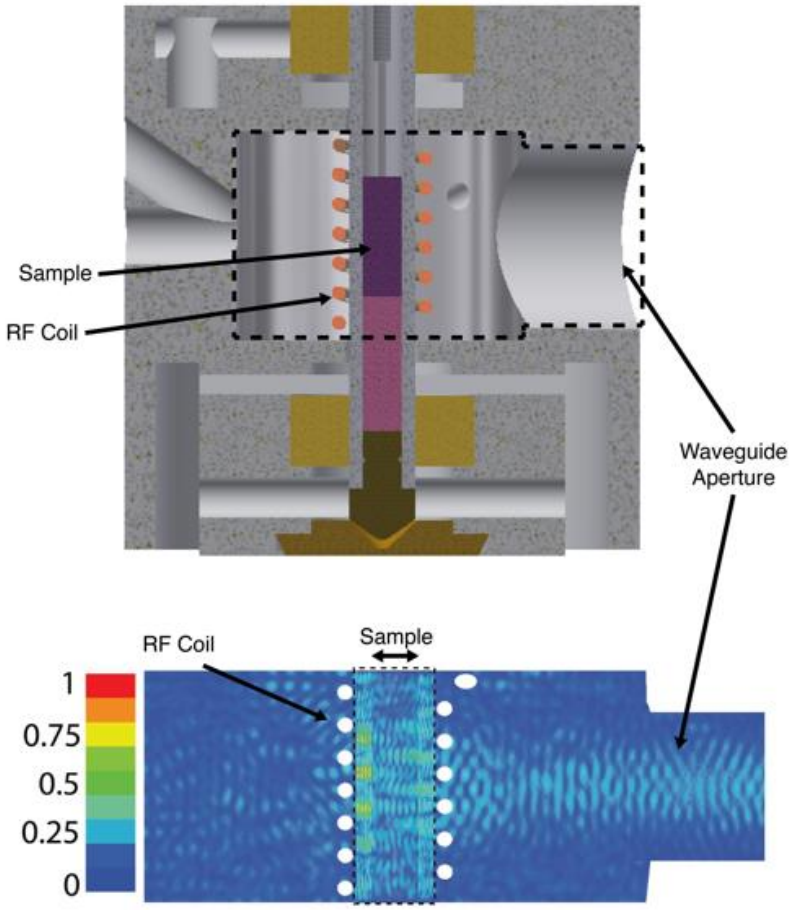

Figure 21: (Top) CAD drawing of the stator housing with the sample and RF coil. (Bottom) Microwave field distribution inside the sample chamber (dashed region in top picture). Diffraction of microwaves can be observed at the RF coils. Microwaves are absorbed in a single pass through the sample and scattered in the chamber housing.

The mechanical assembly of the sample and the surrounding components in the probe make it challenging to achieve high microwave coupling efficiency to the sample chamber. Detailed electromagnetic coupling studies have been very limited in the past, with first major study performed at MIT[202] and then followed by others.[203-205] The electromagnetic modeling predicts that only ~ 5 % of the incident power is deposited into the sample. The remaining of the power, ~ 35 % is reflected back into the waveguide and ~ 60% of the power is scattered and deposited ohmically in the stator and RF coil. The scattering effect can be minimized by using an RF coil with non-uniform pitch where the gap between the central turns of the coil are larger or by embedding the particles of high dielectric constant into the frozen

sample.[202,204] Attempts have also been made to improve the microwave field strength at the sample by coating the inner surface of the stator housing with reflective materials and focusing the microwave irradiation through a lens made from materials that refract microwave, i.e. Teflon. Another alternative approach is to employ microwave irradiation along the rotor axis.[192,200,206] In this case microwaves are launched from the top of the magnet and directly in to the sample chamber, avoiding the need for a waveguide passing through the probe body. This may be an easier approach if one intends to modify a commercial probe for DNP applications. Studies of power coupling optimization can significantly reduce the microwave power requirements. Although the gyrotrons are capable of generating tens of watts of power, excess power may result in overheating in the sample chamber. Novel coupling schemes using state-of-the-art electromagnetics simulations are therefore necessary to further increase the DNP efficiency. Further, a DNP-MAS probe needs to have provisions for cryogenic sample spinning. The simplest regime to achieve this is to employ cold bearing and drive gas only, while an extra variable-temperature (VT) system could be introduced as the third passage for VT experiments. We will discuss the details of the cryogenic system in the next section.

5.3 Cryogenic MAS

The size of DNP enhancement factor depends on the efficiency to saturate either the allowed or forbidden EPR transitions. (Section 2), depending on the type of dominant DNP mechanism. As the transitions are most easily saturated when the relaxation rates are slow, it is necessary to cool the sample at cryogenic temperatures to prolong the relaxation times. Thus, MAS-DNP experiments are typically conducted at temperatures between 20-180 K by employing either cold nitrogen (Section 5.3.1) or helium (Section 5.3.2) gas for cooling the sample directly, as well as spinning the rotor. Some of the main considerations in assembling a cryogenic MAS setup include the type of cryogenics (N_2 or He gas), cost of operation, type of DNP applications, experimental time due to prolonged T_1 at low temperatures, etc. Nevertheless, we will discuss the setup of a standard cryogenic MAS system here.

5.3.1 Nitrogen Spinning

Two different methods are employed to generate the nitrogen gas: (1) using the boil-off from liquid nitrogen dewars and (2) using a nitrogen separator. The former method has the advantage that pure nitrogen gas without moisture can be obtained very easily. Although using a nitrogen separator is comparatively cheaper, care must be taken to remove any moisture content in order to avoid frosting inside the heat exchanger and/or the probe during the experiment. A typical DNP setup utilizing a nitrogen separator can be seen in Figure 22. Nitrogen gas generated by either of these methods is at room temperature and is sent to a heat exchanger for cooling. The heat exchanger has a coil-in-a-can design. Pressure regulated input gas enters the heat exchanger through a copper tube, which is coiled at the bottom, and exits through the other end of the coil. This tube is vacuum-jacketed, except at the coiled region, and is placed inside an external pressurized copper can. Upon pressurizing the can, the nitrogen gas inside the can gets partially condensed to a liquid and cools down the MAS gas passing through the inner copper tube. It is important to maintain a higher pressure inside the can than the MAS gas flow to avoid liquefaction. Hence, controlling the can pressure will change the level of liquid nitrogen inside the can, which in turns regulate the gas temperature.

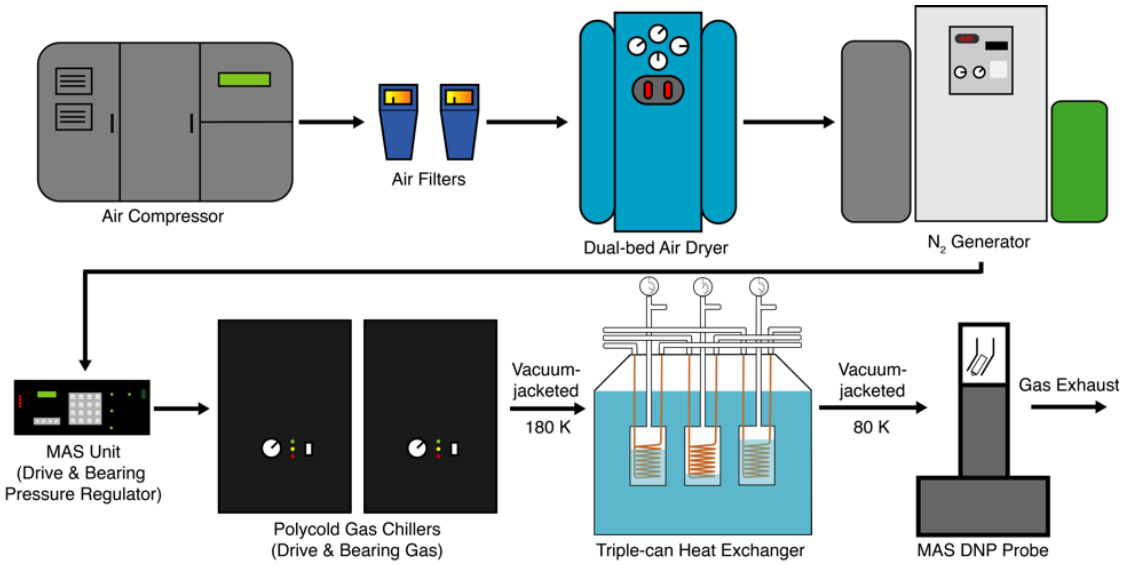

Figure 22: Schematic of DNP setup with a nitrogen generator. Room temperature air from a compressor first passes through a series of filters and dryers to remove dirt and moisture. The dry air is then sent to a nitrogen generator where pure (>99%) nitrogen gas is generated. From there, the purified nitrogen gas is sent to a pressure regulation unit before flowing through a pre-cooling refrigerator (optional) and heat exchanger to cool down to low temperatures before entering the probe.

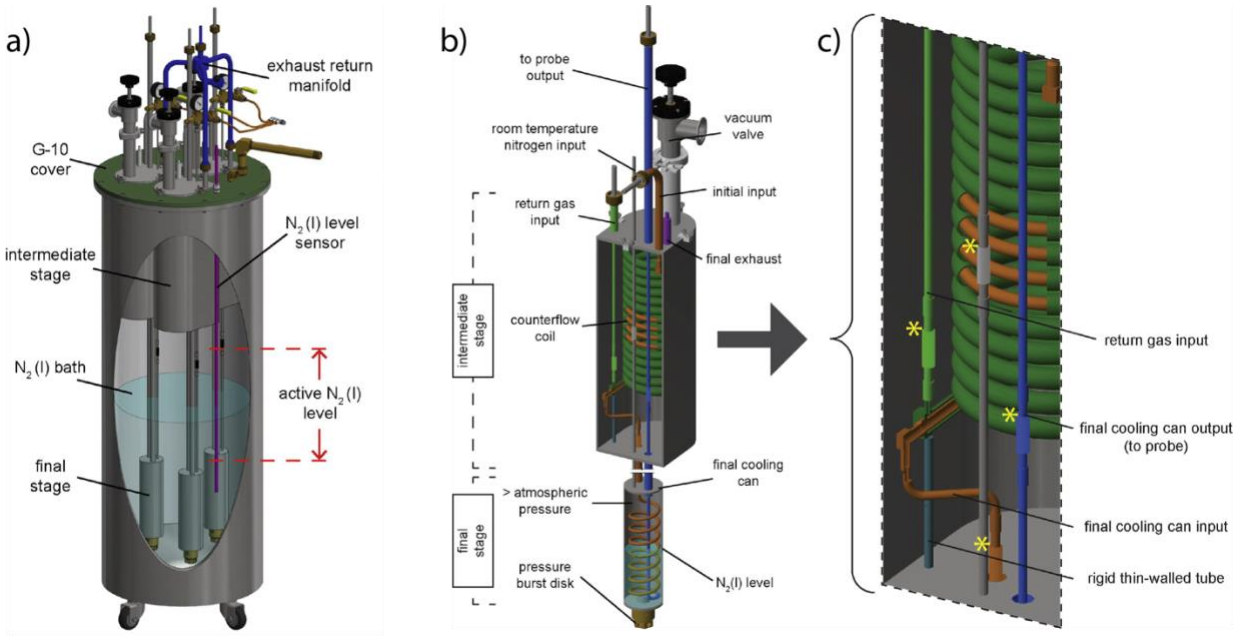

Figure 23: (a) Overview of a triple-can heat exchanger setup utilizing return gas from the probe to assist in cooling of the drive, bearing and VT gas. (b and c) Detailed view of the intermediate stage of the heat exchanger setup.

In earlier designs, a common heat exchanger can was used to cool down bearing, drive and VT (if present) gases. For better control and cooling efficiency, it is advantageous to use separate heat exchanger cans for bearing, drive and VT. Hence, current cooling systems employ separate triple can heat exchanger (Figure 23a) for each passage. These cans are placed in an external vacuum-jacketed liquid nitrogen dewar so that the MAS gases can cool down efficiently. Periodic refilling of this dewar is necessary to maintain a stable gas temperature. Liquid nitrogen consumption from the dewar can be minimized by precooling the MAS gases before it enters the heat exchanger. Recently, Barnes and coworkers have developed a heat exchanger (Figure 23) that uses less than 90 L/day of liquid nitrogen to cool MAS gases.[207] In this design, the cold returning gas from the MAS probe is transported back to the heat exchanger to reduce the liquid nitrogen consumption. In addition, there are built-in heaters on the transfer lines to maintain the gas temperature.

5.3.2 Helium Spinning

In order to perform experiments below 80 K, helium gas is preferred over the nitrogen gas as the cryogenics despite the higher cost. A cost-effective strategy was implemented by Tycko et al. where helium is used for cooling only keeping nitrogen gas for spinning.[199,208,209] An elongated Zirconia rotor with poor thermal conductivity is necessary in this case to avoid condensation of nitrogen gas at the center of the rotor. Though this method minimizes helium consumption, i.e. to 1.3 L/h for $T < 30$ K,[209] mixing of the gases makes it unviable to recover helium. A more economical and practical option is to design a closed helium recovery system (Figure 24).[101,210-212] NUMOC, developed by the Grenoble team, is a semi-closed loop helium recovery system utilizing liquid helium as the cooling source for the MAS gases. This design consumes an average of 5-25 L/h of helium depending on the desired temperature. It is still an ongoing development to upgrade the system to a closed-loop helium recovery system, SACRYPAN. The Osaka design developed by Matsuki and coworkers is closed-loop and capable of maintaining stable MAS frequencies (+/- 5 Hz) and temperatures (+/-0.5 K) for weeks at a time, with running costs as low as ~$3/h.

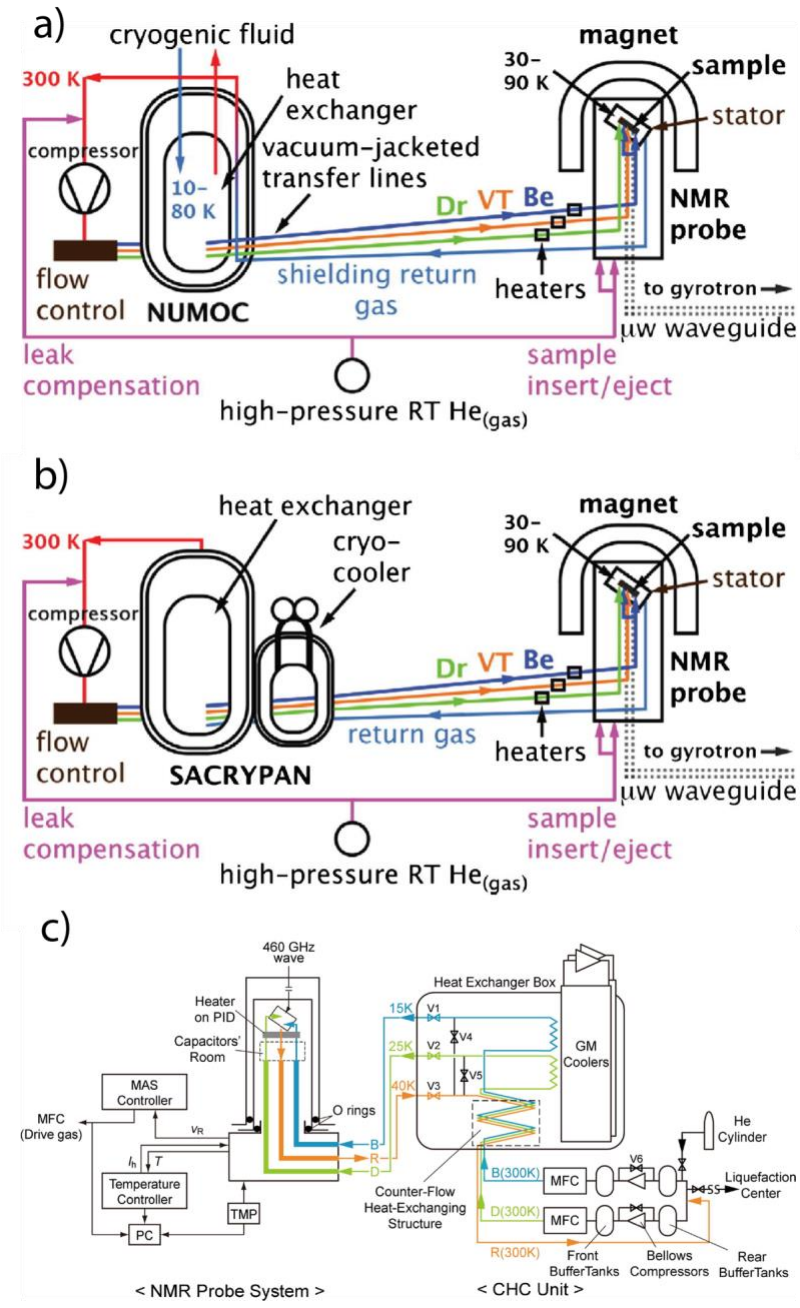

Figure 24: (a and b) Layout of the helium recovery systems, NUMOC and SACRYPAN. (c) Helium recovery system built by Matsuki and coworkers.

5.3.3 Fast MAS DNP

It was shown recently that not only faster MAS frequency increases the NMR resolution for both biological samples and inorganic materials, it also enables higher DNP enhancements.[43,213,214] However,

the maximum MAS frequency ω of a rotor is determined by the rotor material and the speed of sound v_S at the drive tips, i.e. the tangential velocity v has to fulfill the inequality $v = r\omega < v_S$ to avoid shock wave and turbulences.[215,216] Nevertheless, the MAS frequency ω can adopt higher values if a smaller rotor with diameter $d = 2r$ is employed. For examples, the maximum MAS frequencies of the commercial probes are 15, 25, and 40 kHz for the 3.2, 1.9, and 1.3 mm DNP probes, respectively at 100 K. The maximum MAS frequencies decrease at low temperatures because the density of the gas is higher and the speed of sound is lower. For instance, the speed of sound in nitrogen reduces by approximately half from a temperature of 300 K to 90 K at 2 bar of pressure. It is worth noticing that the speed of sound in helium remains much higher than nitrogen at all temperatures, i.e. the speed of sound in helium at 35 K is similar to that of nitrogen at room temperature.[101] Hence, much higher spinning frequencies can be achieved by employing helium gas instead of nitrogen for MAS. Recently, spinning frequencies of 25 kHz were achieved with a 3.2 mm zirconia rotor at 90 K by employing helium gas cooled by nitrogen.[210] Another technical challenge in using smaller rotors is that it is difficult to integrate a sample eject system with the stator because the lighter rotors are more prone to eject out without a mechanism to hold them in place. More recently, a suction assembly has been developed by Bruker Inc. to sustain stable MAS at DNP temperatures without a cap on the stator.

5.3.4 Rotor Materials

In order to achieve faster MAS frequencies and higher DNP enhancements, the three most important material properties (Table 1) of a DNP-MAS rotor are thermal conductivity, microwave absorption/permittivity and flexural strength. Thus, sapphire rotors are often employed than the zirconia rotors because of superior heat dissipation and microwave penetration. It was reported that the DNP enhancements are typically 20% higher in sapphire than zirconia rotors. However, sapphire is more fragile than zirconia and thus the maximum spinning frequency is lower. This can be circumvented by a diamond rotor, which is an ideal material for DNP application due to its excellent strength, microwave penetration, and thermal conductivity.

Table 1. Comparison of the properties of zirconia, sapphire, and diamond at room temperature.[217]

Property	Material		
	Zirconia 3Y-TZP	Sapphire	Synthetic Diamond (CVD)
Density $\left(\frac{\mathrm{g}}{\mathrm{cm}^3}\right)$	6.04	3.97	3.51[218]
Youngs Modulus (GPa)	205	468	1050
Tensile Strength (MPa)	-	399	1000
Compressive Strength (MPa)	2500	2930	~1000
Flexural Strength (MPa)	965	689	-
Thermal Conductivity $\left(\frac{\mathrm{W}}{\mathrm{mK}}\right)$	2	46	2000
Thermal Diffusivity $\left(\frac{\mathrm{cm}^2}{\mathrm{s}}\right)$	-	0.123	2.97
Thermal Expansion $(10^{-6}\mathrm{K}^{-1})$	11	8	0.8[218]
Heat Capacity $\left(\frac{\mathrm{J}}{\mathrm{gK}}\right)$	-	0.764	0.516
Poisson's Ratio	0.30	0.28	~0.2
Permittivity ϵ_{r} (170 GHz)	-	9.7	5.674
Loss Tangent $tan\delta$ 10^{-5} (170 GHz)		15	1-2

6 Applications

Prior to the development of the hyperpolarization techniques, conventional NMR experiments often require special labeling schemes like ^{13}C or ^{15}N isotope enrichments, or large sample quantity to obtain satisfactory sensitivity. One of the solutions to this issue is to integrate the DNP technique into the existing NMR experiments, which allow natural abundance materials[92] to be studied without expensive and possibly challenging isotope labelling or having long acquisition times. The DNP-NMR technique has enabled access to structural information or molecular mechanism that are otherwise beyond its reach. While the enhancement of the solution-state DNP technique is fundamentally limited by the relaxation mechanisms at high magnetic fields, we will focus on the DNP applications incorporated into solid-state MAS experiments. Earliest known solid-state DNP studies were undertaken by Wind[140,219-221] and Schafer[141,222-224], primarily to study coal, diamond polymers, and other materials at room temperature. The application was further extended to biologically relevant sample at cryogenic temperature with amino acids and a protein, T4 lysozyme.[225,226] Thereafter, cryogenic MAS-DNP has been employed in various

fields of solid-state NMR, particularly biological macromolecules, porous materials, natural abundance pharmaceutical products, quantum dots[227], Lithium batteries[228], etc. In this review article, we will focus on the recent MAS-DNP applications on biological solids (Section 6.1) and inorganic materials (Section 6.2).

6.1 Biological Applications

While the sensitivity enhancement from DNP yields significant advantage to any biomolecular NMR experiment, there are additional considerations for its application, particularly of the effects of low temperatures on biomolecular structure and function. At low temperatures, many NMR peaks broaden inhomogeneously due to the presence of multiple molecular conformations whose contributions to the lineshape are no longer averaged by the temperature-dependent dynamics. Therefore, DNP is best suited to rigid biological samples, or for samples with sites whose chemical shifts are unique, so that the peaks remain unambiguously assigned even at low temperature. Some examples of rigid systems are amyloid fibrils (Section 6.1.1) such as $A\beta_{40}$[229] and other supramolecular assemblies such as Type III secretion system (T3SS) needles (Section 6.1.3). Systems with a unique chemical shift include the membrane protein bacteriorhodopsin (bR),[230-232] with a well-resolved Schiff base which is of mechanistic interest (Section 6.1.2). On the other hand, a chemical shift can also be made unique through careful isotope labeling scheme, which was employed to study drug binding to the membrane protein $M2_{18-60}$ (Section 6.1.2).

In some cases, the low temperature may offer certain advantages or be required, thereby facilitating the use of DNP as something of a natural choice. For example, the low temperature may enable the trapping of mechanistic intermediates in bR, and enabling the study of drug binding to M2 by quenching interfering dynamics. Another interesting type of dynamics present in protein samples is threefold hopping of methyl groups. When the hopping rate becomes comparable to the proton

decoupling field strength at low temperatures, i.e. in an intermediate-exchange regime, the peaks could have broader linewidths. To mitigate this problem, one can adjust the temperature to avoid the intermediate-exchange regime, or simply deuterate the methyl groups.[233,234] The choice of deuteration is particularly apt for DNP since it can often yield high-resolution spectra and higher DNP efficiency (see Figure 25a).

With these considerations in mind, DNP has been successfully applied to many biological macromolecules including small peptides,[235] amyloid fibrils,[143,229,236-238] membrane proteins,[91,230-232,239-247] ribosomes,[248] bacteriophages,[214,249] nucleic acids,[250] and other protein complexes.[251-256]

6.1.1 Amyloid Fibrils

Amyloid fibrils are self-aggregate proteins that are of interest to the biochemistry community due to their relevance to diseases including Alzheimer's disease (AD), Parkinson's disease, and type-2 diabetes. Since the fibrils are insoluble and non-crystalline, solid-state NMR is an indispensable tool for studying these systems, and DNP has been applied to further probe their chemical properties.

The amyloid forming peptide 'GNNQQNY', extracted from the yeast prion protein Sup35p, was the first fibril to be studied with DNP. Depending on the experimental condition, GNNQQNY can form nanocrystals or amyloid fibrils. Using isotopically-enriched nanocrystals, Van der Wel et al. showed that nanocrystals with a size up to 1 μm can be efficiently polarized via DNP,[235] and the study was extended to multidimensional correlation experiments on both GNNQQNY nanocrystals and fibrils.[236] It was shown that the chemical shifts of the water-accessible residues change upon cooling to cryogenic temperature in the case of nanocrystals while the effects are minimal in the case of fibrils.

After the initial study on GNNQQNY, the DNP technique was applied to larger amyloidogenic proteins like transthyretin (TTR105-115)[238] and the 86-residue SH3 domain of PI3 kinase (PI3-SH3). [237] In the latter case, a large number of additional contacts, especially in the aromatic region (Figure 25b) were discovered via DNP-enhanced ZF-TEDOR. This is because at room temperature, the rates of

dynamic processes like the aromatic ring-flip motion are in the regime that interferes with cross polarization or decoupling during NMR experiments, resulting in quenched signal intensities or line-broadening. Here, the cryogenic temperature requirement of DNP has other advantages, namely the recovery of signals that are otherwise unobservable at room temperature.

DNP has also been applied to amyloid-β (Aβ), the self-assembled fibrils of which are believed to be responsible for AD. Potapov et al. have exploited the advantages of DNP to probe four different self-assembly stages of Aβ (Figure 25c), where the amount of protein sample available in each transient stage is limited. It was confirmed that the parallel intermolecular alignment observed in Aβ_{40} develops only at the final stages of fibril formation.[143]

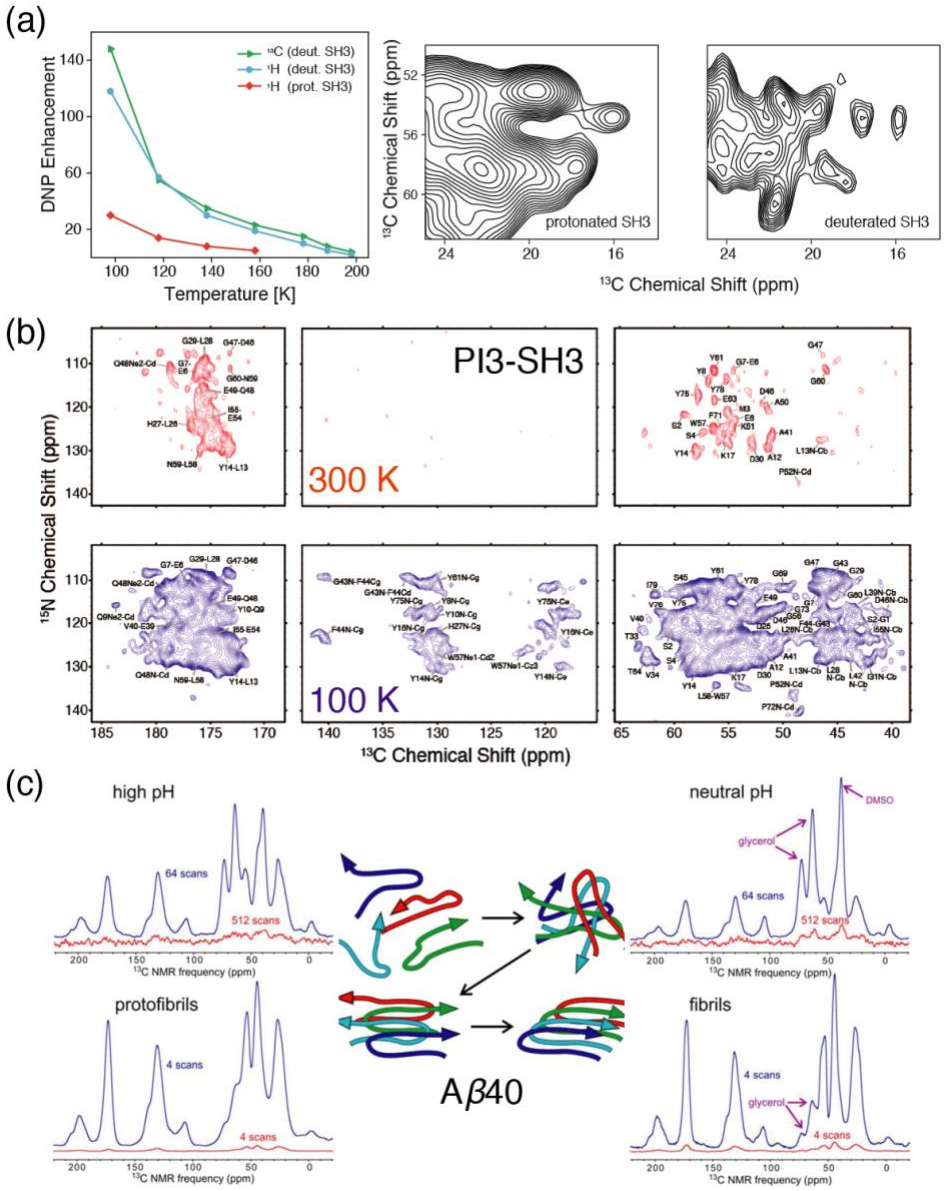

Figure 25: (a) s Effect of deuteration in PI3-SH3 on enhancement (left) and resolution (right). (b) The ring-flip motions in the aromatic region interferes with NMR experiments and therefore not visible at 300 K (top and red), but the aromatic peaks reappear at a lower temperature of 100K (bottom and purple). (c) The figure shows the spectra of Aβ at different self-assembly stages with the microwave turned on (blue) or off (red). Reprinted with permission from ref [143,257,258]. (amyloid.ai)

6.1.2 Membrane Proteins

Like amyloid fibrils, membrane proteins are of significant biochemical relevance and are not well-suited to study by atomistic-resolution techniques other than ssNMR. In particular, DNP-NMR has been applied to the membrane protein bacteriorhodopsin (bR),[230-232] which acts as a light driven ion pump transporting protons for ATP synthase in archaea. The translocation of protons is facilitated by the Schiff base (SB), formed between the chromophore retinal and Lys216, and its nearby counterion residues. Upon light irradiation, bR proceeds through a photocycle forming a series of intermediates labeled K, L, M, N, and O with effective shuttling of a proton during these steps. These intermediates can be trapped cryogenically, but the relative proportion of an individual state can be quite low. As such, DNP is a valuable technique in this case to boost the sensitivity since the study already requires low temperature. Some of the initial studies with DNP involved using ξ-^{15}N lysine labeled bR. Mak-Jurkauskas et al. reported the first NMR spectrum of the K-intermediate and identified four different conformations for the L intermediate.[230] Later ^{13}C-^{15}N correlation experiments with a U-^{13}C,^{15}N-labeled bR sample permitted unambiguous identification of several co-existing states and it was found that only one of the four L intermediates is functional and proceeds thereafter in the photocycle.[231] Nevertheless, details of bR's primary proton transfer step from the SB to Asp85 are still unclear. It was suggested in the earlier literature that there are three possible pathways that contained the lowest energy barriers,[259] in particular the path B (Figure 26a), where the proton is relayed to Asp85 via Thr89. The recent multidimensional correlation DNP-NMR experiments performed in our laboratory had indicated the presence of an alcohol group in the M_o intermediate (Figure 26b).[239] Moreover, ^{13}C-^{13}C spectra showed correlations between the C_γ of Asp85 and the alcohol carbon of Thr89 (the only alcohol-containing residue close to the SB) in L and in M_o. Finally, $^{13}C_\gamma$(Asp85)-^{15}N(SB) distance measurements across the active site reveal helical movements between helices C and G, the two come closer together just before the primary transfer and relax thereafter. In conclusion, all experiments converged in pointing to path B as the primary proton transfer pathway and that these findings would not have been possible without DNP.

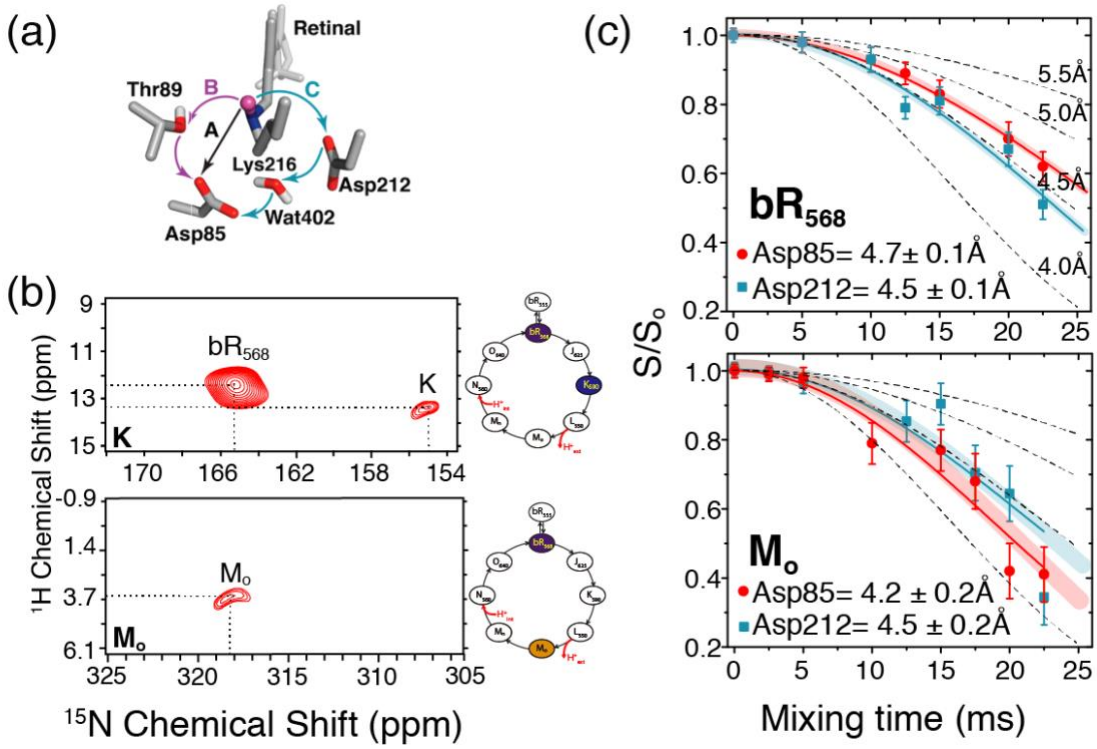

Figure 26: Proposals for the primary proton transfer pathway in bR. (b) DNP enhanced ^{15}N-^{1}H HETCOR spectra showing a downfield 1H chemical shift of 3.6 ppm in Mo, indicative an alcohol. (c) DNP enhanced 3D FS-REDOR experiments are used to obtain distances from the SB nitrogen to the Cϒ of Asp85(red) and Asp212 (blue), shown together with simulated curves (black dotted line). (Br.ai)

Channelrhodopsin-2 (ChR2) is another retinylidene membrane protein of the rhodopsin family that has been investigated using DNP-NMR. The cis-trans isomerization of the ChR2 retinal was studied by employing U-^{15}N ChR2 with 14,15-$^{13}C_2$ labeled retinal reconstituted into lipid bilayers.[240] From the retinal ^{13}C chemical shifts and the DQ buildup rates, existence of 100% *trans* form in the dark adapted state was confirmed unambiguously. Furthermore, three different photocycle intermediates were identified with ^{13}C DQF and ^{15}N DCP DNP-enhanced 1D spectra.

Oligomerization of membrane proteins is a commonly observed phenomenon. Maciejko et al. have studied the interprotomer interactions within the oligomers formed by the membrane protein green proteorhodopsin (GPR) by observing the interprotomer contacts in DNP-enhanced ^{15}N-^{13}C TEDOR

spectra.[241] Interprotomer ^{13}C-^{15}N interfaces were created by mixing individually ^{13}C and ^{15}N labeled protomers in a 1:1 ratio and reconstituting them into a lipid bilayer to form mixed labelled pentamers. Their studies indicated that Lys and Arg residues play a major role in the interprotomer interactions and that a salt bridge between Arg51-Asp52 residues is necessary for oligomer stabilization and it acts as a switch between pentamer and hexamer conformations.

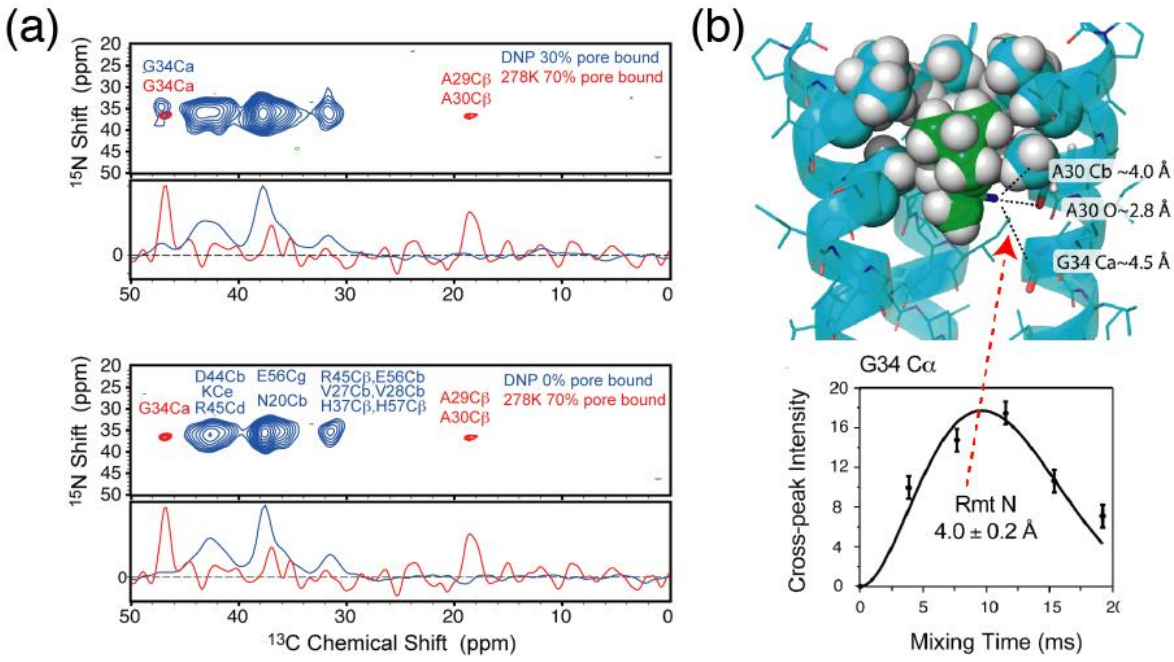

Figure 27: (a) The DNP-enhanced ZF-TEDOR spectra between the ^{13}C-labeled protein and ^{15}N-labeled drug shows that the shift in the ^{13}C resonance is correlated with the pore binding site. (b) The proposed structural model of the drug binding site with distance constraints obtained from the DNP-assisted distance measurement technique. Reprinted with permission from ref [260] (Source: BioApp3.png)

DNP can also be applied to investigation of protein-ligand interactions with NMR. For instance, Andreas et al. have studied the binding of the antiviral drug rimantadine (Rmt) to the membrane protein $M2_{18\text{-}60}$, the proton transporter from the Influenza A virus.[242] As the binding ligand is non-rigid and susceptible to dynamics at high temperatures, it was essential to perform the NMR experiment at cryogenic temperature to quench the dynamics, facilitating signal enhancement using DNP. Moreover, a

structural model of the drug bound to the protein was suggested using the distance constraints determined using the DNP-enhanced TEDOR sequence (Figure 27).

DNP has also been applied to the study of substrate binding to EmrE, a small four transmembrane protein from *E. coli*.[243] EmrE transports positively charged polyaromatic compounds in exchange for protons. A direct contact between the substrate tetraphenylphosphonium (TPP^+) and Glu14 residue was observed in a DNP-enhanced ^{13}C-^{13}C DARR spectrum employing sparsely ^{13}C labeled EmrE and ^{13}C labeled TPP^+.

Human ABC transporter associated with antigen processing (TAP) is another membrane protein-substrate system that has been studied with DNP enhanced solid state NMR.[244] Atomic scale backbone conformations of an antigenic peptide, KRYQNSTVY, bound to TAP were determined and the peptide binding cavity was identified. More recently, a study on the effect of drug binding on specific sites in transmembrane helices 4 and 6 of another ABC exporter MsbA was reported.[245]

All the studies discussed so far have been conducted with protein samples after extensive purification protocols and reconstitution, which can be a very tedious process. There have been some attempts in the literature to study the membrane proteins in their native membranes without purification and reconstitution, made viable through the enhanced sensitivity with DNP.[246,247]

6.1.3 Other Biological Systems

Phytochromes are photoreceptors that regulate various aspects of plant growth. Stoppler et al. studied the functional sensory module of the cyanobacterial phytochrome Cph1 with DNP enhanced MAS NMR.[253] The chromophore, phycocyanobilin (PCB) is covalently bound to Cys259 of the protein. PCB has four pyrrole rings in its structure with a single positive charge. DNP enhanced chemical shift assignments helped to identify the localization of the positive charge in the chromophore and its interaction with functionally relevant water molecules.

Proteins with intrinsically disordered regions (IDRs)[261] are found in many biological systems, posing a challenge for structural characterization. The yeast prion domain of the protein Sup35 in the purified form has an N-terminal domain (N) that adopts a beta-sheet-rich amyloid conformation next to an intrinsically disordered domain (M), otherwise known as MN. However, the structure could be different in vivo. With DNP, Fredrick et al.[254] have studied the prion fibrils in a complex cellular environment and established that the fibril structure is different from the purified form especially in the disordered region.[254] Furthermore, the intrinsically disordered region of M is shown to make many direct interactions with the cellular components.

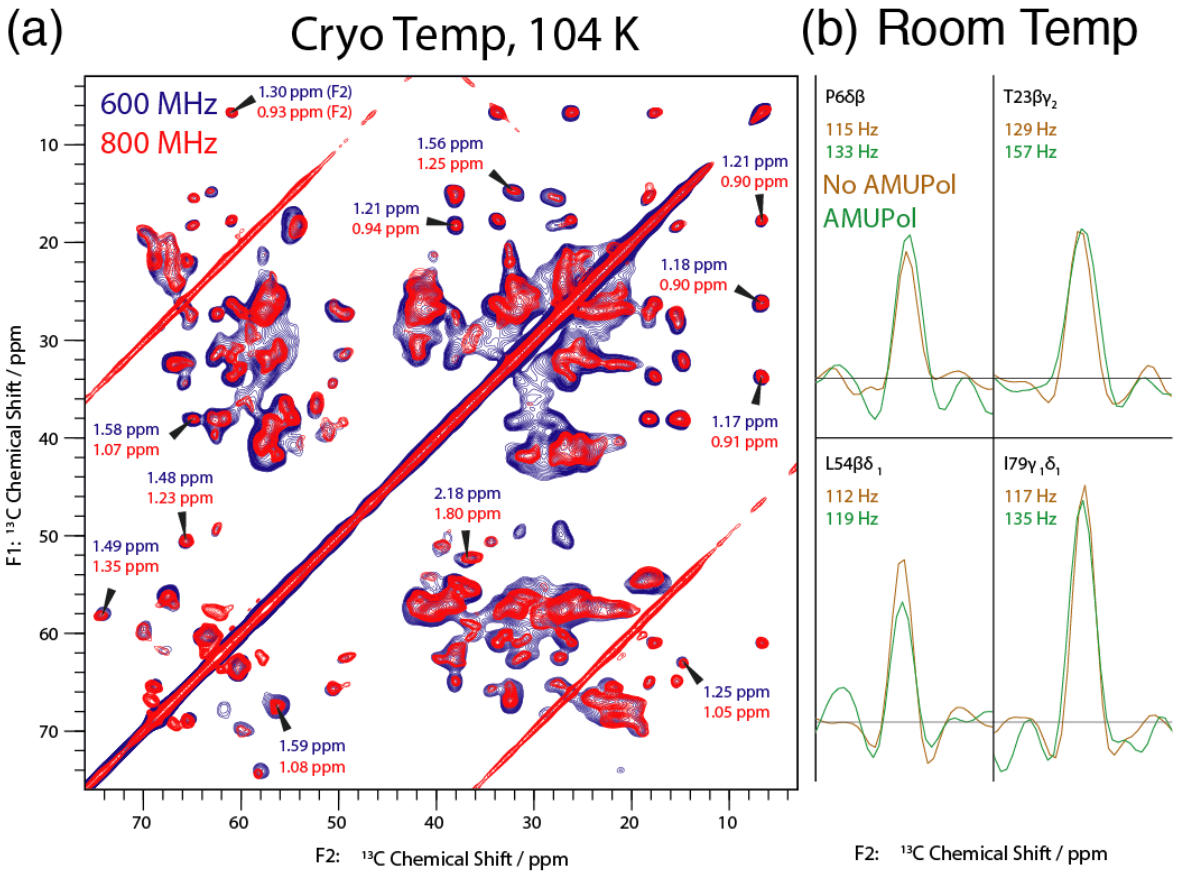

Figure 28: (a) The MxiH needles exhibit higher resolution DNP-NMR spectra at higher magnetic fields. (b) The room-temperature spectra show minor line-broadening effect due to addition of the radical AMUPOL. Reprinted with permission from ref [256] (Source:T3SS.png)

T3SS needle is a supramolecular assembly of the protein MxiH, which is sufficiently rigid that the linewidths of the peaks in DNP experiments are mostly dominated by the homogeneous contribution. Figure 28a shows the DNP-enhanced 2D spectra of the needle sample at 104 K at two different fields, 600 MHz and 800 MHz. It was shown that the resolution is improved by 22 % when the magnetic field is higher, confirming that the lines are homogeneously broadened. Moreover, Figure 28b shows that the addition of radical has limited influence on the same T3SS sample. In addition to higher magnetic fields, the homogeneous components can also be minimized by exploiting faster MAS frequencies. This was demonstrated experimentally on the study of Acinetobacter phage 205 (AP205) nucleocapsid,[262] showing that higher resolution can be achieved at faster MAS frequencies and higher fields (Figure 29). The high-resolution DNP-enhanced spectra have enabled the assignment of the aromatic resonances and long-range contacts in AP205 coat protein and its RNA, which were not observed at room temperature. A similar protein, the coat protein of Pf1 virus, was studied using a DNP-enhanced sequential side chain–side chain (S^3) correlation experiment for chemical-shift assignment.[214]

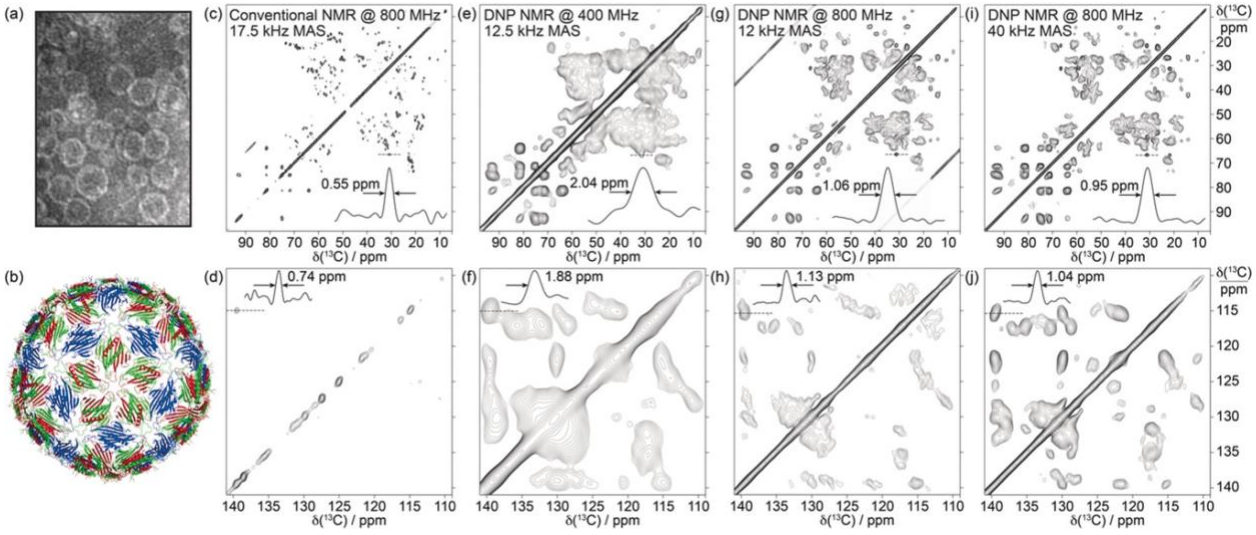

Figure 29: (a) TEM image and (b) 3D structure model of the AP205 nucleocapsids. The aliphatic-to-aliphatic (c, e, g, and i) and aromatic-to-aromatic (d, f, h, and j) regions of a DARR spectrum at (c and d) 800 MHz / 280 K / 17.5 kHz MAS, (e and f) 400 MHz / 107 K / 12.5 kHz MAS, (g and h) 800 MHz / 103 K / 12 kHz MAS, and (i and j) 800 MHz / 115 K / 40 kHz MAS. Reproduced from ref [262].

6.2 Inorganic Materials

MAS NMR is able to elucidate molecular structures at atomic resolution, quantify various solid-state forms, and probe molecular dynamics and chemical interactions in a non-destructive and non-invasive manner. It is therefore highly suitable for investigating systems that are powder in its native state such as zeolites and pharmaceutics. However, high throughput measurements of these systems by MAS are limited by the inherent low sensitivity. In addition, the detection scheme becomes more challenging when the major natural abundance nuclei are not NMR active, have a quadrupole moment owing to their high spin, or have low gyromagnetic ratios. Thus, the integration of DNP into solid-state NMR experiments has opened a new avenue to the spectroscopy of ^{13}C[263], ^{29}Si[264-267], ^{27}Al[43,268-270], ^{15}N[271], ^{89}Y[272], ^{17}O[273-276] and ^{119}Sn[277-279] nuclei in various systems.

A major development in the application of DNP for study of inorganic materials was introduced by Emsley and colleagues,[263] where powdered microcrystalline solids are wetted by incipient wetness impregnation with a solution of radical, enabling surface enhanced NMR spectroscopy by DNP (DNP-SENS). This impregnation technique is similar to the way that GNNQQNY nanocrystals were polarized in earlier literature.[235] The ^{1}H-^{1}H spin diffusion is an important step in the DNP-SENS technique to relay the enhanced polarization over a micrometer length scale, yielding a high overall sensitivity gain[280,281]. Figure 30 shows the natural abundance ^{13}C DNP SENS spectrum of an aromatic substrate covalently bound to the surface site of a silica framework.

Many nuclei involved in material studies are quadrupolar nuclei: for instance, ^{27}Al is a half-integer quadrupolar nucleus and thus the resolution of its central transition improves at higher magnetic fields and faster MAS frequencies. This is demonstrated clearly in Figure 31 where the Al (IV) site of mesoporous alumina is clearly visible at 18.8 T and 40 kHz MAS frequency, along with higher DNP efficiency (ε=16 at 40 kHz vs. ε=8 at 10 kHz).

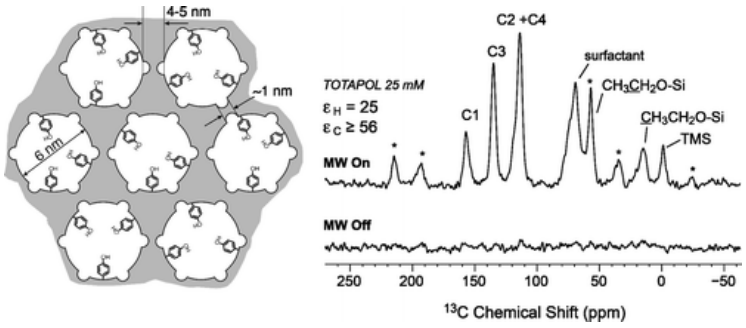

Figure 30: Left: Schematic representation of the pores [mesopores (6 nm diameter) are shown as circles and micropores (<1 nm diameter) as small half-circles] and channel network with phenol functionalities. The shaded gray area represents bulk silica. Right: ^{13}C DNP enhancements obtained for the surface substrates covalently incorporated into the silica framework. [Reproduced with permission from reference [263].]

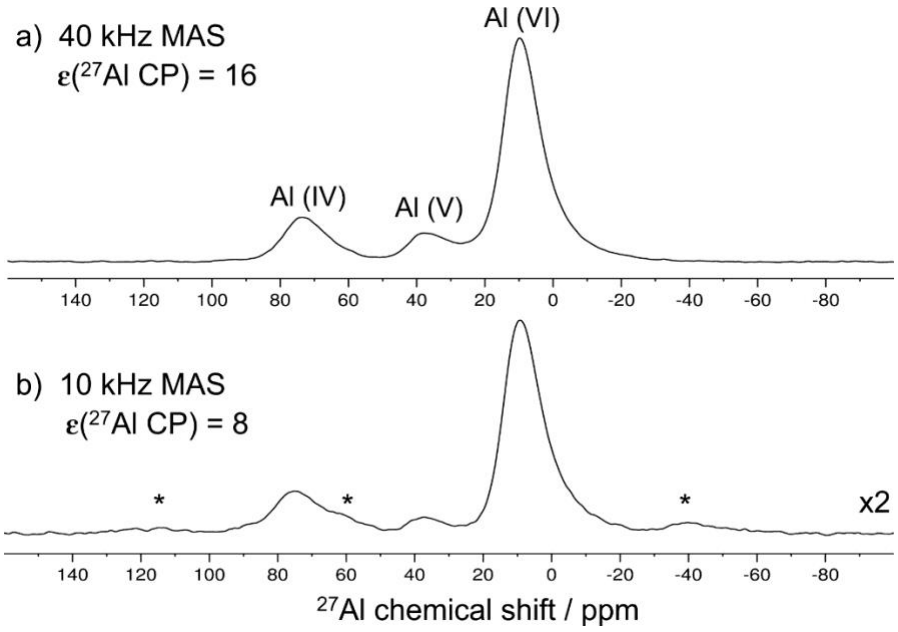

Figure 31: OE DNP-enhanced ^{27}Al cross-polarization (CP) MAS spectra of mesoporous alumina at 18.8 at (a) 40 kHz and (b) 10 kHz MAS frequency. [Reproduced with permission from reference [43]]

DNP exhibits considerable potential to advance the use of MAS NMR in the pharmaceutical sciences by alleviating the low NMR sensitivity in natural abundance drug systems. The major challenge remains in developing a suitable method to introduce polarizing agents into the sample for optimum signal enhancement with minimal sample perturbations. Emsley and coworkers demonstrated the first

impregnation method in DNP for the investigation of commercially available pharmaceuticals.[282] The impregnation method involves directly wetting the pharmaceutical formulations with the organic solvent (1,1,2,2-tetrachloroethane) containing polarizing agents for DNP experiments. Since then, numerous methods have been reported for preparing pharmaceutical samples for DNP, including polymer film casting, co-milling,[283] and glass forming methods.[284] An alternate approach to study pharamaceutical formulations was presented where the formulations during the research/developmental stage instead of the final stage were studied using DNP.[285] Specifically, the polarizing radicals are incorporated *in situ* and *sans* solvent matrix into the amorphous solid dispersion via the spray drying and hot-melt extrusion processes. On the other hand, a solvent-free method where the radical like TOTAPOL is covalently bonded to a peptide was demonstrated.[286,287] While it is important to prepare a glass-forming DNP matrix for better DNP efficiency, it is vital to ensure that both the polarizing agent and the solvent are compatible with the sample of interest.

7 Conclusions and Outlook

In this review article, we have presented a concise but comprehensive account on the theory, instrumentation, and applications of the DNP techniques on solid-state NMR. We have explained the basic operating principles and the recent developments of the CW- and pulsed DNP mechanisms. Although most DNP mechanisms exhibit efficient enhancement factors at moderate magnetic fields (less than 10 T), the observation that CW-DNP techniques become less efficient at higher magnetic fields remains a major challenge. There is ongoing interest and progress in further understanding and optimizing CE radicals for improved DNP enhancements using CW microwave irradiation. Nevertheless, we expect that a major improvement to DNP will be led by the development of novel pulsed DNP sequences and the newly discovered solid-state Overhauser effect in preparation for ever higher magnetic fields (^{1}H Larmor frequencies above 1 GHz).[288] To that end, further development in the DNP instrumentation including pulsed microwave sources (such as gyro-amplifiers), low-loss transmission waveguides, and high-Q

resonance structures will be imperative in attaining high DNP enhancements. Besides that, the biological applications of the DNP technique have not been extended to all biological samples yet mainly because of inhomogeneous line broadening at cryogenic temperatures. If the DNP methodology was to be more efficient and robust, we expect that a better compromise between enhancement factor and resolution can be reached at higher temperatures (> 200 K).[229,289] On the other hand, future development on the faster MAS techniques with diamond rotors and helium spinning, non-uniform sampling scheme, and ^{1}H-detected sequences can all be integrated into the DNP experiments to further extend the applications across different disciplines in NMR spectroscopy and possibly also MRI techniques.

8 Acknowledgements

We would like to thank Prof. Dr. Matthias Ernst, Prof. Dr. Gunnar Jeschke, Prof. Shimon Vega, Dr. Guinevere Mathies and Dr. Björn Corzilius for stimulating discussion. K.O.T. is supported by an Early Postdoc Mobility grant from the Swiss National Science Foundation (Grant no.165285). We are grateful of the support granted by the National Institute of Biomedical Imaging and Bioengineering (EB-002804 and EB-002026).

References

(1) Abragam, A.; Goldman, M. Principles of dynamic nuclear polarisation. *Reports on Progress in Physics* **1978,** *41* (3), 395.
(2) Carver, T. R.; Slichter, C. P. Polarization of Nuclear Spins in Metals. *Physical Review* **1953,** *92* (1), 212.
(3) Berman, H. M.; Westbrook, J.; Feng, Z.; Gilliland, G.; Bhat, T. N.; Weissig, H.; Shindyalov, I. N.; Bourne, P. E. The protein data bank. *Nucleic acids research* **2000,** *28* (1), 235.
(4) Rosay, M.; Stowe Winter School on Biomolecular SSNMR, 2018.
(5) Becerra, L. R. R.; Gerfen, G. J. J.; Bellew, B. F. F.; Bryant, J. A. A.; Hall, D. A. A.; Inati, S. J. J.; Weber, R. T. T.; Un, S.; Prisner, T. F. F.; McDermott, A. E. E.et al. A Spectrometer for Dynamic Nuclear Polarization and Electron Paramagnetic Resonance at High Frequencies. *Journal of Magnetic Resonance, Series A* **1995,** *117* (1), 28.
(6) Abragam, A.; Proctor, W. G. *Une Nouvelle Methode De Polarisation Dynamique Des Noyaux Atomiques Dans Les Solides*, 1958.

(7) Overhauser, A. W. Polarization of nuclei in metals. *Physical Review* **1953,** *92* (2), 411.
(8) Hwang, C. F.; Hill, D. A. New effect in dynamic polarization. *Physical Review Letters* **1967,** *18* (4), 110.
(9) Borghini, M. Spin-temperature model of nuclear dynamic polarization using free radicals. *Physical Review Letters* **1968,** *20* (9), 419.
(10) Jeffries, C. D. Polarization of Nuclei by Resonance Saturation in Paramagnetic Crystals. *Physical Review* **1957,** *106* (1), 164.
(11) Hovav, Y.; Feintuch, A.; Vega, S. Theoretical aspects of dynamic nuclear polarization in the solid state - The solid effect. *Journal of Magnetic Resonance* **2010,** *207* (2), 176.
(12) Hu, K.-N.; Debelouchina, G. T.; Smith, A. A.; Griffin, R. G. Quantum mechanical theory of dynamic nuclear polarization in solid dielectrics. *The Journal of chemical physics* **2011,** *134* (12), 125105.
(13) Wenckebach, W. T. The Solid Effect. *Applied Magnetic Resonance* **2008,** *34* (3-4), 227.
(14) Thurber, K. R.; Tycko, R. Theory for cross effect dynamic nuclear polarization under magic-angle spinning in solid state nuclear magnetic resonance: The importance of level crossings. *Journal of Chemical Physics* **2012,** *137* (8), 0.
(15) Corzilius, B.; Smith, A. A.; Griffin, R. G. Solid effect in magic angle spinning dynamic nuclear polarization. *The Journal of chemical physics* **2012,** *137* (5), 054201.
(16) Haeberlen, U.; Waugh, J. Coherent Averaging Effects in Magnetic Resonance. *Physical Review* **1968,** *175* (2), 453.
(17) de Boer, W. Dynamic orientation of nuclei at low temperatures. *Journal of Low Temperature Physics* **1976,** *22* (1-2), 185.
(18) Smith, A. A.; Corzilius, B.; Haze, O.; Swager, T. M.; Griffin, R. G. Observation of strongly forbidden solid effect dynamic nuclear polarization transitions via electron-electron double resonance detected NMR. *Journal of Chemical Physics* **2013,** *139* (21), 1.
(19) Kaushik, M.; Bahrenberg, T.; Can, T. V.; Caporini, M. A.; Silvers, R.; Heiliger, J.; Smith, A. A.; Schwalbe, H.; Griffin, R. G.; Corzilius, B. Gd(III) and Mn(II) complexes for dynamic nuclear polarization: small molecular chelate polarizing agents and applications with site-directed spin labeling of proteins. *Phys. Chem. Chem. Phys.* **2016,** *18* (39), 27205.
(20) Hwang, C. F.; Hill, D. A. Phenomenological Model for the New Effect in Dynamic Polarization. *Physical Review Letters* **1967,** *19* (18), 1011.
(21) Hu, K.-N. N.; Bajaj, V. S.; Rosay, M.; Griffin, R. G. High-frequency dynamic nuclear polarization using mixtures of TEMPO and trityl radicals. *Journal of Chemical Physics* **2007,** *126* (4), 044512.
(22) Song, C.; Hu, K.-n. N.; Joo, C.-g. G.; Swager, T. M.; Griffin, R. G. TOTAPOL: a biradical polarizing agent for dynamic nuclear polarization experiments in aqueous media. *Journal of the American Chemical Society* **2006,** *128* (35), 11385.
(23) Hu, K.-N.; Yu, H.-h.; Swager, T. M.; Griffin, R. G. Dynamic Nuclear Polarization with Biradicals. *Journal of the American Chemical Society* **2004,** *126* (35), 10844.
(24) Nagaraj, M.; Franks, T. W.; Saeidpour, S.; Schubeis, T.; Oschkinat, H.; Ritter, C.; van Rossum, B. J. Surface Binding of TOTAPOL Assists Structural Investigations of Amyloid Fibrils by Dynamic Nuclear Polarization NMR Spectroscopy. *ChemBioChem* **2016**, 1308.
(25) Hovav, Y.; Feintuch, A.; Vega, S. Theoretical aspects of dynamic nuclear polarization in the solid state - The cross effect. *Journal of Magnetic Resonance* **2012,** *214* (2), 29.
(26) Mentink-Vigier, F.; Akbey, Ü.; Oschkinat, H.; Vega, S.; Feintuch, A. Theoretical aspects of Magic Angle Spinning - Dynamic Nuclear Polarization. *Journal of Magnetic Resonance* **2015,** *258*, 102.
(27) Jeschke, G. A new mechanism for chemically induced dynamic nuclear polarization in the solid state. *Journal of the American Chemical Society* **1998,** *120* (18), 4425.
(28) Ravera, E.; Shimon, D.; Feintuch, A.; Goldfarb, D.; Vega, S.; Flori, A.; Luchinat, C.; Menichetti, L.; Parigi, G. The effect of Gd on trityl-based dynamic nuclear polarisation in solids. *Physical Chemistry Chemical Physics* **2015,** *17* (40), 26969.
(29) Mentink-Vigier, F.; Paul, S.; Lee, D.; Feintuch, A.; Hediger, S.; Vega, S.; De Paëpe, G. Nuclear depolarization and absolute sensitivity in magic-angle spinning cross effect dynamic nuclear polarization. *Physical Chemistry Chemical Physics* **2015,** *17* (34), 21824.
(30) Thurber, K. R.; Tycko, R. Perturbation of nuclear spin polarizations in solid state NMR of nitroxide-doped samples by magic-angle spinning without microwaves. *The Journal of chemical physics* **2014,** *140* (18), 184201.
(31) Verel, R.; Baldus, M.; Nijman, M.; van Os, J. W. M.; Meier, B. H. Adiabatic homonuclear polarization transfer in magic-angle- spinning solid-state NMR. *Chemical Physics Letters* **1997,** *280* (1-2), 31.
(32) Raleigh, D. P. P.; Levitt, M. H. H.; Griffin, R. G. G.; Bitter, F.; Magnet, N. Rotational resonance in solid state NMR. *Chemical Physics Letters* **1988,** *146* (1-2), 71.
(33) Solomon, I. Relaxation processes in a system of two spins. *Physical Review* **1955,** *99* (2), 559.
(34) Griesinger, C.; Bennati, M.; Vieth, H. M.; Luchinat, C.; Parigi, G.; Höfer, P.; Engelke, F.; Glaser, S. J.; Denysenkov, V.; Prisner, T. F. Dynamic nuclear polarization at high magnetic fields in liquids. *Progress in nuclear magnetic resonance spectroscopy* **2012,** *64*, 4.
(35) Lingwood, M. D.; Han, S. In *Annual Reports on NMR Spectroscopy*; Webb, G. A., Ed.; Academic Press, 2011; Vol. 73.
(36) Gunther, U. L. Dynamic nuclear hyperpolarization in liquids. *Top Curr Chem* **2013,** *335*, 23.
(37) Slichter, C. P. The discovery and renaissance of dynamic nuclear polarization. *Reports on Progress in Physics* **2014,** *77* (7).

(38) Can, T. V.; Caporini, M. A.; Mentink-Vigier, F.; Corzilius, B.; Walish, J. J.; Rosay, M.; Maas, W. E.; Baldus, M.; Vega, S.; Swager, T. M.et al. Overhauser effects in insulating solids. *The Journal of Chemical Physics* **2014,** *141* (6), 064202.
(39) Pylaeva, S.; Ivanov, K. L.; Baldus, M.; Sebastiani, D.; Elgabarty, H. Molecular Mechanism of Overhauser Dynamic Nuclear Polarization in Insulating Solids. *Journal of Physical Chemistry Letters* **2017,** *8* (10), 2137.
(40) Ji, X.; Can, T. V.; Mentink-Vigier, F.; Bornet, A.; Milani, J.; Vuichoud, B.; Caporini, M. A.; Griffin, R. G.; Jannin, S.; Goldman, M.et al. Overhauser effects in non-conducting solids at 1.2 K. *Journal of Magnetic Resonance* **2018,** *286*, 138.
(41) Chaudhari, S. R.; Wisser, D.; Pinon, A. C.; Berruyer, P.; Gajan, D.; Tordo, P.; Ouari, O.; Reiter, C.; Engelke, F.; Copéret, C.et al. Dynamic Nuclear Polarization Efficiency Increased by Very Fast Magic Angle Spinning. *Journal of the American Chemical Society* **2017**, jacs.7b05194.
(42) Lelli, M.; Chaudhari, S. R.; Gajan, D.; Casano, G.; Rossini, A. J.; Ouari, O.; Tordo, P.; Lesage, A.; Emsley, L. Solid-State Dynamic Nuclear Polarization at 9.4 and 18.8 T from 100 K to Room Temperature. *Journal of the American Chemical Society* **2015,** *137* (46), 14558.
(43) Chaudhari, S. R.; Wisser, D.; Pinon, A. C.; Berruyer, P.; Gajan, D.; Tordo, P.; Ouari, O.; Reiter, C.; Engelke, F.; Copéret, C.et al. Dynamic Nuclear Polarization Efficiency Increased by Very Fast Magic Angle Spinning. *Journal of the American Chemical Society* **2017,** *139* (31), 10609.
(44) van Bentum, P. J. M.; Sharma, M.; van Meerten, S. G. J.; Kentgens, A. P. M. Solid Effect DNP in a Rapid-melt setup. *Journal of Magnetic Resonance* **2016,** *263*, 126.
(45) Ardenkjaer-Larsen, J. H.; Fridlund, B.; Gram, A.; Hansson, G.; Hansson, L.; Lerche, M. H.; Servin, R.; Thaning, M.; Golman, K. Increase in signal-to-noise ratio of > 10,000 times in liquid-state NMR. *Proceedings of the National Academy of Sciences of the United States of America* **2003,** *100* (18), 10158.
(46) Hovav, Y.; Feintuch, A.; Vega, S. Theoretical aspects of dynamic nuclear polarization in the solid state – spin temperature and thermal mixing. *Phys. Chem. Chem. Phys.* **2013,** *15* (1), 188.
(47) Provotorov, B. N. Magnetic resonance saturation in crystals. *Journal of Experimental and Theoretical Physics* **1962,** *14* (5), 1126.
(48) Wenckebach, W. T. Dynamic nuclear polarization via thermal mixing: Beyond the high temperature approximation. *Journal of Magnetic Resonance* **2017,** *277*, 68.
(49) Karabanov, A.; Kwiatkowski, G.; Perotto, C. U.; Wiśniewski, D.; McMaster, J.; Lesanovsky, I.; Köckenberger, W. Dynamic nuclear polarisation by thermal mixing: quantum theory and macroscopic simulations. *Phys. Chem. Chem. Phys.* **2016,** *18* (43), 30093.
(50) Henstra, A.; Lin, T. S.; Schmidt, J.; Wenckebach, W. T. High dynamic nuclear polarization at room temperature. *Chemical Physics Letters* **1990,** *165* (1), 6.
(51) Tateishi, K.; Negoro, M.; Nishida, S.; Kagawa, A.; Morita, Y.; Kitagawa, M. Room temperature hyperpolarization of nuclear spins in bulk. *Proceedings of the National Academy of Sciences of the United States of America* **2014,** *111* (21), 7527.
(52) Can, T. V.; Walish, J. J.; Swager, T. M.; Griffin, R. G. Time domain DNP with the NOVEL sequence. *The Journal of chemical physics* **2015,** *143* (5), 054201.
(53) Bloembergen, N.; Sorokin, P. P. Nuclear Magnetic Resonance in the Cesium Halides. *Physical Review* **1958,** *110* (4), 865.
(54) Wind, R. A.; Li, L.; Lock, H.; Maciel, G. E. Dynamic nuclear polarization in the nuclear rotating frame. *Journal of Magnetic Resonance (1969)* **1988,** *79* (3), 577.
(55) Farrar, C. T.; Hall, D. A.; Gerfen, G. J.; Rosay, M.; Ardenkjær-Larsen, J. H.; Griffin, R. G. High-Frequency Dynamic Nuclear Polarization in the Nuclear Rotating Frame. *Journal of Magnetic Resonance* **2000,** *144* (1), 134.
(56) Weis, V.; Bennati, M.; Rosay, M.; Griffin, R. G. Solid effect in the electron spin dressed state: a new approach for dynamic nuclear polarization. *Journal of Chemical Physics* **2000,** *113* (16), 6795.
(57) Saliba, E. P.; Sesti, E. L.; Scott, F. J.; Albert, B. J.; Choi, E. J.; Alaniva, N.; Gao, C.; Barnes, A. B. Electron Decoupling with Dynamic Nuclear Polarization in Rotating Solids. *Journal of the American Chemical Society* **2017,** *139* (18), 6310.
(58) Can, T. V.; Ni, Q. Z.; Griffin, R. G. Mechanisms of dynamic nuclear polarization in insulating solids. *Journal of Magnetic Resonance* **2015,** *253*, 23.
(59) Henstra, A.; Dirksen, P.; Schmidt, J.; Wenckebach, W. T. Nuclear spin orientation via electron spin locking (NOVEL). *Journal of Magnetic Resonance (1969)* **1988,** *77* (2), 389.
(60) Henstra, A.; Wenckebach, W. T. The theory of nuclear orientation via electron spin locking (NOVEL). *Molecular Physics* **2008,** *106* (7), 859.
(61) Hartmann, S. R.; Hahn, E. L. Nuclear Double Resonance in the Rotating Frame. *Physical Review* **1962,** *128* (5), 2042.
(62) Mathies, G.; Jain, S.; Reese, M.; Griffin, R. G. Pulsed Dynamic Nuclear Polarization with Trityl Radicals. *The journal of physical chemistry letters* **2016,** *7* (1), 111.
(63) Can, T. V.; Weber, R. T.; Walish, J. J.; Swager, T. M.; Griffin, R. G. Ramped-amplitude NOVEL. *The Journal of Chemical Physics* **2017,** *146* (15), 154204.
(64) Jain, S. K.; Mathies, G.; Griffin, R. G. Off-resonance NOVEL. *The Journal of Chemical Physics* **2017,** *147* (16), 164201.

(65) Baldus, M.; Petkova, A. T.; Herzfeld, J.; Griffin, R. G. Cross polarization in the tilted frame: assignment and spectral simplification in heteronuclear spin systems. *Molecular Physics* **1998,** *95* (6), 1197.
(66) Henstra, A.; Dirksen, P.; Wenckebach, W. T. Enhanced dynamic nuclear polarization by the integrated solid effect. *Physics Letters A* **1988,** *134* (2), 134.
(67) Henstra, a.; Wenckebach, W. T. Dynamic nuclear polarisation via the integrated solid effect I: theory. *Molecular Physics* **2013,** *112* (May 2014), 1.
(68) Eichhorn, T. R.; Brandt, B. v. d.; Hautle, P.; Henstra, A.; Wenckebach, W. T. Dynamic nuclear polarisation via the integrated solid effect II: experiments on naphthalene- h8doped with pentacene- d14. *Molecular Physics* **2013,** *112* (13), 1773.
(69) Bornet, A.; Milani, J.; Vuichoud, B.; Perez Linde, A. J.; Bodenhausen, G.; Jannin, S. Microwave frequency modulation to enhance Dissolution Dynamic Nuclear Polarization. *Chemical Physics Letters* **2014,** *602*, 63.
(70) Hovav, Y.; Feintuch, A.; Vega, S.; Goldfarb, D. Dynamic nuclear polarization using frequency modulation at 3.34 T. *Journal of Magnetic Resonance* **2014,** *238*, 94.
(71) Can, T. V.; Weber, R. T.; Walish, J. J.; Swager, T. M.; Griffin, R. G. Frequency-Swept Integrated Solid Effect. *Angewandte Chemie International Edition* **2017,** *56* (24), 6744.
(72) Andrew, E. R.; Bradbury, A.; Eades, R. G. Nuclear Magnetic Resonance Spectra from a Crystal rotated at High Speed. *Nature* **1958,** *182* (4650), 1659.
(73) Bennett, A. E.; Griffin, R. G.; Ok, J. H.; Vega, S. Chemical shift correlation spectroscopy in rotating solids: Radio frequency-driven dipolar recoupling and longitudinal exchange. *The Journal of Chemical Physics* **1992,** *96* (11), 8624.
(74) Scholz, I.; van Beek, J. D.; Ernst, M. Operator-based Floquet theory in solid-state NMR. *Solid state nuclear magnetic resonance* **2010,** *37* (3-4), 39.
(75) Leskes, M.; Madhu, P. K.; Vega, S. Floquet theory in solid-state nuclear magnetic resonance. *Progress in nuclear magnetic resonance spectroscopy* **2010,** *57* (4), 345.
(76) Tan, K. O.; Rajeswari, M.; Madhu, P. K.; Ernst, M. Asynchronous symmetry-based sequences for homonuclear dipolar recoupling in solid-state nuclear magnetic resonance. *The Journal of Chemical Physics* **2015,** *142* (6), 065101.
(77) Tan, K. O.; Agarwal, V.; Meier, B. H.; Ernst, M. A generalized theoretical framework for the description of spin decoupling in solid-state MAS NMR: Offset effect on decoupling performance. *The Journal of Chemical Physics* **2016,** *145* (9), 094201.
(78) Rosay, M., MIT, 2001.
(79) Pinon, A.; Rossini, A. J.; Widdifield, C. M.; Gajan, D.; Emsley, L. Polymorphs of Theophylline Characterized by DNP Enhanced Solid-State NMR. *Mol Pharm* **2015,** *12* (11), 4146.
(80) Sauvée, C.; Rosay, M.; Casano, G.; Aussenac, F.; Weber, R. T.; Ouari, O.; Tordo, P. Highly efficient, water-soluble polarizing agents for dynamic nuclear polarization at high frequency. *Angewandte Chemie - International Edition* **2013,** *52* (41), 10858.
(81) Mathies, G.; Caporini, M. A.; Michaelis, V. K.; Liu, Y.; Hu, K. N.; Mance, D.; Zweier, J. L.; Rosay, M.; Baldus, M.; Griffin, R. G. Efficient Dynamic Nuclear Polarization at 800 MHz/527 GHz with Trityl-Nitroxide Biradicals. *Angewandte Chemie - International Edition* **2015,** *54* (40), 11770.
(82) Gast, P.; Mance, D.; Zurlo, E.; Ivanov, K. L.; Baldus, M.; Huber, M. A tailored multi-frequency EPR approach to accurately determine the magnetic resonance parameters of dynamic nuclear polarization agents: application to AMUPol. *Physical Chemistry Chemical Physics* **2017,** *19* (5), 3777.
(83) Hu, K. N.; Song, C.; Yu, H. H.; Swager, T. M.; Griffin, R. G. High-frequency dynamic nuclear polarization using biradicals: A multifrequency EPR lineshape analysis. *Journal of Chemical Physics* **2008,** *128* (5).
(84) Kubicki, D. J.; Casano, G.; Schwarzwälder, M.; Abel, S.; Sauvée, C.; Ganesan, K.; Yulikov, M.; Rossini, A. J.; Jeschke, G.; Copéret, C.et al. Rational design of dinitroxide biradicals for efficient cross-effect dynamic nuclear polarization. *Chemical Science* **2016,** *7* (1), 550.
(85) Yau, W.-M.; Thurber, K. R.; Tycko, R. Synthesis and evaluation of nitroxide-based oligoradicals for low-temperature dynamic nuclear polarization in solid state NMR. *Journal of Magnetic Resonance* **2014,** *244*, 98.
(86) Matsuki, Y.; Maly, T.; Ouari, O.; Karoui, H.; Le Moigne, F.; Rizzato, E.; Lyubenova, S.; Herzfeld, J.; Prisner, T.; Tordo, P.et al. Dynamic nuclear polarization with a rigid biradical. *Angew Chem Int Ed Engl* **2009,** *48* (27), 4996.
(87) Zagdoun, A.; Casano, G.; Ouari, O.; Lapadula, G.; Rossini, A. J.; Lelli, M.; Baffert, M.; Gajan, D.; Veyre, L.; Maas, W. E.et al. A slowly relaxing rigid biradical for efficient dynamic nuclear polarization surface-enhanced NMR spectroscopy: expeditious characterization of functional group manipulation in hybrid materials. *Journal of the American Chemical Society* **2012,** *134* (4), 2284.
(88) Zagdoun, A.; Casano, G.; Ouari, O.; Schwarzwalder, M.; Rossini, A. J.; Aussenac, F.; Yulikov, M.; Jeschke, G.; Coperet, C.; Lesage, A.et al. Large molecular weight nitroxide biradicals providing efficient dynamic nuclear polarization at temperatures up to 200 K. *J Am Chem Soc* **2013,** *135* (34), 12790.
(89) Corzilius, B.; Smith, A. A.; Barnes, A. B.; Luchinat, C.; Bertini, I.; Griffin, R. G. High-field dynamic nuclear polarization with high-spin transition metal ions. *Journal of the American Chemical Society* **2011,** *133* (15), 5648.
(90) Maly, T.; Debelouchina, G. T.; Bajaj, V. S.; Hu, K.-N.; Joo, C.-G.; Mak-Jurkauskas, M. L.; Sirigiri, J. R.; van der Wel, P. C. A.; Herzfeld, J.; Temkin, R. J.et al. Dynamic nuclear polarization at high magnetic fields. *The Journal of chemical physics* **2008,** *128* (5), 052211.

(91) Smith, A. N.; Caporini, M. A.; Fanucci , G. E.; Long, J. R. A Method for Dynamic Nuclear Polarization Enhancement of Membrane Proteins. *Angewandte Chemie International Edition* **2014,** *54* (5), 1542.

(92) Takahashi, H.; Lee, D.; Dubois, L.; Bardet, M.; Hediger, S.; De Paëpe, G. Rapid Natural ‐ Abundance 2D 13C ‐ 13C Correlation Spectroscopy Using Dynamic Nuclear Polarization Enhanced Solid ‐ State NMR and Matrix ‐ Free Sample Preparation. *Angewandte Chemie International Edition* **2012,** *51* (47), 11766.

(93) Takahashi, H.; Hediger, S.; Paëpe, G. D. Matrix-free dynamic nuclear polarization enables solid-state NMR 13 C– 13 C correlation spectroscopy of proteins at natural isotopic abundance. *Chemical Communications* **2013,** *49* (82), 9479.

(94) Fernández-de-Alba, C.; Takahashi, H.; Richard, A.; Chenavier, Y.; Dubois, L.; Maurel, V.; Lee, D.; Hediger, S.; De Paëpe, G. Matrix-Free DNP-Enhanced NMR Spectroscopy of Liposomes Using a Lipid-Anchored Biradical. *Chemistry - A European Journal* **2015,** *21* (12), 4512.

(95) W., v. d. C. E. A.; J., K. E.; Claire, S.; E., H. R.; Markus, W.; Olivier, O.; Eduardo, P.; Paul, T.; Marc, B. Biomolecular DNP-Supported NMR Spectroscopy using Site-Directed Spin Labeling. *Chemistry – A European Journal* **2015,** *21* (37), 12971.

(96) Albert, B. J.; Gao, C.; Sesti, E. L.; Saliba, E. P.; Alaniva, N.; Scott, F. J.; Sigurdsson, S. T.; Barnes, A. B. Dynamic Nuclear Polarization Nuclear Magnetic Resonance in Human Cells Using Fluorescent Polarizing Agents. *Biochemistry* **2018**.

(97) Mar, G. N. L.; Horrocks, W. D.; Holm, R. H. *NMR of Paramagnetic Molecules: Principles and Applications*; Academic Press Inc, 1974.

(98) Corzilius, B.; Andreas, L. B.; Smith, A. A.; Ni, Q. Z.; Griffin, R. G. Paramagnet induced signal quenching in MAS-DNP experiments in frozen homogeneous solutions. *Journal of magnetic resonance (San Diego, Calif. : 1997)* **2014,** *240*, 113.

(99) Perez Linde, A. J.; Chinthalapalli, S.; Carnevale, D.; Bodenhausen, G. Rotation-induced recovery and bleaching in magnetic resonance. *Phys. Chem. Chem. Phys.* **2015,** *17* (9), 6415.

(100) Mentink-Vigier, F.; Mathies, G.; Liu, Y.; Barra, A.-L.; Caporini, M. A.; Lee, D.; Hediger, S.; Griffin, R. G.; De Paëpe, G. Efficient cross-effect dynamic nuclear polarization without depolarization in high-resolution MAS NMR. *Chemical Science* **2017,** *8* (12), 8150.

(101) Bouleau, E.; Saint-Bonnet, P.; Mentink-Vigier, F.; Takahashi, H.; Jacquot, J. F.; Bardet, M.; Aussenac, F.; Purea, A.; Engelke, F.; Hediger, S.et al. Pushing NMR sensitivity limits using dynamic nuclear polarization with closed-loop cryogenic helium sample spinning. *Chemical Science* **2015,** *6* (12), 6806.

(102) Leavesley, A.; Wilson, C. B.; Sherwin, M.; Han, S. Effect of water/glycerol polymorphism on dynamic nuclear polarization. *Physical Chemistry Chemical Physics* **2018,** *20* (15), 9897.

(103) Smith, A. A.; Corzilius, B.; Barnes, A. B.; Maly, T.; Griffin, R. G. Solid effect dynamic nuclear polarization and polarization pathways. *The Journal of Chemical Physics* **2012,** *136* (1), 015101.

(104) Stoll, S.; Schweiger, A. EasySpin, a comprehensive software package for spectral simulation and analysis in EPR. *Journal of Magnetic Resonance* **2006,** *178* (1), 42.

(105) Hogben, H. J.; Krzystyniak, M.; Charnock, G. T. P.; Hore, P. J.; Kuprov, I. Spinach - A software library for simulation of spin dynamics in large spin systems. *Journal of Magnetic Resonance* **2011,** *208* (2), 179.

(106) Veshtort, M.; Griffin, R. G. SPINEVOLUTION: A powerful tool for the simulation of solid and liquid state NMR experiments. *Journal of Magnetic Resonance* **2006,** *178* (2), 248.

(107) Vold, R. L.; Vold, R. R. Nuclear magnetic relaxation in coupled spin systems. *Progress in Nuclear Magnetic Resonance Spectroscopy* **1978,** *12* (2), 79.

(108) Karabanov, A.; Kwiatkowski, G.; Köckenberger, W. Spin dynamic simulations of solid effect DNP: The role of the relaxation superoperator. *Molecular Physics* **2014,** *112* (14), 1838.

(109) Havel, T. F. Metric matrix embedding in protein structure calculations, NMR spectra analysis, and relaxation theory. *Magnetic Resonance in Chemistry* **2003,** *41* (S1), S37.

(110) Karabanov, A.; Kwiatkowski, G.; Köckenberger, W. Quantum Mechanical Simulation of Cross Effect DNP Using Krylov–Bogolyubov Averaging. *Applied Magnetic Resonance* **2012,** *43* (1-2), 43.

(111) Levante, T. O.; Ernst, R. R. Homogeneous versus inhomogeneous quantum-mechancial master equations. *Chem. Phys. Lett.* **1995,** *241* (July), 73.

(112) Levitt, M. H.; Di Bari, L. Steady state in magnetic resonance pulse experiments. *Physical Review Letters* **1992,** *69* (21), 3124.

(113) Can, T. V.; McKay, J. E.; Weber, R. T.; Yang, C.; Dubroca, T.; van Tol, J.; Hill, S.; Griffin, R. G. Frequency-Swept Integrated and Stretched Solid Effect Dynamic Nuclear Polarization. *The Journal of Physical Chemistry Letters* **2018**, 3187.

(114) Bloembergen, N. On the interaction of nuclear spins in a crystalline lattice. *Physica* **1949,** *15* (3-4), 386.

(115) Bloembergen, N.; Shapiro, S.; Pershan, P. S.; Artman, J. O. Cross-Relaxation in Spin Systems. *Physical Review* **1959,** *114* (2), 445.

(116) Wolfe, J. P. Direct observation of a nuclear spin diffusion barrier. *Physical Review Letters* **1973,** *31* (15), 907.

(117) Wolfe, J. P.; Markiewicz, R. S. Near-Nuclei Magnetic Resonance of CaF2:Yb3+. *Physical Review Letters* **1973,** *30* (22), 1105.

(118) Hansen, A. D. A.; Wolfe, J. P. Measurement of the nuclear spin diffusion barrier around Eu2+ ions in CaF2. *Physics Letters A* **1978,** *66* (4), 320.

(119) Karabanov, A.; Kuprov, I.; Charnock, G. T. P.; van der Drift, A.; Edwards, L. J.; Köckenberger, W. On the accuracy of the state space restriction approximation for spin dynamics simulations. *The Journal of Chemical Physics* **2011,** *135* (8), 084106.
(120) Karabanov, A.; van der Drift, A.; Edwards, L. J.; Kuprov, I.; Köckenberger, W. Quantum mechanical simulation of solid effect dynamic nuclear polarisation using Krylov–Bogolyubov time averaging and a restricted state-space. *Physical Chemistry Chemical Physics* **2012,** *14* (8), 2658.
(121) Karabanov, A.; Wiśniewski, D.; Lesanovsky, I.; Köckenberger, W. Dynamic Nuclear Polarization as Kinetically Constrained Diffusion. *Physical Review Letters* **2015,** *115* (2), 020404.
(122) Mentink-Vigier, F.; Vega, S.; De Paëpe, G. Fast and accurate MAS-DNP simulations of large spin ensembles. *Phys. Chem. Chem. Phys.* **2017,** *19* (5), 3506.
(123) Un, S.; Prisner, T.; Weber, R. T.; Seaman, M. J.; Fishbein, K. W.; McDermott, A. E.; Singel, D. J.; Griffin, R. G. Pulsed dynamic nuclear polarization at 5 T. *Chemical Physics Letters* **1992,** *189* (1), 54.
(124) Becerra, L. R.; Gerfen, G. J.; Temkin, R. J.; Singel, D. J.; Griffin, R. G. Dynamic Nuclear Polarization with a Cyclotron Resonance Maser at 5 T. *Physical Review Letters* **1993,** *71* (21), 3561.
(125) Granatstein, V. L.; Parker, R. K.; Armstrong, C. M. Vacuum electronics at the dawn of the twenty-first century. *Proceedings of the IEEE* **1999,** *87* (5), 702.
(126) Booske, J. H.; Dobbs, R. J.; Joye, C. D.; Kory, C. L.; Neil, G. R.; Park, G. S.; Park, J.; Temkin, R. J. Vacuum Electronic High Power Terahertz Sources. *IEEE Transactions on Terahertz Science and Technology* **2011,** *1* (1), 54.
(127) Tucek, J.; Basten, M.; Gallagher, D.; Kreischer, K. 2016 IEEE International Vacuum Electronics Conference (IVEC), 2016; p 1.
(128) Hesler, J. L.; Crowe, T. In *SPIE Newsroom*, 2015.
(129) Komiak, J. J. GaN HEMT: Dominant Force in High-Frequency Solid-State Power Amplifiers. *IEEE Microwave Magazine* **2015,** *16* (3), 97.
(130) Crowe, T. W.; Hesler, J. L.; Retzloff, S. A.; Kurtz, D. S. International Conference on Infrared, Millimeter, and Terahertz Waves, Cancun, 2017; p 1.
(131) Siles, J. V.; Lee, C.; Lin, R.; Mehdi, I. International Conference on Infrared, Millimeter, and Terahertz Waves, Cancun, 2017; p 1.
(132) Weis, V.; Bennati, M.; Rosay, M.; Bryant, J. A.; Griffin, R. G. High-Field DNP and ENDOR with a Novel Multiple-Frequency Resonance Structure. *Journal of Magnetic Resonance* **1999,** *140* (1), 293.
(133) Thurber, K. R.; Yau, W.-M.; Tycko, R. Low-temperature dynamic nuclear polarization at 9.4T with a 30mW microwave source. *Journal of Magnetic Resonance* **2010,** *204* (2), 303.
(134) Siaw, T. A.; Leavesley, A.; Lund, A.; Kaminker, I.; Han, S. A versatile and modular quasi optics-based 200 GHz dual dynamic nuclear polarization and electron paramagnetic resonance instrument. *Journal of Magnetic Resonance* **2016,** *264*, 131.
(135) Leavesley, A.; Shimon, D.; Siaw, T. A.; Feintuch, A.; Goldfarb, D.; Vega, S.; Kaminker, I.; Han, S. Effect of electron spectral diffusion on static dynamic nuclear polarization at 7 Tesla. *Phys. Chem. Chem. Phys.* **2017,** *19* (5), 3596.
(136) Carter, R. G. *Microwave and RF Vacuum Electronic Power Sources*; Cambridge University Press, 2018.
(137) Tsimring, S. E. *Electron beams and microwave vacuum electronics*; John Wiley & Sons, 2006.
(138) Basu, B. *Electromagnetic theory and applications in beam-wave electronics*; World scientific, 1996.
(139) Parker, R. K.; Abrams, R. H.; Danly, B. G.; Levush, B. Vacuum electronics. *IEEE Transactions on Microwave Theory and Techniques* **2002,** *50* (3), 835.
(140) Wind, R. A.; Anthonio, F. E.; Duijvestijn, M. J.; Smidt, J.; Trommel, J.; de Vette, G. M. C. Experimental setup for enhanced 13C NMR spectroscopy in solids using dynamic nuclear polarization. *Journal of Magnetic Resonance (1969)* **1983,** *52* (3), 424.
(141) Afeworki, M.; Vega, S.; Schaefer, J. Direct Electron-to-Carbon Polarization Transfer in Homogeneously Doped Polycarbonates. *Macromolecules* **1992,** *25* (16), 4100.
(142) Kemp, T. F.; Dannatt, H. R. W.; Barrow, N. S.; Watts, A.; Brown, S. P.; Newton, M. E.; Dupree, R. Dynamic Nuclear Polarization enhanced NMR at 187 GHz/284 MHz using an Extended Interaction Klystron amplifier. *Journal of Magnetic Resonance* **2016,** *265*, 77.
(143) Potapov, A.; Yau, W.-M.; Ghirlando, R.; Thurber, K. R.; Tycko, R. Successive Stages of Amyloid-β Self-Assembly Characterized by Solid-State Nuclear Magnetic Resonance with Dynamic Nuclear Polarization. *Journal of the American Chemical Society* **2015,** *137* (25), 8294.
(144) Communications and Power Industries.
(145) Berry, D.; Deng, H.; Dobbs, R.; Horoyski, P.; Hyttinen, M.; Kingsmill, A.; MacHattie, R.; Roitman, A.; Sokol, E.; Steer, B. Practical Aspects of EIK Technology. *IEEE Transactions on Electron Devices* **2014,** *61* (6), 1830.
(146) Kowalski, E. J.; Shapiro, M. A.; Temkin, R. J. An Overmoded W-Band Coupled-Cavity TWT. *IEEE Transactions on Electron Devices* **2015,** *62* (5), 1609.
(147) Stephens, J. C.; Tucek, J. C.; Basten, M. A.; Kresicher, K. E.; Shapiro, M. A.; Temkin, R. J. International Vacuum Electronics Conference, 2018.
(148) Barker, R. J.; Booske, J. H.; Neville C. Luhmann, Jr.; Nusinovich, G. S. *Modern Microwave and Millimeter-Wave Power Electronics*; Wiley-IEEE Press, 2005.

(149) Rosay, M.; Tometich, L.; Pawsey, S.; Bader, R.; Schauwecker, R.; Blank, M.; Borchard, P.; Cauffman, S.; Felch, K.; Weber, R.et al. Solid-state dynamic nuclear polarization at 263 GHz: spectrometer design and experimental results. *Physical Chemistry Chemical Physics* **2010,** *12* (22), 5850.
(150) Nusinovich, G. S. *Introduction to the Physics of Gyrotrons (Johns Hopkins Studies in Applied Physics)*; Johns Hopkins University Press, 2004.
(151) Benford, J.; Swegle, J. A.; Schamiloglu, E. *High Power Microwaves, Third Edition (Series in Plasma Physics)*; CRC Press, 2015.
(152) Flyagin, V. A.; Gaponov, A. V.; Petelin, I.; Yulpatov, V. K. The Gyrotron. *IEEE Transactions on Microwave Theory and Techniques* **1977,** *25* (6), 514.
(153) Felch, K. L.; Danly, B. G.; Jory, H. R.; Kreischer, K. E.; Lawson, W.; Levush, B.; Temkin, R. J. Characteristics and applications of fast-wave gyrodevices. *Proceedings of the IEEE* **1999,** *87* (5), 752.
(154) Vlasov, S. N.; Orlova, I. M. Quasioptical transformer which transforms the waves in a waveguide having a circular cross section into a highly directional wave beam. *Radiophysics and Quantum Electronics* **1974,** *17* (1), 115.
(155) Choi, E. M.; Shapiro, M. A.; Sirigiri, J. R.; Temkin, R. J. Calculation of Radiation from a Helically Cut Waveguide for a Gyrotron Mode Converter in the Quasi-Optical Approximation. *Journal of Infrared, Millimeter, and Terahertz Waves* **2009,** *30* (1), 8.
(156) Jawla, S. K.; Guss, W. C.; Shapiro, M. A.; R.J., T. 2014 39th International Conference on Infrared, Millimeter, and Terahertz waves (IRMMW-THz), 2014; p 1.
(157) Blank, M.; Borchard, P.; Cauffman, S.; Felch, K.; Rosay, M.; Tometich, L. High-frequency gyrotrons for DNP-enhanced NMR applications. *IEEE International Vacuum Electronics Conference* **2014**.
(158) Joye, C. D.; Griffin, R. G.; Hornstein, M. K.; Hu, K.-N.; Kreischer, K. E.; Rosay, M.; Shapiro, M. A.; Sirigiri, J. R.; Temkin, R. J.; Woskov, P. P. Operational characteristics of a 14-W 140-GHz gyrotron for dynamic nuclear polarization. *IEEE Transactions on Plasma Science* **2006,** *34* (3), 518.
(159) Barnes, A. B.; Nanni, E. A.; Herzfeld, J.; Griffin, R. G.; Temkin, R. J. A 250GHz Gyrotron with a 3GHz Tuning Bandwidth for Dynamic Nuclear Polarization. *Journal of Magnetic Resonance* **2012,** *221*, 147.
(160) Jawla, S.; Ni, Q. Z.; Barnes, A.; Guss, W.; Daviso, E.; Herzfeld, J.; Griffin, R.; Temkin, R. Continuously Tunable 250 GHz Gyrotron with a Double Disk Window for DNP-NMR Spectroscopy. *Journal of Infrared, Millimeter, and Terahertz Waves* **2012,** *34* (1), 42.
(161) Torrezan, A. C.; Shapiro, M. A.; Sirigiri, J. R.; Temkin, R. J.; Griffin, R. G. Operation of a Continuously Frequency-Tunable Second-Harmonic CW 330-GHz Gyrotron for Dynamic Nuclear Polarization. *IEEE Transactions on Electron Devices* **2011,** *58* (8), 2777.
(162) Torrezan, A. C.; Seong-Tae, H.; Mastovsky, I.; Shapiro, M. A.; Sirigiri, J. R.; Temkin, R. J.; Barnes, A. B.; Griffin, R. G. Continuous-Wave Operation of a Frequency-Tunable 460-GHz Second-Harmonic Gyrotron for Enhanced Nuclear Magnetic Resonance. *IEEE Transactions on Plasma Science* **2010,** *38* (6), 1150.
(163) Jawla, S.; Reese, M.; George, C.; Chen, Y.; Shapiro, M.; Griffin, R.; Temkin, R., 2016; p 1.
(164) Barnes, A. B.; Markhasin, E.; Daviso, E.; Michaelis, V. K.; Nanni, E. A.; Jawla, S. K.; Mena, E. L.; DeRocher, R.; Thakkar, A.; Woskov, P. P.et al. Dynamic Nuclear Polarization at 700MHz/460GHz. *Journal of Magnetic Resonance* **2012,** *224*, 1.
(165) Ikeda, R.; Yamaguchi, Y.; Tatematsu, Y.; Idehara, T.; Ogawa, I.; Saito, T.; Matsuki, Y.; Fujiwara, T. Broadband Continuously Frequency Tunable Gyrotron for 600 MHz DNP-NMR Spectroscopy. *Plasma and Fusion Research* **2014,** *9* (0), 1206058.
(166) Manuilov, V. N.; Glyavin, M. Y.; Sedov, A. S.; Zaslavsky, V. Y.; Idehara, T. Design of a Second Harmonic Double-Beam Continuous Wave Gyrotron with Operating Frequency of 0.79 THz. *Journal of Infrared, Millimeter, and Terahertz Waves* **2015,** *36* (12), 1164.
(167) Idehara, T.; Glyavin, M.; Kuleshov, A.; Sabchevski, S.; Manuilov, V.; Zaslavsky, V.; Zotova, I.; Sedov, A. Experimental study of a THz band double-beam gyrotron. *2017 42nd International Conference on Infrared, Millimeter, and Terahertz Waves (IRMMW-THz)* **2017**.
(168) Dumbrajs, O.; Idehara, T. Theoretical Study on the 1.185-THz Third Harmonic Gyrotron. *Journal of Infrared, Millimeter, and Terahertz Waves* **2017**.
(169) Idehara, T.; Ogawa, I.; Mori, H.; Kobayashi, S.-i.; Mitsudo, S.; Saito, T. 2008 33rd International Conference on Infrared, Millimeter and Terahertz Waves, 2008; p 1.
(170) Idehara, T.; Kosuga, K.; Agusu, L.; Ikeda, R.; Ogawa, I.; Saito, T.; Matsuki, Y.; Ueda, K.; Fujiwara, T. Continuously Frequency Tunable High Power Sub-THz Radiation Source-Gyrotron FU CW VI for 600 MHz DNP-NMR Spectroscopy. *Journal of Infrared, Millimeter, and Terahertz Waves* **2010,** *31* (7), 775.
(171) Idehara, T.; Tatematsu, Y.; Yamaguchi, Y.; Khutoryan, E. M.; Kuleshov, A. N.; Ueda, K.; Matsuki, Y.; Fujiwara, T. The Development of 460 GHz gyrotrons for 700 MHz DNP-NMR spectroscopy. *Journal of Infrared, Millimeter, and Terahertz Waves* **2015,** *36* (7), 613.
(172) Idehara, T.; Khutoryan, E. M.; Tatematsu, Y.; Yamaguchi, Y.; Kuleshov, A. N.; Dumbrajs, O.; Matsuki, Y.; Fujiwara, T. High-Speed Frequency Modulation of a 460-GHz Gyrotron for Enhancement of 700-MHz DNP-NMR Spectroscopy. *Journal of Infrared, Millimeter, and Terahertz Waves* **2015,** *36* (9), 819.
(173) Hogge, J. P.; Braunmueller, F.; Alberti, S.; Genoud, J.; Tran, T. M.; Vuillemin, Q.; Tran, M. Q.; Ansermet, J. P.; Cuanillon, P.; Macor, A.et al., 2013; p 1.

(174) Bogdashov, A. A.; Belousov, V. I.; Chirkov, A. V.; Denisov, G. G.; Korchagin, V. V.; Kornishin, S. Y.; Tai, E. M. Transmission Line for 258 GHz Gyrotron DNP Spectrometry. *Journal of Infrared, Millimeter, and Terahertz Waves* **2011,** *32* (6), 823.
(175) Denysenkov, V.; Prandolini, M. J.; Gafurov, M.; Sezer, D.; Endeward, B.; Prisner, T. F. Liquid State DNP Using a 260 GHz High Power Gyrotron. *Physical Chemistry Chemical Physics* **2010,** *12* (22), 5786.
(176) Li, Z.-D.; Du, C.-H.; Qi, X.-B.; Luo, L.; Liu, P.-K. A 0.33-THz second-harmonic frequency-tunable gyrotron. *Chinese Physics B* **2016,** *25* (2), 029401.
(177) Soane, A. V.; Shapiro, M. A.; Jawla, S.; Temkin, R. J. Operation of a 140-GHz Gyro-Amplifier Using a Dielectric-Loaded, Severless Confocal Waveguide. *IEEE Transactions on Plasma Science* **2017,** *45* (10), 2835.
(178) Nanni, E. A.; Lewis, S. M.; Shapiro, M. A.; Griffin, R. G.; Temkin, R. J. Photonic-Band-Gap Traveling-Wave Gyrotron Amplifier. *Physical Review Letters* **2013,** *111* (23), 235101.
(179) Nanni, E. A.; Jawla, S.; Lewis, S. M.; Shapiro, M. A.; Temkin, R. J. Photonic-band-gap gyrotron amplifier with picosecond pulses. *Applied Physics Letters* **2017,** *111* (23), 233504.
(180) Bhartia, P.; Bahl, I. J. *Millimeter wave engineering and applications*; Wiley: New York, 1984.
(181) Thumm, M. K.; Kasparek, W. Passive high-power microwave components. *IEEE Transactions on Plasma Science* **2002,** *30* (3), 755.
(182) Dragone, C. Attenuation and Radiation Characteristics of the HE11-Mode. *IEEE Transactions on Microwave Theory and Techniques* **1980,** *28* (7), 704.
(183) Doane, J. L. In *Infrared and millimeter waves*; Academic Press: Orlando, 1985; Vol. 13.
(184) Clarricoats, P. J. B.; Olver, A. D. *Corrugated horns for microwave antennas*; P. Peregrinus on behalf of the Institution of Electrical Engineers: London, UK, 1984.
(185) Clarricoats, P. J. B.; Olver, A. D.; Chong, S. L. Attenuation in corrugated circular waveguides. Part 1: Theory. *Proceedings of the Institution of Electrical Engineers* **1975,** *122* (11), 1173.
(186) Callis, R. W.; Cary, W. P.; Ellis, R.; Gorelov, Y. A.; Grunloh, H. J.; Lohr, J.; Peavy, J. J.; Pinsker, R. I.; Ponce, D.; Prater, R., 2002; p 294.
(187) Leuterer, F.; Beckmann, M.; Brinkschulte, H.; Monaco, F.; Münich, M.; Ryter, F.; Schütz, H.; Empacher, L.; Gantenbein, G.; Förster, W.et al. Experience with the ECRH system of ASDEX-Upgrade. *Fusion Engineering and Design* **2001,** *53* (1-4), 485.
(188) Kowalski, E. J.; Tax, D. S.; Shapiro, M. A.; Sirigiri, J. R.; Temkin, R. J.; Bigelow, T. S.; Rasmussen, D. A. Linearly Polarized Modes of a Corrugated Metallic Waveguide. *IEEE Transactions on Microwave Theory and Techniques* **2010,** *58* (11), 2772.
(189) Nanni, E. A.; Barnes, A. B.; Griffin, R. G.; Temkin, R. J. THz Dynamic Nuclear Polarization NMR. *IEEE Transactions on Terahertz Science and Technology* **2011,** *1* (1), 145.
(190) Woskov, P. P.; Nanni, E. A.; Shapiro, M. A.; Jawla, S. K.; Hummelt, J. S.; Temkin, R. J.; Barnes, A. B. 330 GHz helically corrugated waveguide. *2011 International Conference on Infrared, Millimeter, and Terahertz Waves* **2011**.
(191) Nanni, E. A.; Jawla, S. K.; Shapiro, M. A.; Woskov, P. P.; Temkin, R. J. Low-loss Transmission Lines for High-power Terahertz Radiation. *Journal of Infrared, Millimeter, and Terahertz Waves* **2012,** *33* (7), 695.
(192) Pike, K. J.; Kemp, T. F.; Takahashi, H.; Day, R.; Howes, A. P.; Kryukov, E. V.; MacDonald, J. F.; Collis, A. E. C.; Bolton, D. R.; Wylde, R. J.et al. A spectrometer designed for 6.7 and 14.1T DNP-enhanced solid-state MAS NMR using quasi-optical microwave transmission. *Journal of Magnetic Resonance* **2012,** *215*, 1.
(193) Armstrong, B. D.; Edwards, D. T.; Wylde, R. J.; Walker, S. A.; Han, S. A 200 GHz dynamic nuclear polarization spectrometer. *Physical Chemistry Chemical Physics* **2010,** *12* (22), 5920.
(194) Dubroca, T.; Smith, A. N.; Pike, K. J.; Froud, S.; Wylde, R.; Trociewitz, B.; McKay, J.; Mentink-Vigier, F.; van Tol, J.; Wi, S.et al. A quasi-optical and corrugated waveguide microwave transmission system for simultaneous dynamic nuclear polarization NMR on two separate 14.1 T spectrometers. *Journal of Magnetic Resonance* **2018,** *289*, 35.
(195) Wang, W.; Chasteen, D. N. Construction and Performance of Ribbon-Wound TE011Cylindrical EPR/ENDOR Cavities. *Journal of Magnetic Resonance, Series A* **1995,** *116* (2), 237.
(196) Smith, A. A.; Corzilius, B.; Bryant, J. A.; DeRocher, R.; Woskov, P. P.; Temkin, R. J.; Griffin, R. G. A 140GHz Pulsed EPR/212MHz NMR Spectrometer for DNP Studies. *Journal of Magnetic Resonance* **2012,** *223*, 170.
(197) Paulson, E. K.; Martin, R. W.; Zilm, K. W. Cross polarization, radio frequency field homogeneity, and circuit balancing in high field solid state NMR probes. *Journal of Magnetic Resonance* **2004,** *171* (2), 314.
(198) Prisner, T.; Denysenkov, V.; Sezer, D. Liquid state DNP at high magnetic fields: Instrumentation, experimental results and atomistic modelling by molecular dynamics simulations. *Journal of Magnetic Resonance* **2016,** *264*, 68.
(199) Thurber, K. R.; Tycko, R. Biomolecular solid state NMR with magic-angle spinning at 25K. *Journal of Magnetic Resonance* **2008,** *195* (2), 179.
(200) Becerra, L. R.; Gerfen, G. J.; Bellew, B. F.; Bryant, J. A.; Hall, D. A.; Inati, S. J.; Weber, R. T.; Un, S.; Prisner, T. F.; McDermott, A. E.et al. A Spectrometer for Dynamic Nuclear Polarization and Electron Paramagnetic Resonance at High Frequencies. *Journal of Magnetic Resonance, Series A* **1995,** *117* (1), 28.
(201) Barnes, A. B.; Mak-Jurkauskas, M. L.; Matsuki, Y.; Bajaj, V. S.; van der Wel, P. C. A.; DeRocher, R.; Bryant, J.; Sirigiri, J. R.; Temkin, R. J.; Lugtenburg, J.et al. Cryogenic sample exchange NMR probe for magic angle spinning dynamic nuclear polarization. *Journal of Magnetic Resonance* **2009,** *198* (2), 261.

(202) Nanni, E. A.; Barnes, A. B.; Matsuki, Y.; Woskov, P. P.; Corzilius, B.; Griffin, R. G.; Temkin, R. J. Microwave Field Distribution in a Magic Angle Spinning Dynamic Nuclear Polarization NMR Probe. *Journal of Magnetic Resonance* **2011,** *210* (1), 16.
(203) Rosay, M.; Blank, M.; Engelke, F. Instrumentation for solid-state dynamic nuclear polarization with magic angle spinning NMR. *Journal of Magnetic Resonance* **2016,** *264*, 88.
(204) Macor, A.; de Rijk, E.; Annino, G.; Alberti, S.; Ansermet, J. P. THz-Waves Channeling in a Monolithic Saddle-Coil for Dynamic Nuclear Polarization Enhanced NMR. *Journal of Magnetic Resonance* **2011,** *212* (2), 440.
(205) Kubicki, D. J.; Rossini, A. J.; Purea, A.; Zagdoun, A.; Ouari, O.; Tordo, P.; Engelke, F.; Lesage, A.; Emsley, L. Amplifying Dynamic Nuclear Polarization of Frozen Solutions by Incorporating Dielectric Particles. *Journal of the American Chemical Society* **2014,** *136* (44), 15711.
(206) Matsuki, Y.; Takahashi, H.; Ueda, K.; Idehara, T.; Ogawa, I.; Toda, M.; Akutsu, H.; Fujiwara, T. Dynamic nuclear polarization experiments at 14.1 T for solid-state NMR. *Physical Chemistry Chemical Physics* **2010,** *12* (22), 5799.
(207) Albert, B. J.; Pahng, S. H.; Alaniva, N.; Sesti, E. L.; Rand, P. W.; Saliba, E. P.; Scott, F. J.; Choi, E. J.; Barnes, A. B. Instrumentation for cryogenic magic angle spinning dynamic nuclear polarization using 90L of liquid nitrogen per day. *Journal of Magnetic Resonance* **2017,** *283* (Supplement C), 71.
(208) Thurber, K. R.; Potapov, A.; Yau, W.-M.; Tycko, R. Solid State Nuclear Magnetic Resonance with Magic-Angle Spinning and Dynamic Nuclear Polarization below 25K. *Journal of Magnetic Resonance* **2013,** *226*, 100.
(209) Thurber, K.; Tycko, R. Low-temperature dynamic nuclear polarization with helium-cooled samples and nitrogen-driven magic-angle spinning. *Journal of Magnetic Resonance* **2016,** *264*, 99.
(210) Lee, D.; Bouleau, E.; Saint-Bonnet, P.; Hediger, S.; De Paëpe, G. Ultra-low temperature MAS-DNP. *Journal of Magnetic Resonance* **2016,** *264*, 116.
(211) Matsuki, Y.; Nakamura, S.; Fukui, S.; Suematsu, H.; Fujiwara, T. Closed-cycle cold helium magic-angle spinning for sensitivity-enhanced multi-dimensional solid-state NMR. *Journal of Magnetic Resonance* **2015,** *259*, 76.
(212) Matsuki, Y.; Idehara, T.; Fukazawa, J.; Fujiwara, T. Advanced instrumentation for DNP-enhanced MAS NMR for higher magnetic fields and lower temperatures. *Journal of Magnetic Resonance* **2016,** *264*, 107.
(213) Chaudhari, S. R.; Berruyer, P.; Gajan, D.; Reiter, C.; Engelke, F.; Silverio, D. L.; Coperet, C.; Lelli, M.; Lesage, A.; Emsley, L. Dynamic nuclear polarization at 40 kHz magic angle spinning. *Physical Chemistry Chemical Physics* **2016,** *18* (15), 10616.
(214) Sergeyev, I. V.; Itin, B.; Rogawski, R.; Day, L. A.; McDermott, A. E. Efficient assignment and NMR analysis of an intact virus using sequential side-chain correlations and DNP sensitization. *Proceedings of the National Academy of Sciences* **2017**.
(215) Zilm, K. W.; Alderman, D. W.; Grant, D. M. A high-speed magic angle spinner. *Journal of Magnetic Resonance (1969)* **1978,** *30* (3), 563.
(216) Osen, D.; Knott, B.; Bruker BioSpin GmbH, 2017.
(217) Thumm, M.; Heidinger, R.; Arnold, A.; Blumhofer, M.; Illy, S.; Meier, A.; Piosczyk, B.; Rohde, M.; Schneider, R.; Severloh, P. "ITER ECRF window development - CVD-diamond window. Final report," Association Euratom-Forschungszentrum Karlsruhe GmbH Technik und Umwelt (Germany), 2002.
(218) INSACO.
(219) Wind, R. A.; Duijvestijn, M. J.; van der Lugt, C.; Manenschijn, A.; Vriend, J. Applications of dynamic nuclear polarization in 13C NMR in solids. *Progress in Nuclear Magnetic Resonance Spectroscopy* **1985,** *17*, 33.
(220) Wind, R. A.; Duijvestijn, M. J.; van der Lugt, C.; Smidt, J.; Vriend, H. An investigation of coal by means of e.s.r., 1H n.m.r., 13C n.m.r. and dynamic nuclear polarization. *Fuel* **1987,** *66* (7), 876.
(221) Lock, H.; Wind, R. A.; Maciel, G. E.; Johnson, C. E. A study of 13C ‐ enriched chemical vapor deposited diamond film by means of 13C nuclear magnetic resonance, electron paramagnetic resonance, and dynamic nuclear polarization. *The Journal of Chemical Physics* **1993,** *99* (5), 3363.
(222) Afeworki, M.; McKay, R. A.; Schaefer, J. Selective observation of the interface of heterogeneous polycarbonate/polystyrene blends by dynamic nuclear polarization carbon-13 NMR spectroscopy. *Macromolecules* **1992,** *25* (16), 4084.
(223) Afeworki, M.; Schaefer, J. Molecular dynamics of polycarbonate chains at the interface of polycarbonate/polystyrene heterogeneous blends. *Macromolecules* **1992,** *25* (16), 4097.
(224) Afeworki, M.; McKay, R. A.; Schaefer, J. Dynamic Nuclear Polarization Enhanced Nuclear Magnetic Resonance of Polymer-Blend Interfaces. *Materials Science and Engineering: A* **1993,** *162* (1-2), 221.
(225) Gerfen, G. J.; Becerra, L. R.; Hall, D. A.; Griffin, R. G.; Temkin, R. J.; Singel, D. J. High Frequency (140 GHz) Dynamic Nuclear Polarization: Polarization Transfer to a Solute in Frozen Aqueous Solution. *The Journal of Chemical Physics* **1995,** *102* (24), 9494.
(226) Hall, D. A.; Maus, D. C.; Gerfen, G. J.; Inati, S. J.; Becerra, L. R.; Dahlquist, F. W.; Griffin, R. G. Polarization-Enhanced NMR Spectroscopy of Biomolecules in Frozen Solution. *Science* **1997,** *276* (5314), 930.
(227) Piveteau, L.; Ong, T.-C.; Walder, B. J.; Dirin, D. N.; Moscheni, D.; Schneider, B.; Bär, J.; Protesescu, L.; Masciocchi, N.; Guagliardi, A.et al. Resolving the Core and the Surface of CdSe Quantum Dots and Nanoplatelets Using Dynamic Nuclear Polarization Enhanced PASS–PIETA NMR Spectroscopy. **2018**.
(228) Leskes, M.; Kim, G.; Liu, T.; Michan, A. L.; Aussenac, F.; Dorffer, P.; Paul, S.; Grey, C. P. Surface-Sensitive NMR Detection of the Solid Electrolyte Interphase Layer on Reduced Graphene Oxide. **2017**.

(229) Lopez del Amo, J.-M.; Schneider, D.; Loquet, A.; Lange, A.; Reif, B. Cryogenic solid state NMR studies of fibrils of the Alzheimer's disease amyloid-β peptide: perspectives for DNP. *Journal of Biomolecular NMR* **2013,** *56* (4), 359.

(230) Mak-Jurkauskas, M. L.; Bajaj, V. S.; Hornstein, M. K.; Belenky, M.; Griffin, R. G.; Herzfeld, J. Energy transformations early in the bacteriorhodopsin photocycle revealed by DNP-enhanced solid-state NMR. *Proceedings of the National Academy of Sciences* **2008,** *105* (3), 883.

(231) Bajaj, V. S.; Mak-Jurkauskas, M. L.; Belenky, M.; Herzfeld, J.; Griffin, R. G. Functional and shunt states of bacteriorhodopsin resolved by 250 GHz dynamic nuclear polarization–enhanced solid-state NMR. *Proceedings of the National Academy of Sciences* **2009,** *106* (23), 9244.

(232) Bajaj, V. S.; Mak-Jurkauskas, M. L.; Belenky, M.; Herzfeld, J.; Griffin, R. G. DNP enhanced frequency-selective TEDOR experiments in bacteriorhodopsin. *Journal of Magnetic Resonance* **2010,** *202* (1), 9.

(233) Ni, Q. Z.; Markhasin, E.; Can, T. V.; Corzilius, B.; Tan, K. O.; Barnes, A. B.; Daviso, E.; Su, Y.; Herzfeld, J.; Griffin, R. G. Peptide and Protein Dynamics and Low-Temperature/DNP Magic Angle Spinning NMR. *The Journal of Physical Chemistry B* **2017,** *121* (19), 4997.

(234) Barnes, A. B.; Corzilius, B.; Mak-Jurkauskas, M. L.; Andreas, L. B.; Bajaj, V. S.; Matsuki, Y.; Belenky, M. L.; Lugtenburg, J.; Sirigiri, J. R.; Temkin, R. J.et al. Resolution and polarization distribution in cryogenic DNP/MAS experiments. *Physical Chemistry Chemical Physics* **2010,** *12* (22), 5861.

(235) van der Wel, P. C. A.; Hu, K.-N.; Lewandowski, J.; Griffin, R. G. Dynamic Nuclear Polarization of Amyloidogenic Peptide Nanocrystals: GNNQQNY, a Core Segment of the Yeast Prion Protein Sup35p. *Journal of the American Chemical Society* **2006,** *128* (33), 10840.

(236) Debelouchina, G. T.; Bayro, M. J.; van der Wel, P. C. A.; Caporini, M. A.; Barnes, A. B.; Rosay, M.; Maas, W. E.; Griffin, R. G. Dynamic nuclear polarization-enhanced solid-state NMR spectroscopy of GNNQQNY nanocrystals and amyloid fibrils. *Physical Chemistry Chemical Physics* **2010,** *12* (22), 5911.

(237) Bayro, M. J.; Debelouchina, G. T.; Eddy, M. T.; Birkett, N. R.; MacPhee, C. E.; Rosay, M.; Maas, W. E.; Dobson, C. M.; Griffin, R. G. Intermolecular Structure Determination of Amyloid Fibrils with Magic-Angle Spinning and Dynamic Nuclear Polarization NMR. *Journal of the American Chemical Society* **2011,** *133* (35), 13967.

(238) Debelouchina, G. T.; Bayro, M. J.; Fitzpatrick, A. W.; Ladizhansky, V.; Colvin, M. T.; Caporini, M. A.; Jaroniec, C. P.; Bajaj, V. S.; Rosay, M.; MacPhee, C. E.et al. Higher Order Amyloid Fibril Structure by MAS NMR and DNP Spectroscopy. *Journal of the American Chemical Society* **2013,** *135* (51), 19237.

(239) Ni, Q. Z.; Can, T. V.; Daviso, E.; Belenky, M.; Griffin, R. G.; Herzfeld, J. Primary Transfer Step in the Light-Driven Ion Pump Bacteriorhodopsin: An Irreversible U-Turn Revealed by Dynamic Nuclear Polarization-Enhanced Magic Angle Spinning NMR. *Journal of the American Chemical Society* **2018**.

(240) Becker-Baldus, J.; Bamann, C.; Saxena, K.; Gustmann, H.; Brown, L. J.; Brown, R. C. D.; Reiter, C.; Bamberg, E.; Wachtveitl, J.; Schwalbe, H.et al. Enlightening the photoactive site of channelrhodopsin-2 by DNP-enhanced solid-state NMR spectroscopy. *Proceedings of the National Academy of Sciences* **2015,** *112* (32), 9896.

(241) Maciejko, J.; Mehler, M.; Kaur, J.; Lieblein, T.; Morgner, N.; Ouari, O.; Tordo, P.; Becker-Baldus, J.; Glaubitz, C. Visualizing Specific Cross-Protomer Interactions in the Homo-Oligomeric Membrane Protein Proteorhodopsin by Dynamic-Nuclear-Polarization-Enhanced Solid-State NMR. *Journal of the American Chemical Society* **2015,** *137* (28), 9032.

(242) Andreas, L. B.; Barnes, A. B.; Corzilius, B.; Chou, J. J.; Miller, E. A.; Caporini, M.; Rosay, M.; Griffin, R. G. Dynamic Nuclear Polarization Study of Inhibitor Binding to the M218–60 Proton Transporter from Influenza A. *Biochemistry* **2013,** *52* (16), 2774.

(243) Ong, Y. S.; Lakatos, A.; Becker-Baldus, J.; Pos, K. M.; Glaubitz, C. Detecting Substrates Bound to the Secondary Multidrug Efflux Pump EmrE by DNP-Enhanced Solid-State NMR. *Journal of the American Chemical Society* **2013,** *135* (42), 15754.

(244) Lehnert, E.; Mao, J.; Mehdipour, A. R.; Hummer, G.; Abele, R.; Glaubitz, C.; Tampé, R. Antigenic Peptide Recognition on the Human ABC Transporter TAP Resolved by DNP-Enhanced Solid-State NMR Spectroscopy. *Journal of the American Chemical Society* **2016,** *138* (42), 13967.

(245) Spadaccini, R.; Kaur, H.; Becker-Baldus, J.; Glaubitz, C. The effect of drug binding on specific sites in transmembrane helices 4 and 6 of the ABC exporter MsbA studied by DNP-enhanced solid-state NMR. *Biochimica et Biophysica Acta (BBA) - Biomembranes* **2018,** *1860* (4), 833.

(246) Linden, A. H.; Lange, S.; Franks, W. T.; Akbey, Ü.; Specker, E.; van Rossum, B.-J.; Oschkinat, H. Neurotoxin II Bound to Acetylcholine Receptors in Native Membranes Studied by Dynamic Nuclear Polarization NMR. *Journal of the American Chemical Society* **2011,** *133* (48), 19266.

(247) Jacso, T.; Franks, W. T.; Rose, H.; Fink, U.; Broecker, J.; Keller, S.; Oschkinat, H.; Reif, B. Characterization of Membrane Proteins in Isolated Native Cellular Membranes by Dynamic Nuclear Polarization Solid‐State NMR Spectroscopy without Purification and Reconstitution. *Angewandte Chemie* **2012,** *124* (2), 447.

(248) Gelis, I.; Vitzthum, V.; Dhimole, N.; Caporini, M. A.; Schedlbauer, A.; Carnevale, D.; Connell, S. R.; Fucini, P.; Bodenhausen, G. Solid-state NMR enhanced by dynamic nuclear polarization as a novel tool for ribosome structural biology. *Journal of Biomolecular NMR* **2013,** *56* (2), 85.

(249) Sergeyev, I. V.; Day, L. A.; Goldbourt, A.; McDermott, A. E. Chemical Shifts for the Unusual DNA Structure in Pf1 Bacteriophage from Dynamic-Nuclear-Polarization-Enhanced Solid-State NMR Spectroscopy. *Journal of the American Chemical Society* **2011,** *133* (50), 20208.

(250) Wenk, P.; Kaushik, M.; Richter, D.; Vogel, M.; Suess, B.; Corzilius, B. Dynamic nuclear polarization of nucleic acid with endogenously bound manganese. *Journal of Biomolecular NMR* **2015,** *63* (1), 97.
(251) Koers, E. J.; Cruijsen, E. A. W. v. d.; Rosay, M.; Weingarth, M.; Prokofyev, A.; Sauvée, C.; Ouari, O.; Zwan, J. v. d.; Pongs, O.; Tordo, P.et al. NMR-based structural biology enhanced by dynamic nuclear polarization at high magnetic field. *Journal of Biomolecular NMR* **2014,** *60* (2-3), 157.
(252) Wang, T.; Park, Y. B.; Caporini, M. A.; Rosay, M.; Zhong, L.; Cosgrove, D. J.; Hong, M. Sensitivity-enhanced solid-state NMR detection of expansin's target in plant cell walls. *Proceedings of the National Academy of Sciences* **2013,** *110* (41), 16444.
(253) Stöppler, D.; Song, C.; van Rossum, B. J.; Geiger, M. A.; Lang, C.; Mroginski, M. A.; Jagtap Anil, P.; Sigurdsson Snorri, T.; Matysik, J.; Hughes, J.et al. Dynamic Nuclear Polarization Provides New Insights into Chromophore Structure in Phytochrome Photoreceptors. *Angewandte Chemie International Edition* **2016,** *55* (52), 16017.
(254) Frederick, Kendra K.; Michaelis, Vladimir K.; Corzilius, B.; Ong, T.-C.; Jacavone, Angela C.; Griffin, Robert G.; Lindquist, S. Sensitivity-Enhanced NMR Reveals Alterations in Protein Structure by Cellular Milieus. *Cell* **2015,** *163* (3), 620.
(255) Fricke, P.; Demers, J.-P.; Becker, S.; Lange, A. Studies on the MxiH Protein in T3SS Needles Using DNP-Enhanced ssNMR Spectroscopy. *ChemPhysChem* **2013,** *15* (1), 57.
(256) Fricke, P.; Mance, D.; Chevelkov, V.; Giller, K.; Becker, S.; Baldus, M.; Lange, A. High resolution observed in 800 MHz DNP spectra of extremely rigid type III secretion needles. *Journal of Biomolecular NMR* **2016,** *65* (3-4), 121.
(257) Akbey, Ü.; Linden, A. H.; Oschkinat, H. High-Temperature Dynamic Nuclear Polarization Enhanced Magic-Angle-Spinning NMR. *Applied Magnetic Resonance* **2012,** *43* (1), 81.
(258) Bayro, M. J.; Debelouchina, G. T.; Eddy, M. T.; Birkett, N. R.; MacPhee, C. E.; Rosay, M.; Maas, W. E.; Dobson, C. M.; Griffin, R. G. Intermolecular structure determination of amyloid fibrils with magic-angle spinning and dynamic nuclear polarization NMR. *Journal of the American Chemical Society* **2011,** *133* (35), 13967.
(259) Bondar, A.-N.; Elstner, M.; Suhai, S.; Smith, J. C.; Fischer, S. Mechanism of Primary Proton Transfer in Bacteriorhodopsin. *Structure* **2004,** *12* (7), 1281.
(260) Andreas, L. B.; Barnes, A. B.; Corzilius, B.; Chou, J. J.; Miller, E. A.; Caporini, M.; Rosay, M.; Griffin, R. G. Dynamic nuclear polarization study of inhibitor binding to the M2(18-60) proton transporter from influenza A. *Biochemistry* **2013,** *52* (16), 2774.
(261) Wright, P. E.; Dyson, H. J. Intrinsically disordered proteins in cellular signalling and regulation. *Nature Reviews Molecular Cell Biology* **2014,** *16*, 18.
(262) Jaudzems, K.; Bertarello, A.; Chaudhari, S. R.; Pica, A.; Cala-DePaepe, D.; Barbet-Massin, E.; Pell, A. J.; Akopjana, I.; Kotelovica, S.; Gajan, D.et al. Dynamic Nuclear Polarization-Enhanced Biomolecular NMR Spectroscopy at High Magnetic Field with Fast Magic-Angle Spinning. *Angewandte Chemie - International Edition* **2018**, 7458.
(263) Lesage, A.; Lelli, M.; Gajan, D.; Caporini, M. A.; Vitzthum, V.; Miéville, P.; Alauzun, J.; Roussey, A.; Thieuleux, C.; Mehdi, A.et al. Surface enhanced NMR spectroscopy by dynamic nuclear polarization. *Journal of the American Chemical Society* **2010,** *132* (44), 15459.
(264) Kobayashi, T.; DiVerdi, J. A.; Maciel, G. E. Silica gel surface: Molecular dynamics of surface silanols. *Journal of Physical Chemistry C* **2008,** *112* (11), 4315.
(265) Lafon, O.; Rosay, M.; Aussenac, F.; Lu, X.; Trebosc, J.; Cristini, O.; Kinowski, C.; Touati, N.; Vezin, H.; Amoureux, J.-P. Beyond the Silica Surface by Direct Silicon-29 Dynamic Nuclear Polarization. *Angewandte Chemie-International Edition* **2011,** *50* (36), 8367.
(266) Lelli, M.; Gajan, D.; Lesage, A.; Caporini, M. A.; Vitzthum, V.; Miéville, P.; Héroguel, F.; Rascón, F.; Roussey, A.; Thieuleux, C.et al. Fast characterization of functionalized silica materials by silicon-29 surface-enhanced NMR spectroscopy using dynamic nuclear polarization. *Journal of the American Chemical Society* **2011,** *133* (7), 2104.
(267) Lee, D.; Monin, G.; Duong, N. T.; Lopez, I. Z.; Bardet, M.; Mareau, V.; Gonon, L.; De Paëpe, G. Untangling the condensation network of organosiloxanes on nanoparticles using 2D29Si-29Si solid-state NMR enhanced by dynamic nuclear polarization. *Journal of the American Chemical Society* **2014,** *136* (39), 13781.
(268) Lee, D.; Takahashi, H.; Thankamony, A. S. L.; Dacquin, J.-P.; Bardet, M.; Lafon, O.; Paëpe, G. D. Enhanced Solid-State NMR Correlation Spectroscopy of Quadrupolar Nuclei Using Dynamic Nuclear Polarization. *Journal of the American Chemical Society* **2012,** *134* (45), 18491.
(269) Vitzthum, V.; Miéville, P.; Carnevale, D.; Caporini, M. A.; Gajan, D.; Copéret, C.; Lelli, M.; Zagdoun, A.; Rossini, A. J.; Lesage, A.et al. Dynamic nuclear polarization of quadrupolar nuclei using cross polarization from protons: Surface-enhanced aluminium-27 NMR. *Chemical Communications* **2012,** *48* (14), 1988.
(270) Lee, D.; Duong, N. T.; Lafon, O.; De Paëpe, G. Primostrato solid-state NMR enhanced by dynamic nuclear polarization: Pentacoordinated Al3+ions are only located at the surface of hydrated γ-alumina. *Journal of Physical Chemistry C* **2014,** *118* (43), 25065.
(271) Kobayashi, T.; Gupta, S.; Caporini, M. A.; Pecharsky, V. K.; Pruski, M. Mechanism of Solid-State Thermolysis of Ammonia Borane: A 15N NMR Study Using Fast Magic-Angle Spinning and Dynamic Nuclear Polarization. *The Journal of Physical Chemistry C* **2014,** *118* (34), 19548.
(272) Blanc, F.; Sperrin, L.; Lee, D.; Dervişoğlu, R.; Yamazaki, Y.; Haile, S. M.; De Paëpe, G.; Grey, C. P. Dynamic nuclear polarization NMR of low-γ nuclei: Structural insights into hydrated yttrium-doped BaZrO3. *Journal of Physical Chemistry Letters* **2014,** *5* (14), 2431.

(273) Blanc, F.; Sperrin, L.; Jefferson, D. A.; Pawsey, S.; Rosay, M.; Grey, C. P. Dynamic nuclear polarization enhanced natural abundance 17O spectroscopy. *Journal of the American Chemical Society* **2013,** *135* (8), 2975.

(274) Perras, F. A.; Kobayashi, T.; Pruski, M. Natural Abundance ¹⁷O DNP Two-Dimensional and Surface-Enhanced NMR Spectroscopy. *Journal of the American Chemical Society* **2015,** *137* (26), 8336.

(275) Perras, F. A.; Chaudhary, U.; Slowing, I. I.; Pruski, M. Probing Surface Hydrogen Bonding and Dynamics by Natural Abundance, Multidimensional, ¹⁷ O DNP-NMR Spectroscopy. *The Journal of Physical Chemistry C* **2016,** *120* (21), 11535.

(276) Hope, M. A.; Halat, D. M.; Magusin, P. C. M. M.; Paul, S.; Peng, L.; Grey, C. P. Surface-selective direct 17O DNP NMR of CeO2 nanoparticles. **2017**.

(277) Gunther, W. R.; Michaelis, V. K.; Caporini, M. A.; Griffin, R. G.; Román-Leshkov, Y. Dynamic nuclear polarization NMR enables the analysis of sn-beta zeolite prepared with natural abundance 119Sn precursors. *Journal of the American Chemical Society* **2014,** *136* (17), 6219.

(278) Conley, M. P.; Rossini, A. J.; Comas-Vives, A.; Valla, M.; Casano, G.; Ouari, O.; Tordo, P.; Lesage, A.; Emsley, L.; Copéret, C. Silica-surface reorganization during organotin grafting evidenced by119Sn DNP SENS: A tandem reaction of gem-silanols and strained siloxane bridges. *Physical Chemistry Chemical Physics* **2014,** *16* (33), 17822.

(279) Wolf, P.; Valla, M.; Rossini Aaron, J.; Comas‐Vives, A.; Núñez‐Zarur, F.; Malaman, B.; Lesage, A.; Emsley, L.; Copéret, C.; Hermans, I. NMR Signatures of the Active Sites in Sn‐β Zeolite. *Angewandte Chemie International Edition* **2014,** *53* (38), 10179.

(280) Rossini, A. J.; Zagdoun, A.; Lelli, M.; Lesage, A.; Copéret, C.; Emsley, L. Dynamic nuclear polarization surface enhanced NMR spectroscopy. *Accounts of Chemical Research* **2013,** *46* (9), 1942.

(281) Rossini, A. J.; Zagdoun, A.; Hegner, F.; Schwarzwälder, M.; Gajan, D.; Copéret, C.; Lesage, A.; Emsley, L. Dynamic Nuclear Polarization NMR Spectroscopy of Microcrystalline Solids. *Journal of the American Chemical Society* **2012,** *134* (40), 16899.

(282) Rossini, A. J.; Widdifield, C. M.; Zagdoun, A.; Lelli, M.; Schwarzwälder, M.; Copéret, C.; Lesage, A.; Emsley, L. Dynamic Nuclear Polarization Enhanced NMR Spectroscopy for Pharmaceutical Formulations. *Journal of the American Chemical Society* **2014,** *136* (6), 2324.

(283) Elisei, E.; Filibian, M.; Carretta, P.; Colombo Serra, S.; Tedoldi, F.; Willart, J. F.; Descamps, M.; Cesaro, A. Dynamic nuclear polarization of a glassy matrix prepared by solid state mechanochemical amorphization of crystalline substances. *Chem. Commun.* **2015,** *51* (11), 2080.

(284) Ong, T. C.; Mak-Jurkauskas, M. L.; Walish, J. J.; Michaelis, V. K.; Corzilius, B.; Smith, A. A.; Clausen, A. M.; Cheetham, J. C.; Swager, T. M.; Griffin, R. G. Solvent-Free Dynamic Nuclear Polarization of Amorphous and Crystalline ortho-Terphenyl. *J. Phys. Chem. B* **2013,** *117* (10), 3040.

(285) Ni, Q. Z.; Yang, F.; Can, T. V.; Sergeyev, I. V.; D'Addio, S. M.; Jawla, S. K.; Li, Y.; Lipert, M. P.; Xu, W.; Williamson, R. T.et al. In Situ Characterization of Pharmaceutical Formulations by Dynamic Nuclear Polarization Enhanced MAS NMR. *The Journal of Physical Chemistry B* **2017,** *121* (34), 8132.

(286) Vitzthum, V.; Borcard, F.; Jannin, S.; Morin, M.; Miéville, P.; Caporini, M. A.; Sienkiewicz, A.; Gerber-Lemaire, S.; Bodenhausen , G. Fractional Spin-Labeling of Polymers for Enhancing NMR Sensitivity by Solvent-Free Dynamic Nuclear Polarization. *ChemPhysChem* **2011,** *12* (16), 2929.

(287) Takahashi, H.; Fernández-de-Alba, C.; Lee, D.; Maurel, V.; Gambarelli, S.; Bardet, M.; Hediger, S.; Barra, A.-L.; De Paëpe, G. Optimization of an absolute sensitivity in a glassy matrix during DNP-enhanced multidimensional solid-state NMR experiments. *J. Magn. Reson.* **2014,** *239*, 91.

(288) Gan, Z.; Hung, I.; Wang, X.; Paulino, J.; Wu, G.; Litvak, I. M.; Gor'kov, P. L.; Brey, W. W.; Lendi, P.; Schiano, J. L.et al. NMR spectroscopy up to 35.2T using a series-connected hybrid magnet. *Journal of Magnetic Resonance* **2017,** *284*, 125.

(289) Bauer, T.; Dotta, C.; Balacescu, L.; Gath, J.; Hunkeler, A.; Böckmann, A.; Beat; Meier, H. Line-Broadening in Low-Temperature Solid-State NMR Spectra of Fibrils. *Journal of Biomolecular NMR* **0123,** *0* (1), 51.